PHYSICS-BASED SIMULATION OF TABLET DISINTEGRATION AND DISSOLUTION

by

Yue Li

A Dissertation

Submitted to the Faculty of Purdue University

In Partial Fulfillment of the Requirements for the degree of

Doctor of Philosophy

Department of Industrial and Physical Pharmacy

West Lafayette, Indiana

August 2021

THE PURDUE UNIVERSITY GRADUATE SCHOOL
STATEMENT OF COMMITTEE APPROVAL

Dr. Tonglei Li, Chair

Department of Industrial and Physical Pharmacy

Dr. Kinam Park

Department of Industrial and Physical Pharmacy

Dr. Bumsoo Han

School of Mechanical Engineering

Dr. Qi (Tony) Zhou

Department of Industrial and Physical Pharmacy

Approved by:

Dr. Rodolfo Pinal

For my family.

ACKNOWLEDGMENTS

First and foremost, I would like to thank my Ph.D. advisor, Dr. Tonglei Li, for offering me this opportunity to pursue my doctoral degree at Purdue University. His expertise in pharmaceutical science and computer science is invaluable in formulating this research project. His positive attitude and the pursuit of perfection in research have sharpened my thinking and helped me push the project to a higher level. I would also like to thank members of my advisory committee: Dr. Kinam Park, Dr. Bumsoo Han, and Dr. Qi (Tony) Zhou for providing insightful criticism and excellent scientific advice.

I would also like to thank my lab mates: Dr. Hou Peng for the generous help and the discussions; Dr. Yonghui Qiao for helping me with the experiments and collecting the data; Clairissa Corpstein and Nick Huls for helping me edit my thesis and prune the sentences; and Dr. Xiaoyu Yu and Fudan Zheng for all the help in the lab.

Heartful thanks to my parents and family. Without their support and understating, I could not have completed my studies as a graduate student at Purdue University.

TABLE OF CONTENTS

LIST OF TABLES

LIST OF FIGURES

ABSTRACT

As the most used dosage form in the world, tablets are widely used for the mass production of drugs. The disintegration and dissolution kinetics of tablets play a vital role in the pharmacokinetics and pharmacodynamics of drugs. It is also critical for evaluating the quality of drug formulations. This thesis reports a modeling and simulation approach of tablet disintegration and dissolution processes in a dissolution test device. By coupling the lattice Boltzmann method with the discrete element method, we simulate the hydrodynamics as well as the particle dynamics in the dissolution test device. Our computational methods could model the tablet structure, disintegration of the tablet in the dissolution device, and dissolution of particles under the influence of hydrodynamics. The simulation results show that our computational methods can reproduce experimental results. Our methods pave the path toward an *in-silico* platform for tablet formulation design and verification.

CHAPTER 1. INTRODUCTION

Tablets are the most popular oral dosage form. The disintegration of a given tablet and the subsequent release kinetics of the active pharmaceutical ingredient (API) are facilitated by utilizing swelling polymers as excipients. The disintegration process governs drug release kinetics and plays a crucial role in determining drug absorption and eventual bioavailability. Thus, it is essential to fully understand and predict the disintegration and dissolution process in order to better inform the rational design of tablet formulation.

Several research efforts have been reported in the literature for developing physical models of tablet disintegration and dissolution, such as the finite element method (FEM) [1, 2], the discrete element model (DEM) [3-6], a hybrid of FEM and DEM [7, 8] and the cellular automata method [9]. The DEM approach is promising as it treats particles individually and could easily describe the non-uniform distribution of API and its excipients. However, all of the above methods neglect the fluid dynamics around the tablet. The liquid flow significantly influences the disintegration (and dissolution) of the tablet [10]. The local interactions between liquid and tablet can, therefore, significantly impact the disintegration and dissolution kinetics of the tablet.

Therefore, we aim in this project to develop a physical simulation method for tablet disintegration and dissolution. We will consider and model three basic processes, including particle dissembling, fluid dynamics, and fluid–solid interactions. Unlike what is reported in the literature, our method considers both particle–particle interactions within the tablet and the interaction of liquids flowing onto and around the tablet. For this purpose, the lattice Boltzmann method (LBM) is the general framework used to integrate with the DEM. More specifically, the hydrodynamic condition will be simulated with the LBM, while the structure of the tablet will be represented with DEM particles. The DEM and LBM models will be coupled together to simulate the fluid–solid interaction between liquid and tablet particles.

1.1 Significance of this study

Measurement of the disintegration and dissolution kinetics of tablets has been widely adopted by industry and regulatory agencies for drug development. Several compendial standards, such as USP-NP <701> and <711>, have been established and applied for decades as a way to

measure drug product release [11, 12]. Slight variations in disintegration and/or dissolution kinetics of a limited number of tablets are commonly accepted as the criterion of content uniformity. Granted, these methods play a critical role in ensuring the quality of tablet products, but the test methodology itself offers no direct insight into tablet formulation and formation. This makes it challenging to achieve the Quality by Design (QbD) goal of tablet products. As continuous manufacturing of solid dosage forms is becoming a reality through wide adaptions of process analytical technologies [13, 14], using the disintegration and dissolution test methods in bulk solution as a "black-box" tool presents a hindrance to the effective development and manufacturing of tablet products.

The overarching goal of our research is to mechanistically connect the disintegration and dissolution kinetics of a tablet with its microstructure, including—but not limited to—the composition of the drug (API) and its disintegrants (and other excipients), their distribution in the tablet, particle size, size distribution, inter-particulate bonding, or other interactions. These factors are well known to control or influence the disintegration and dissolution of a tablet. However, few efforts have been made to investigate their influence on kinetic behaviors mechanistically. This proposed project aims to develop physics-based modeling and simulation methods of tablet disintegration and dissolution based on particle properties of the API and the disintegrant, as well as inter-particulate mechanics. Moreover, as hydrodynamic conditions vary significantly in a liquid environment in which a tablet dissolves (e.g., due to mechanical stirring in Apparatus II or peristaltic waves in the GI), we need to fully consider the liquid–particle hydrodynamic forces at the tablet surface and during the dissolution of a drug/excipient particle. It is also critical to consider the physics of water uptake by disintegrant particles and its influence on particle swelling and particle–particle interactions. Fulfilling these requirements, we aim to model the hydrodynamics of a liquid with the LBM, inter-particle kinetics with DEM, and liquid–particle coupling with the immersed moving boundary method (IMBM) [15-17]. All of these methods are rooted in physical descriptions of liquid and particle movements. Thus, the specific aims for this project include:

(1) Integrating the computational methods for simulating tablet disintegration and dissolution. We have implemented most of the computational techniques, including LBM, DEM, and IMBM, and algorithm implementation of particle dissolution and water uptake and swelling of disintegrant particles. We will combine these methods in this project.

(2) Developing an *in silico* model of the tablet micro-structure from physical measurements of particulate properties and mechanical strength, as well as the compression force of tableting. Our overall simulation is at the particulate level, which treats individual particles in a tablet as the fundamental unit for examining disintegration and dissolution kinetics. To simulate a real tablet, we will explore measurement methods of particle properties and particulate organization in a tablet.

(3) Conducting numerical simulations of model tablet products dissolved using the USP apparatus II, and comparing these results with experimental results. We will develop a numerical model for the apparatus (including the stirring bar and vessel) and apply the simulation platform developed in Aim 1 to the *in silico* models of representative tablet products. The simulation results will be compared against experimental data collected using this dissolution method.

Upon completion of the project, our expected outcome is two-fold. First, we expect to establish the connections between particle properties and tablet compression, as well as the kinetics of disintegration and dissolution kinetics. Second, we will gain deeper insight into the concentration distribution in the USP apparatus II and assess possible limitations of the compendial methods in testing various tablet formulations.

1.2 Previous research

In this section, we briefly introduce prior research on the study of tablet disintegration and dissolution in the USP apparatus II. We will primarily focus on the application of computational methods on tablet disintegration and dissolution studies. Finally, we compare our model with previous approaches to show the advantage of our model.

1.2.1 Research on USP apparatus II hydrodynamics

The study of hydrodynamics using dissolution devices like the USP apparatus II is essential for understanding factors impacting the dissolution test. This will help to build standard protocols to reduce the error in dissolution tests and improve the design of the standard dissolution test device.

Traditionally, experiments were performed to image the fluid dynamics with the USP apparatus II. We can observe fluid flow patterns in the device by injecting colored dye from a salicylic acid calibrator tablet [18]. This gives us a general idea of the impact of fluid flow and the concentration distribution during the dissolution test. More quantitative methods, such as laser-

induced fluorescence (LIF), can be used to gain a detailed dissolution profile with the USP apparatus II. The fluorescent dye molecules released by the tablet in the dissolution test will be excited by the laser. By measuring the strengths of fluorescence, we can measure the concentration within the device without sampling from the device [19]. The techniques could help us better understand the concentration distribution of the drug at different dissolution conditions. We know that the velocity of fluids has a significant impact on the dissolution of the tablet. Laser Doppler velocimetry (LDV) could be employed to measure the liquid velocity at a specific location in a dissolution device [20, 21]. Although both LIF and LDV could help us obtain quantitative information about the concentration and velocity distribution within the dissolution device, their measurement of the quantitative information is usually from isolated spots. As experimental methods cannot continuously measure the concentration and velocity fields, it is difficult to gain a complete picture of hydrodynamics and drug concentrations using current methods.

Compared with traditional experimental methods, computational methods have the advantage of flexibility. They can help us gain insight into the dissolution process of the tablet and are free of human errors during the experimental measurements [22-24]. Computational fluid dynamics (CFD) is a widely used method to simulate the fluid dynamics in the USP apparatus II [21, 25-30]. By comparing the simulated results against experimental methods from LDV and particle image velocimetry (PIV), CFD methods have been proven to be accurate and efficient methods for studying the dynamics in the USP apparatus II [19, 25, 31]. Compared to experimental methods, CFD could help us investigate more detailed dynamics in the device. For example, CFD simulations have shown that the velocity and shear rate change dramatically at the bottom of the USP apparatus II, which indicates that the location of the tablet in the dissolution test affects the final result of the compendial method [30] . With the help of CFD simulations, we can also study the impact of paddle agitation speeds on fluid strain rate distribution in the USP apparatus II [32]. While these kinds of studies are usually difficult to perform in an wet lab, they are much easier to perform using CFD simulations.

1.2.2 Tablet disintegration and dissolution

Traditionally, the USP apparatus II has been widely used for the dissolution tests of different drug formulations. However, without understanding the kinetics of tablet disintegration

and dissolution, we are applying trial-and-error methods to examine the effect of different formulations. Scientists used to design multiple new drug formulations based on experience and test them in the USP apparatus II to determine the optimal formulation. Therefore, to facilitate the rational design of the new drug formulation, we must simulate the entire processes of tablet disintegration and dissolution.

As CFD methods focus on liquid dynamics, we must combine CFD with other methods which could simulate the solid tablet in order to study the impact of tablet formulation on the kinetics of disintegration and dissolution. To study hydrodynamics near the tablet in dissolution tests, some simulations placed a geometry of the tablet at the bottom of the USP apparatus II to study the liquid velocity at the surface of the tablet. The mass transfer from tablet to liquid is calculated based on the velocity magnitude [27, 29, 32-34]. This method can only study the impact of liquid dynamics on the whole tablet, and therefore could not examine the effects of different tablet formulations on the dissolution tests. As a result, we need to model the interactions between tablet particles and fluid dynamics.

Tablet dissolution happens alongside disintegration, during which the tablet breaks due to the swelling of the excipient, which changes the dissolution rate of a tablet. Some studies applied numerical methods, such as cellular automata and the FEM, to simulate the swelling of uniform particles [1, 35]. To better model the properties of tablet particles, we use the DEM, in which the particle size densities and solubilities are represented by sphere particles [4]. DEM methods have been widely used in the simulation of the drug manufacturing process. Usually, combined with FEM, DEM could help us to better understand factors affecting the manufacturing of tablets [36]. DEM is also widely used in the study of tablet compression [37, 38].

Much effort has been made to combine CFD with other numerical methods to simulate tablet disintegration and dissolution. For example, by combining CFD with direct numerical simulation (DNS) of particles, the dissolution of particles under different hydrodynamics can be simulated [39, 40]. However, due to the limitations of the coupling method, the velocity field must be extracted from the COMSOL simulation and then imported into an in-house program. Because this means that the coupling is unidirectional, we cannot understand the impact of drug particles on hydrodynamics. Additionally, the simulation could not be performed in real-time, as the software programs are required to use preprocessed velocity data from other programs [40, 41].

In this project, we propose to use a kind of CFD method, namely LBM, coupled with DEM to study tablet disintegration and dissolution rather than solving the Navier-Stoke equation with the FEM or FVM approach. LBM can simulate the fluid dynamics by solving the Boltzmann transport equation [42]. Recently, LBM has gained considerable attention [42-45]. Compared to traditional FEM- and FVM-based methods, LBM has the advantage of being simple to implement. Because all the computation is performed locally, LBM is easily implemented for large-scale parallel computation on CPUs and GPUs [46]. Also, LBM is adept at dealing with complex boundaries and multiphase and multicomponent flows [47, 48].

For what we wanted to simulate in this project, LBM made it easier to implement the coupling between hydrodynamics and particle dynamics. To couple fluids and solids in LBM, two primary methods have between proposed: the momentum exchange method (MEM) [49, 50] and the partially saturated cell method (PSM) [15]. In the MEM, non-slip boundary conditions are used to model the particle surface. In the PSM, the solid particle is model by the ratio of solid part in the lattice node. The solid ratio will determine whether to perform bounce-back boundaries or to treat the node as a fluid. In our simulation, we used PSM, which is also called the immersed moving boundary method (IMBM).

1.2.3 Feasibility of coupling the LBM and DEM from dissolution studies

Compared to previous models for tablet disintegration and dissolution tests, our model has several apparent advantages:

1. The LBM is good at dealing with complex boundaries in simulation. Because we are attempting to simulate the interaction of tablet particles and hydrodynamics, we must deal with the boundary between particles and fluid accurately and efficiently.
2. The LBM could be further developed for large-scale dissolution studies in *in vivo* environments such as the GI tract. Currently, our simulation focuses on the USP apparatus II. However, it is necessary to study the dissolution of tablets in the GI tract for more accurate results. Compared to traditional methods, the LBM is good at dealing with the complex boundaries in the GI tract.
3. By coupling the LBM with the DEM, we can perform, for the first time, a real-time simulation of the entire dissolution process of the tablet in the USP apparatus II.

Because of the efficiency of the LBM, this model could be further developed for more accurate simulations.

The LBM–DEM coupling scheme is capable of simulating both the hydrodynamics in the USP apparatus II an;d the behavior of particles during the dissolution test. This allows us to study the kinetics behind the dissolution of tablets at the scale of tablet particles, enabling the possibility of designing different formulations and of testing the dissolution profile using this simulation platform.

1.3 Mathematical models

In this chapter, the mathematical models used in this project are outlined. Our simulation includes three parts: the fluid phase, which is simulated with the LBM; the solid phase, which is simulated with the DEM; and the coupling between the solid phase and fluid phase.

1.3.1 The LBM

As a CFD method, the LBM could recover the Navier–Stokes equation by solving the Boltzmann transport equation [42, 51, 52]. The LBM originates from the lattice gas automata (LGA) method, which was developed in the 1970s [53]. In the 1980s, the LGA method was extended into the LBM method [54, 55]. The LBM could simulate the fluid hydrodynamics without directly solving the Navier–Stokes equation. The LBM could be used to simulate a wide range of hydrodynamics [42]. The complex environments, such as porous media and other boundary conditions, could be easily implemented in the LBM, which would otherwise be difficult to simulate using traditional CFD methods [47, 56, 57]. Also, because the non-linear operations are computed locally, the LBM programs could be easily parallelized to enable large-scale simulations on CPUs and GPUs [58-61]. The LBM could, therefore, reach second-order accuracy in both time and space [62, 63].

As a relatively new method, the LBM has drawn increasing attention. Several projects have been established to develop lattice Boltzmann solvers. The *openLB* package is an object-oriented implementation of the LBM, and it supports parallel simulation with MPI [64]. *Palabos* follows a similar design framework with *openLB* and provides a flexible framework for extension [60]. It also supports parallel computation with the help of MPI. For parallel simulation with multiple

CPUs and GPUs, packages such as *WaLBerla* [65] and *Sailfish* [66] are available. All of the packages mentioned here are open-sourced.

In our study, *Palabos*, a lattice Boltzmann solver, was used to realize 3D parallel simulations [60]. As a community-supported software, *Palabos* is well maintained to provide various pre-designed features and is easy to extend to meet different computing needs [67]. Besides that, it has a high parallelization efficiency, which is essential for large-scale simulation.

From the Boltzmann transport equation to the LBM

This section introduces the principle of the LBM [68, 69]. Orientated from Ludwig Boltzmann's kinetic theory, the LBM treats the fluid or gas as a space distributed with a large number of small particles. These particles will move randomly and collide with one another. During the collision process, the energy and momentum of the particles will be exchanged with one another.

The Boltzmann transport equation, as shown in Eq. 1.1, highlights the essence of the LBM. In this equation, f is the probability of observing particles at a specific time and space (which is also called the particle distribution function), $\boldsymbol{u}$ is the velocity of the particle, and Ω is the collision term that epitomizes the driving force(s) that cause the change in the distribution function f over time t:

$$\frac{\partial f}{\partial \mathrm{t}} + \boldsymbol{u} \cdot \nabla f = \Omega \qquad \text{Eq. 1.1}$$

The collision term could be approximated with the BGK scheme [70]. In BGK approximations, the assumption is that the fluid distribution f tends to reach a local equilibrium state of f^{eq} at each time step of $\frac{1}{\tau}$.

$$\Omega_{BGK} = -\frac{1}{\tau}[f - f^{eq}] \qquad \text{Eq. 1.2}$$

By replacing Ω in Eq. 1.1 with Ω_{BGK} in Eq. 1.2, we can derive the discrete form from the LBM.

$$f_\alpha(\boldsymbol{x} + \boldsymbol{e_\alpha}\delta t, t + \delta t) - f_\alpha(\boldsymbol{x}, t) = -\frac{1}{\tau}\left[f_\alpha(\boldsymbol{x}, t) - f_\alpha^{eq}(\boldsymbol{x}, t)\right] \qquad \text{Eq. 1.3}$$

The idea of the LBM has simplified the original Boltzmann transport equation by representing the free moving particle to nodes in the lattice. For a 2D LBM modelwe can obtain a

D2Q9 model by restricting the streaming to 9 directions (including one direction that does not move), as shown in Figure 1.1.

The left-hand side of Eq. 1.3 is the streaming term, and the right-hand side of Eq. 1.3 is the collision term. As shown in Figure 1.2, the particles will exchange energy and momentum with each other during the collision term; during the streaming term, the particles will move forward to the next position at the next timestep.

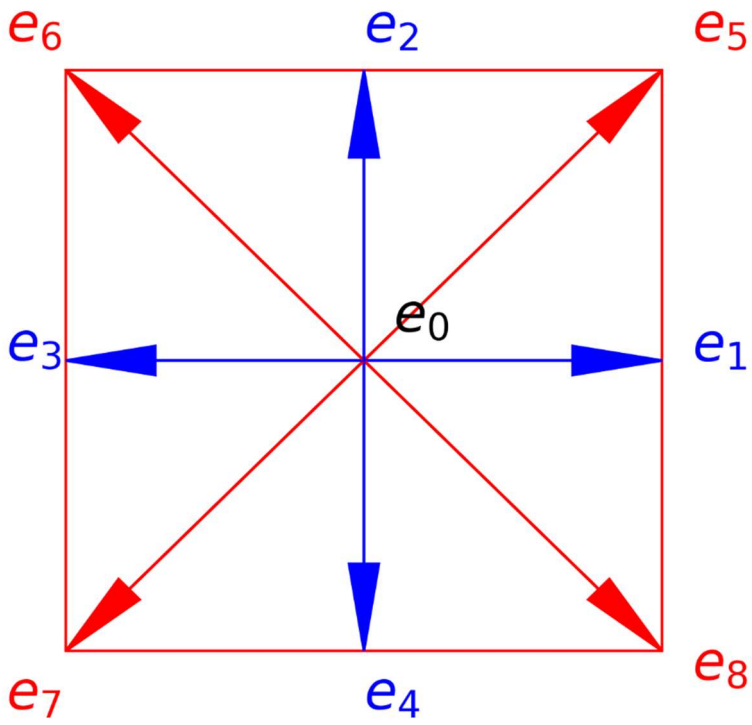

Figure 1.1. D2Q9 model velocity vector on the lattice. Each node could stream to 9 directions (including a static one), as indicated by the arrows.

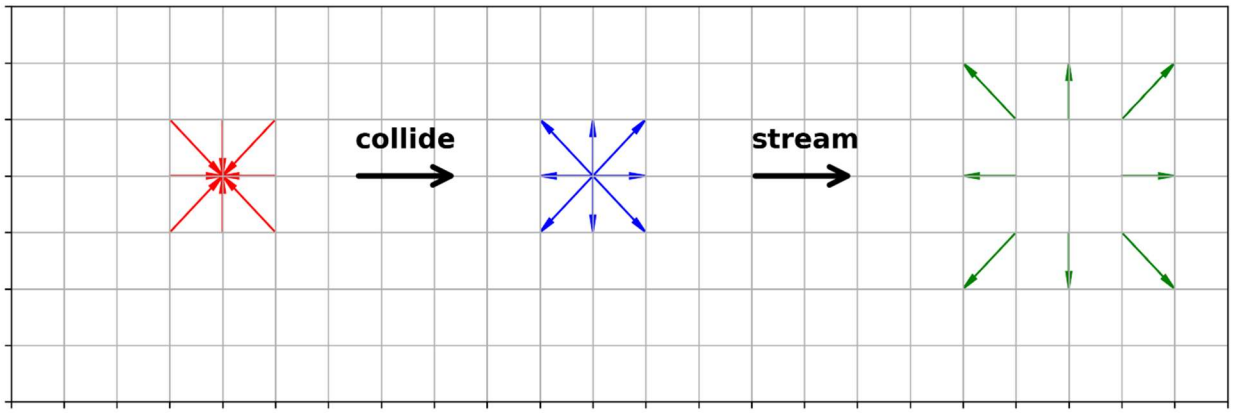

Figure 1.2. Movement of vectors during the collision and streaming step in the LBM [71]. During the collision step, the particles will exchange momentum and energy to reach the local equilibrium state. During the streaming phase, the particle will move to the next position in the next timestep.

The fluid viscosity v is calculated with the dimensionless relaxation time τ as shown below, where c_s is the lattice sound speed.

$$v = \mathrm{c}_s^2 \left(\tau - \frac{1}{2}\right) \delta t \qquad \text{Eq. 1.4}$$

The macroscale parameters, such as the fluid density ρ and velocity $\boldsymbol{u}$, are calculated as below.

$$\rho = \sum_{\alpha=0}^{q} f_\alpha \,, \boldsymbol{u} = \frac{1}{\rho} \sum_{\alpha=0}^{q} f_\alpha \, \boldsymbol{e_\alpha} \qquad \text{Eq. 1.5}$$

The LBM for concentration simulation

To model the dissolution of drug particles, we also need to simulate the scalar field, such as drug concentration or density distribution. The LBM could be used for scalar field distribution simulations as shown below.

$$g_\alpha(\boldsymbol{x} + e_\alpha \delta t, t + \delta t) - g_\alpha(\boldsymbol{x}, t) = -\frac{1}{\tau'} [g_\alpha(\boldsymbol{x}, t) - {g_\alpha}^{eq}(\boldsymbol{x}, t)] \qquad \text{Eq. 1.6}$$

Similarly, the local equilibrium distribution function ${g_\alpha}^{eq}(\boldsymbol{x}, t)$ could be expressed as below.

$${g_\alpha}^{eq} = \mathrm{Cw}_\alpha \left[1 + \frac{1}{2} \frac{\boldsymbol{u} \cdot \boldsymbol{e_\alpha}}{c_s^2} + \left(\frac{\boldsymbol{u} \cdot \boldsymbol{e_\alpha}}{c_s^2}\right)^2 - \frac{u^2}{2c_s^2}\right] \qquad \text{Eq. 1.7}$$

To compute the concentration or density of drug C, we used a similar method:

$$C = \sum_{\alpha=0}^{q} g_\alpha \qquad \text{Eq. 1.8}$$

Also, the diffusion coefficient D is related to the relation term τ':

$$D = \mathrm{c_s^2}\left(\tau' - \frac{1}{2}\right)\delta t \qquad \text{Eq. 1.9}$$

Similar to the D2Q9 model, we also need to define the discrete velocity vectors $\boldsymbol{e_\alpha}$ and weighting factors w_α on each direction in the D3Q19 and D3Q7 models. Our method used the D3Q19 model for velocity field simulations and the D3Q7 model for concentration field simulations [72, 73].

In our simulation, a solid particle dissolves into the fluid, where a source term C_w represents the mass transfer of drug from the solid particle to fluid.

$$g_\alpha(\boldsymbol{x} + \boldsymbol{c_\alpha}\delta t, t + \delta t) = g_\alpha^+(\boldsymbol{x}, t) + 2w_\alpha C_w \qquad \text{Eq. 1.10}$$

Until now, with the lattice Boltzmann method, we could simulate both the velocity field and drug concentration field in the dissolution apparatus.

Turbulence flow simulation in LBM.

Due to the nature of our simulation, the Reynolds number of the USP apparatus II flow could be as high as 4939 [28]. As a result, we need to implement the model to simulate the turbulence flow. DNS of turbulent flow with the LBM model are possible [74-76]. However, this will be highly computationally expensive. For the sake of efficiency, Smagorinsky models are proposed for approximation of the unresolved physics [77]. In the Smagorinksy model, the unresolved turbulence is treated as additional turbulent viscosity.

$$v_t = (C\Delta)^2|S| \qquad \text{Eq. 1.11}$$

In the equation, $|S| = \sqrt{S_{\alpha\beta}\mathrm{S}_{\alpha\beta}}$ is the norm of strain rate tensor. C is the Smagorinsky constant, which is typically in the range of 0.1–0.2, and Δ is the filter width. For the LBM, $\Delta = \Delta\mathrm{x}$. Our project uses the constant Smagorinsky constant C; consequently, this method is also termed the "Static Smagorinsky" method.

1.3.2 Discrete element method

Based on Newton's second and third laws of motion, the DEM tries to simulate the motion of a set of particles that interact with each other. The DEM is developed from the molecular dynamics (MD) method, which is used to model the interactions between atoms and molecules [78-80]. Later, this method is applied to study granule materials, which leads to the development of the DEM [81]. The DEM has wide application in engineering and science.

Various software and packages have been developed for the DEM simulation, some of which are commercial software, such as *Rocky DEM* ® and *EDEM* ®. Some of the open-sourced packages are *LAMMPS* [82], *LIGGGHTS* [83], *Yade DEM* [84], and *Granoo* [85, 86]. The *LAMMPS* packages were initially developed for simulating molecular dynamics. The *LIGGGHTS* project was built based on *LAMMPS* and provides support for granular material modeling as well as for more sophisticated contact models for DEM simulation.

In the following section, we will first introduce the basic principles and equations relevant to the DEM. Then we will focus more on the Edinburgh Elasto-Plastic Adhesion (EEPA) contact model, which is the primary model we use for tablet compression simulation.

Basic equations and principles of the DEM

In this project, we apply the DEM to model the interactions between particles and the interaction between particles in the USP apparatus II device. The DEM simulates the motion of particles based on Newton's second law, as shown in Eq. 1.12 where F is the total force, m is the mass, and a is the acceleration.

$$F = ma \qquad \text{Eq. 1.12}$$

The total force F includes three components: the normal force F_c, the tangential force T_c, and the external force F_{ext} from the environment. F_c and T_c are called the contact force.

$$F = F_c + T_c + F_{ext} \qquad \text{Eq. 1.13}$$

There are various models for contact forces. In our model, Hertz–Mindlin's contact force law is used to model the bulk particle interaction [87-91]. In this model, the normal force includes two components: the spring force and the damping force, as shown Eq. 1.14. Similarly, the tangential force has two components: the shear force and the damping force, as shown Eq. 1.15.

$$F_c = k_n \delta_{n_{ij}} - \gamma_n v_{n_{ij}} \quad \text{Eq. 1.14}$$

$$T_c = k_t \delta_{t_{ij}} - \gamma_t v_{t_{ij}} \quad \text{Eq. 1.15}$$

In the above two equations, k_n and k_t are the elastic constants of normal and tangential contact. δ_{nij} and δ_{tij} are the normal and tangential overlap of the distance between two particles. γ_n and γ_t are the viscoelastic damping constants of normal and tangential contact. v_{nij} and v_{tij} are the relative velocities of normal and tangential components.

In the above equations, e is the coefficient of restitution, Y is Young's modulus, v is the Poisson ratio, μ_s is the coefficient of static friction, μ_r is the coefficient of rolling friction, m is the mass of the particle, R is the radius of the particle. The subscripts i and j represent the two particles in contact. The superscript * of a value means that the value was calculated with the values of particles i and j.

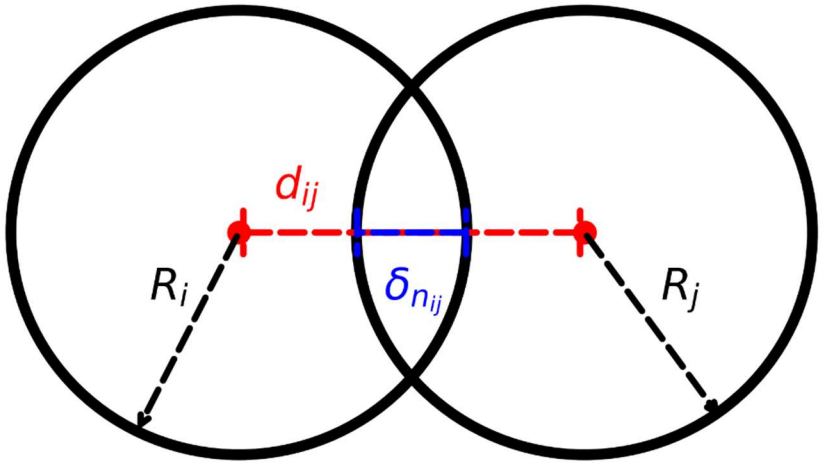

Figure 1.3. DEM particle interaction. The contact force is calculated based on the overlap between particles. When two particles get close to each other, the overlap $\delta_{n_{ij}}$ between two particles is calculated by calculating their relative *distance* d_{ij} (shown in the red line*)* and the radius *(*R_i *and* R_j*)* of these particles.

We can notice from the equations governing the DEM that the key is to check whether the particles overlap with each other and to calculate the overlap $\delta_{n_{ij}}$ between particles. Take the normal force as an example; to calculate the overlap between particles, we need to calculate the relative position d_{ij} and radius *(*R_i and R_j*)* of two particles, as shown in Figure 1.3. So, the overlap could be calculated below as shown below:

$$\boldsymbol{\delta_{n_{ij}}} = R_i + R_j - d_{ij} \qquad \text{Eq. 1.16}$$

If $\delta_{n_{ij}}$ is positive, this means that the two particles overlap with each other. Otherwise, this means the two particles do not overlap with each other.

The EEPA model

The Hertz–Mindlin model that we described in the last section could not be used to study the tablet compression process because this model could not simulate the loading and unloading of the tablet compression process. As a result, we will use the EEPA contact model [92-95]. In the EEPA model, the adhesive force is considered the combination of several different forces, such as *van der Waals* forces, sintering and chemical bonding, electrostatic forces, mechanical forces, etc. In this model, the total force $\mathbf{f_n}$ is the sum of EEPA hysteretic component f_{hys} and damping (dashpot) component f_{nd}.

$$\boldsymbol{f_n} = (f_{hys} + f_{nd})\mathbf{u} \qquad \text{Eq. 1.17}$$

The EEPA hysteretic component includes three phases, as described with three equations in Eq. 1.18. When the exponent parameter n=1, the EEPA model is a linear model, as shown in the left figure; when n>1, the model is non-linear.

$$f_{hys} = \begin{cases} f_0 + k_1\delta^n & \delta^n < k_2(\delta^n - \delta_p^n) \\ f_0 + k_2(\delta^n - \delta_p^n) & \delta^n < k_2(\delta^n - \delta_p^n) < k_1\delta^n \\ f_0 - k_{adh}\delta^n & k_2(\delta^n - \delta_p^n) < k_{adh}\delta^n \end{cases} \qquad \text{Eq. 1.18}$$

There exists a pull-off force f_0, which is constant. The EEPA model includes three phases:

1. The loading phase: As the overlap δ between two particles increases, the hysteretic force will increase eighter linearly (n=1) or non-linearly (n>1) following the k_1 branch. This is called the loading phase and is represented with the red line in the figures. The loading phase stops when the overlap reaches δ_{max}.
2. The unloading/reloading phase is represented with the green line in the figures. During the unloading phase, the overlap between the particles decreases. The stiffness in this phase will become k_2 due to the plastic deformation of the particles. When the force f_{hys} becomes 0, the corresponding overlap is called plastic overlap δ_p. When

reloading happens, the overlap between particles will increase. If the reloading force exceeds the maximum force in the loading phase, the stiffness will revert back to k_1.

3. The adhesive phase: When the overlap between particles continues to reduce beyond δ_p, an adhesive force that attracts the particles will be created. The adhesive force will reach a minimum value of f_{min} if the overlap continues to decrease. After f_{min} is reached, the adhesive force will increase with a slope of k_{adh}. The minimal value of f_{min} is calculated below, where $\Delta\gamma$ is the surface adhesion energy and a is the contacting radius.

$$f_{min} = \frac{3}{2}\pi\Delta\gamma a \qquad \text{Eq. 1.19}$$

The damping (dashpot) component f_{nd} is calculated below:

$$f_{nd} = \beta_n v_n \qquad \text{Eq. 1.20}$$

where v_n is the magnitude of the relative normal velocity, and β_n is the normal dashpot coefficient.

In a similar approach that used the DEM to simulate the tableting process, an elastic repulsion model when particles are pushed against each other was used reciprocally to describe their attraction when pulled apart [96].

1.3.3 The LBM–DEM coupling method

To study the behavior of drug particles in fluid in the USP apparatus II, we need to couple the solid DEM particles with fluids in LBM. Based on the ratio between the diameter of the particles and the size of the lattice node, two kinds of coupling methods are used, as shown in Figure 1.4. In the resolved coupling method, each particle will occupy multiple lattice nodes, and the interaction between the DEM and LBM is usually done in two-way. The coupling method is good at dealing with complex structures and the interaction between fluid and particles. The other approach is called unresolved coupling, where the particle size is significantly smaller than the size of the lattice node. This method could be used when we do not need to solve the interaction between fluid and particles. We use the existing drag laws to obtain the force on the particles from the fluid.

In our simulation, we use the resolved simulation for tablet dissolution. However, when the particle size is much smaller than the lattice node due to particle dissolution, we treat the particles as unresolved.

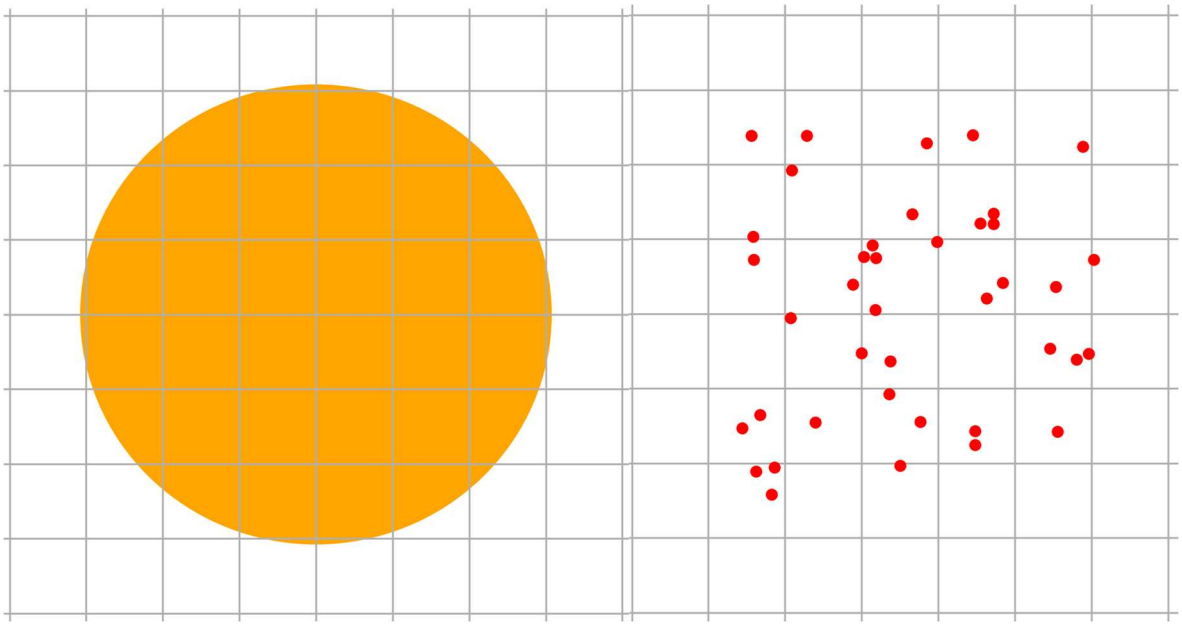

Figure 1.4. Resolved (right) and unresolved (right) models in LBM–DEM coupling methods. When multiple nodes cover the particles, it is called resolved coupling. When the particles are much smaller than the particles, it is considered unresolved coupling.

Immersed moving boundary method

For resolved coupling between DEM and LBM, different methods have been proposed. One method proposed by Mei et al. interpolates population to the surface of particles and uses bounce-back to calculate the exact velocity of fluid [62, 97]. Although this method is considered second-order accurate, it is a non-local computation that is demanding in computation resources. Another more straightforward method by Ladd [98, 99] uses a simple bounce-back scheme to calculate the fluid velocity other than a moving boundary. This local computation is efficient. However, because it represents the existence of particles in a lattice node with 1 or 0, this will cause high fluctuations during computation. Furthermore, it can only reach the first-order accuracy for moving particles. To overcome the shortage of the previous two models, Noble and Torczinsky [15] proposed a method that combines two models. Instead of calculating the exact shape of bounce-back and collision in each node are interpolated based on the ratio of each node occupied by the solid particle. This method only has local computation and can represent the solid particle in a relatively accurate way. Thus we used this method implemented by Seil [16, 100] as the based model for developing our model for tablet disintegration and dissolution. This method is also called the IMBM.

In the IMBM, we represent the shape of a particle in LBM by calculating the solid ratio of each lattice node [15]. At each node, we replace the standard BGK collision term with the new term, as shown below.

$$\Omega = \frac{1}{\tau}(1-B)(f^{eq}-f) + B\Omega^{S} \quad \text{Eq. 1.21}$$

The new collision term interpolates between the standard BGK collision term and the bounce-back term Ω^S, where B is calculated with the solid ratio ε on this node.

$$B = \frac{\varepsilon(\tau-0.5)}{(1-\varepsilon)+(\tau-0.5)} \quad \text{Eq. 1.22}$$

Ω^S is the bounce-back term when liquid hitting the particle with a velocity of $\boldsymbol{U}_S$:

$$\Omega^{S} = f_{-}(\boldsymbol{x},t) - f(\boldsymbol{x},t) + f^{eq}(\rho,\boldsymbol{U_s}) - f_{-}^{eq}(\rho,\boldsymbol{u}) \quad \text{Eq. 1.23}$$

where $\boldsymbol{U}_S$ is the velocity of the solid node. $f_{-}(\boldsymbol{x},t)$ is calculated by setting e_i to $-e_i$ in $f(\boldsymbol{x},t)$, this term describes the fluid description after collision with the solid particle.

With the equations above, we can simulate the fluid-solid interaction efficiently. To calculate the hydrodynamic force $\boldsymbol{F}_f$ and torque $\boldsymbol{T}_f$ experienced by a solid particle, we can calculate these two values by summing up the force and torque on each node partially occupied by the solid particle:

$$\boldsymbol{F_f} = c\,h\left[\sum_{n}\left(B_n\sum_{\alpha}\Omega_{\alpha}^{s}\,e_{\alpha}\right)\right] \quad \text{Eq. 1.24}$$

$$\boldsymbol{T_f} = c\,h\left\{\sum_{n}\left[(x-x_C)\times\left(B_n\sum_{\alpha}\Omega_{\alpha}^{s}\,e_{\alpha}\right)\right]\right\} \quad \text{Eq. 1.25}$$

where c is the speed of lattice, h is the unit length of each lattice node and $c = h/\Delta t$ with Δt being the time step in LBM simulation. In the above two equations, n is the number of lattice nodes that are partially occupied by the solid particle, and α is the discrete direction of a lattice node.

We can calculate the movement of particles with Newton's law of motion described in Eq. 1.26 and Eq. 1.27 . We consider three significant forces which impact particle movement: $\boldsymbol{F_c}$ is the contact force calculated in LIGGGHTs due to particle-particle collision. $\boldsymbol{F_f}$ is the hydrodynamic force calculated in Eq. 1.24. The gravity is mg. T_c and T_f are the corresponding toques of the contact force and hydrodynamic force. The particle mass is m, the moment of inertia is I, acceleration is a, and angular acceleration is $\ddot{\theta}$.

$$ma = F_c + F_f + mg \quad \text{Eq. 1.26}$$

$$\mathrm{I}\ddot{\theta} = T_c + T_f \quad \text{Eq. 1.27}$$

We can calculate the translation and rotation of particles with the above two equations.

1.3.4 DEM particle mass transfer to LBM fluid

To simulate the dissolution of drug particles, we need to model the mass transfer from DEM particles to LBM fluid. Our simulation simulates the dissolution process and convection-diffusion process in two sequential steps. The Noyes-Whitney equation governs dissolution, and convection-diffusion is simulated with the LBM.

As shown in Eq. 1.30Eq. 1.29, C_w is the source term, representing the change of drug concentration from solid DEM particles to fluid. Noyes-Whitney equation is the governing equation for drug particle dissolution, as shown below [101]. In this equation, A is the surface of the solid particles (m^2), K is the dissolution constant (m/s), C is the local concentration, C_s is the saturated concentration (kg/m^3), W is the mass of the particle (kg), and t is time (s).

$$\frac{dW}{dt} = -\mathrm{KA}(\mathrm{C_s} - \mathrm{C}) \quad \text{Eq. 1.28}$$

To connect the LBM with the DEM, for the lattice node covered with the DEM particle, the source term is expressed as below, where δt is the unit physical timestep and δx is the unit physical length of each lattice node.

$$C_w = -\frac{\delta t}{\delta x}\mathrm{K}(\mathrm{C_s} - \mathrm{C}) \quad \text{Eq. 1.29}$$

The radius of DEM particles could be updated based on the mass flux from the surface of particles to the lattice, as shown below:

$$\frac{d}{dt}\left(\rho_s \frac{4\pi}{3}\left(r^i\right)^3\right) = -\int_{A^i} \xi dA \quad \text{Eq. 1.30}$$

In the above equation, the ξ is the mass flux (mass dissolved per unit time at per unit lattice cell), ρ_s is the density of particle, and r_i is the radius of *ith* particle in DEM model.

With Eq. 1.29 and Eq. 1.30, we connect the DEM model with LBM, which could update the particle's radius based on the mass transfer from DEM particle to fluid.

1.4 The architecture of the model

After we have discussed the mathematical methods we used in our project, we give an overview of the architecture of the model used in our project. As shown in Figure 1.5, our model includes two parts: the DEM for drug particle simulation and the LBM for liquid simulation. These two methods are coupled together with the IMBM and the mass transfer model described previously.

The algorithm for LBM–DEM coupling could be described below:

1. Initialize parameters and generate tablet model
2. Calculate fluid movements with the LBM
3. Evaluate fluid velocity (L1) density, and drug concentration (L2)
4. Based on IMBM, calculate the force on particles and pass this force to DEM particles.
5. Calculate the motion of DEM particles with Newton's second law, update the particle radius based on the mass transfer model.
6. Pass the DEM particle velocity and position to the LBM.
7. Update LBM distribution functions and go to step 2 until the maximum time steps are met

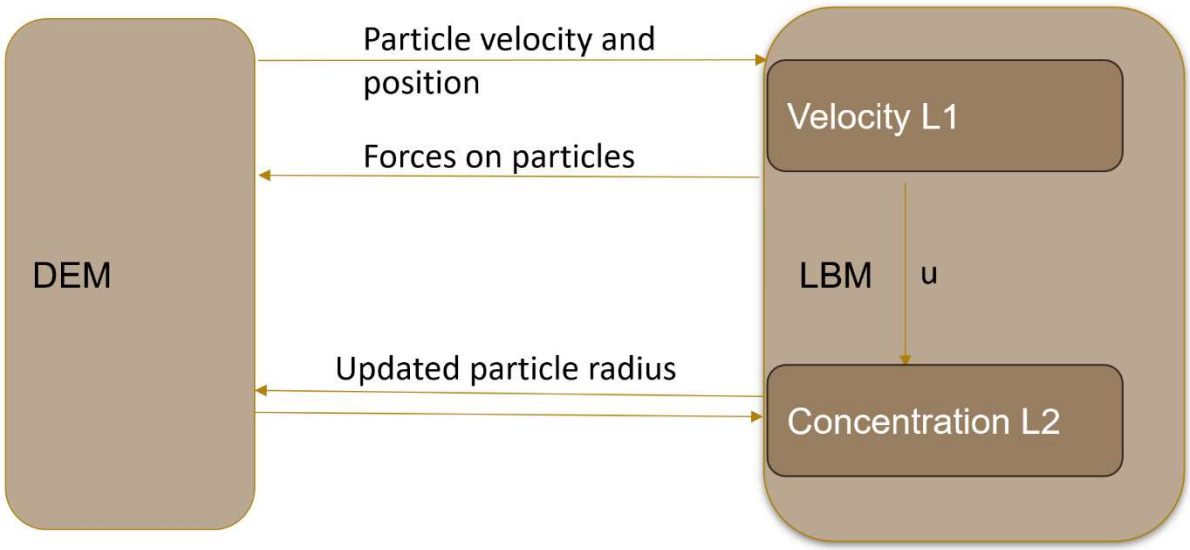

Figure 1.5 Overview of LBM DEM coupling algorithm.

1.5 Design of this dissertation

In this chapter, we introduced the significance of this project and the mathematical approaches we used to build our model. In Chapter 2, we introduced a computational framework to couple the LBM and DEM, and we experimented to validate our model using coning effect as an example. In Chapter 3, we further developed our model to realize the real-time simulation of bulk particle dissolution. We first validated our model with a single-particle dissolution experiment. Then, we compared the dissolution of the bulk particles at different USP apparatus II rotation speeds and drug particle dissolution constants. In Chapter 4, we modeled tablet compression with the DEM and used the DEM-modeled tablet for tablet disintegration and dissolution. We designed different tablet formulations and compared the dissolution profiles with each other.

CHAPTER 2. SIMULATING PARTICLE DISSOLUTION IN DISSOLUTION DEVICES: DEVELOPMENT OF COMPUTATIONAL FRAMEWORK TO COUPLE DISCRETE ELEMENT METHOD WITH FLUID DYNAMICS

2.1 Abstract

Tablet is the most common dosage form, widely used and mass-produced around the world. The disintegration and dissolution kinetics of tablets play a critical role in determining the therapeutic outcome, as well as in evaluating the quality of tablet products and troubleshooting the manufacturing process. Modeling and predicting the disintegration and dissolution kinetics thus facilitates tablet manufacturing and quality control. It can further enable in vitro and in vivo correlation (IVIVC) and lead to patient-centric tablet design and production. In this report, we present a modeling and simulation approach of tablet disintegration and dissolution based on the first principles. We aimed to simulate hydrodynamics in a dissolution device with the lattice Boltzmann method (LBM) and couple with the discrete element method (DEM) of particle dynamics and dissolution. The multiscale approach allows modeling tablet construct as particle assemble and simulating disintegration of the tablet and dissolution of the individual particle under various hydrodynamic conditions. Simulation results demonstrate that our multiscale approach can reproduce experimentally observed dynamics in dissolution devices. The results further indicate the coupling between LBM and DEM.

2.2 Introduction

Formulating a drug in tablet form is widely accepted in the pharmaceutical industry, thanks to patient compliance and the feasibility of mass production. The drug release kinetics of a tablet determine its bioavailability. Testing disintegration and dissolution kinetics allows evaluation and optimization of the drug manufacturing process and makes it possible to establish *in vivo in vitro* correction (IVIVC). Standard devices are commonly used for the quality control of tablet production. Several compendial methods have been developed. As a widely used device, USP Apparatus II is relatively simple and straightforward to use. It consists of a rotating paddle in a cylindrical vessel [12] and generally requires one tablet in a large amount of buffer solution (e.g., 900 mL). Under a constant stirring rate (e.g., 50 rpm) and temperature (37°C), sampling of drug concentration is held at a particular position in the vessel at pre-determined time points. Because of the hydrodynamic environment, it remains questionable whether reliable and representative measurements can be obtained by the current compendial method [18, 102, 103].

Some of the variability could be avoided by careful calibration with calibrator tablets [104]. However, in some situations, variability and inconsistency persist even after calibration [19, 26, 104]. This is usually due to the complexity of hydrodynamic profiles near the rotation paddle in a testing apparatus [30]. With its rotating at 50 rpm under standard conditions, the paddle's tip is measured at 0.194 m/s with a Reynolds number as high as 4939 [28]. This suggests that the flow kinetics in the stirred vessel become heterogenous, as well as time dependent.

Experimental studies are reported in the literature for understanding the hydrodynamics within a dissolution device such as USP Apparatus II and its impact on drug release. The release of dye molecules from a tablet helped visualize the interplay between liquid flow and concentration distribution [18]. Laser-induced fluorescence (LIV) was utilized to gain quantitative information about tablet dissolution in USP Apparatus II [19]. It was shown that, by releasing fluorescent dye molecules from a tablet located at the bottom of a dissolution vessel, the mixing pattern and concentration distribution of drug particles or molecules with the dissolution media could be captured under the illumination of a planar laser. Laser doppler velocimetry was utilized to measure liquid velocities at a selected location in a dissolution apparatus [20, 21]. The measurement could yield quantitative information about fluid hydrodynamics at isolated points,

but obtaining a complete picture of the hydrodynamic field and concentration distribution is difficult with the current experimental means.

Conversely, the computation of fluidic dynamics and simulation of particle dissolution may provide a detailed understanding of the disintegration and dissolution kinetics of tablets. Compared with an experimental measurement, mathematical modeling is usually free of experimental errors due to operation and the surrounding environment [22-24]. In fact, there has been an increase in computational studies on tablet dissolution in dissolution devices reported in the literature. Some implemented computational fluid dynamics (CFD) to simulate detailed hydrodynamic evolution in USP Apparatus II [21, 25-30]. Simulation results are compared with experimental data obtained by laser Doppler velocimetry (LDV) and particle image velocimetry (PIV) [19, 25, 31]. CFD simulation can provide further insights into the dissolution kinetics of a tablet under mechanical flow. One study shows that the shear rate of liquid could dramatically vary along the bottom of the USP Apparatus II vessel, suggesting that the location of the tablet affects the testing results of the compendial method [30]. This is further confirmed by another simulation [27]. CFD simulation is also used to examine the impact of paddle agitation speeds on fluid strain rate distribution [32].

Apparently, CFD alone is not able to capture tablet formulation and how it influences the kinetics of tablet disintegration and dissolution. A geometry of a tablet may be integrated into a CFD simulation and fixated at a dissolution vessel to understand hydrodynamic conditions at the tablet surface. It is difficult to fully examine the interaction between the fluid phase and the solid tablet or particles in the methodology, especially when drug particles undergo dissolution. New computational methods are needed to couple fluid dynamics with tablet or particle dissolution in a testing device.

Tablet dissolution is preceded by disintegration, in which water absorption leads to swelling of excipient particles and subsequent repulsion among drug and excipient particles in a tablet. Numerical methods, including cellular automata and finite element method (FEM), have been used to simulate swelling of uniform particles [1, 35]. More flexible in modeling particles of different properties (such as size, density, and solubility), the discrete element method (DEM) was also utilized to simulate tablet swelling and dissolution [4]. DEM is widely used in the simulation of bulk particle behaviors.

In this study, we have developed an integration scheme to couple CFD and DEM to simulate tablet disintegration and dissolution in a dissolution device. Similar efforts have been reported. For example, by coupling CFD and direct numerical simulation (DNS) of drug particles, the dissolution process of particle dissolution under hydrodynamic conditions was simulated [39, 40]. Nonetheless, it appears in this reported study that only one way of coupling from CFD to DEM was achieved [40, 41], ignoring any possible impact of particle movement on liquid flow. To fully couple dynamics with particle dynamics, we have resorted to using the lattice Boltzmann method (LBM) for computing hydrodynamics and integrating DEM of simulations.

As an emerging CFD method, LBM has gained considerable attention [42-45]. Compared to traditional FEM- and FVM-based methods of CFD, LBM is simple to implement and more capable of dealing with complex boundaries and multiphase and multicomponent flows [47, 48]. Because of the nature of local dynamics, LBM can be easily implemented in parallel computation for conducting large-scale simulations [46]. More important for what we wanted to simulate, using LBM made it easier to implement the coupling between hydrodynamics and particle dynamics. There are generally two major coupling methods: the momentum exchange method (MEM) [49, 50] and the partially saturated cell method (PSM) [15]. In MEM, a particle is mapped into the fluid domain, and the occupied LBM lattice cell is treated as solid. By applying non-slid boundary conditions on the particle surface, hydrodynamic forces on the particle can be derived. Conversely, a counter-acting force with the same magnitude acts on the fluid. In PSM, interaction forces between the fluid and a particle are evaluated based on the ratio of volume filled by the particle in the occupied lattice cell(s) and are utilized in Boltzmann kinetic equations. PSM is also called the immersed moving boundary method (IMBM) and is used in our simulation platform.

In this report, we will discuss our integration approach between LBM and DEM via IMBM to simulate particle dynamics under hydrodynamics in USP Apparatus II, followed by simulation results and a comparison with experimental results from the literature. The methodology we used is similar to those reported by others [15, 16], but ours allows us to further integrate tablet disintegration and particle dissolution in our future publications.

2.3 Simulation methodology

We have implemented a multiscale simulation approach for studying the disintegration and dissolution kinetics of tablets in a dissolution device, including USP Apparatus II. Our research goal is to understand and, eventually, predict how formulation factors, manufacturing process, and tablet microstructure jointly influence the drug release kinetics of a tablet under various hydrodynamic conditions. In this report, we focus on our development of LBM and DEM coupling to be used in further studies.

2.3.1 LBM and DEM coupling

The lattice Boltzmann method (LBM) has been developed for computing hydrodynamics since the 1970s [53-55, 105]. Various review articles have been published on the methodology and its application [42, 47, 48, 106]. In brief, LBM treats fluid flow in a discretized lattice with particle or density distribution functions, from which the velocity and pressure of the fluid can be derived. The Boltzmann equation shown below, highlights the essence of LBM, where Ω is the so-called collision operator that epitomizes the driving force(s) causing the change in LBM's distribution function, *f*, over time.

$$\frac{\partial f}{\partial \mathrm{t}} + \mathrm{c} \cdot \nabla f = \Omega \qquad \text{Eq. 2.1}$$

In this equation, *c* is the lattice velocity. The collision term is generally unknown, but several empirical forms have been proposed, including the BGK model, developed by Bhatnagar, Gross, and Krook in 1954 [9], which is shown below:

$$\Omega = \omega(f^{eq} - f) = \frac{1}{\tau}(f^{eq} - f) \qquad \text{Eq. 2.2}$$

In this equation, ω is the collision frequency and τ is the relaxation factor. With the BGK simplification, the Boltzmann equation becomes:

$$f_\alpha(\boldsymbol{x} + e_\alpha \delta t, t + \delta t) - f_\alpha(\boldsymbol{x}, t) = -\frac{1}{\tau}[f_\alpha(\boldsymbol{x}, t) - f^{eq}(\boldsymbol{x}, t)] \qquad \text{Eq. 2.3}$$

The kinematic viscosity of the fluid is:

$$v_k = c_s^2 \left(\tau - \frac{1}{2}\right) \delta t \qquad \text{Eq. 2.4}$$

In Eq. 2.3, $f_\alpha(\boldsymbol{x},t)$ is the density distribution function along α discretization direction of a lattice point $\boldsymbol{x}$ at time t.; e_a is liquid velocity along α direction. The left side of the equation, also called "streaming," describes the change in distribution function resulting from the exchange of momentum between neighboring lattice nodes, for example, due to underlying bulk advection and molecular diffusion. Clearly, the dynamics of a liquid system is driven by the equilibrium distribution function, $f_\alpha^{eq}(\boldsymbol{x},t)$. Various schemes of simulation lattice and equilibrium distribution function have been developed and are widely used [74].

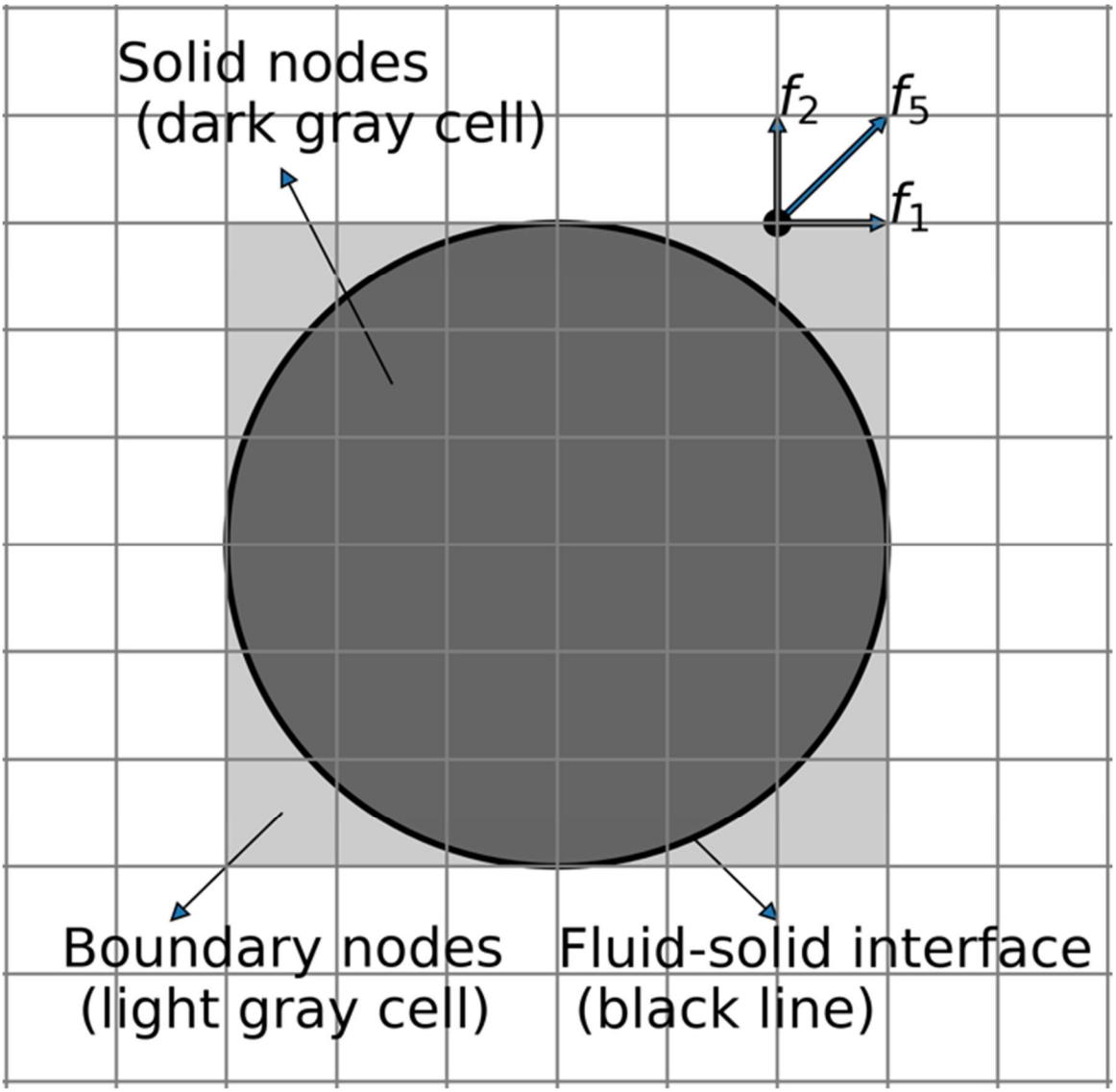

Figure 2.1. Solid particle (dark gray cell) in fluid (blank cell). The ratio of the solid part in a lattice cell is calculated based on the area of the dark grey part in a cell. The dark gray cells indicate the solid nodes, the light gray cells indicate the boundary nodes, and the blank white cells indicate the fluid nodes.

Solid particles are treated individually. Interaction between fluid and a solid particle is handled by the immersed moving boundary method [15]. At the fluid-solid interface (Figure 2.1), local solid and fluid velocities are kept the same by adding additional collision terms to the solid nodes:

$$\Omega = \frac{1}{\tau}(1 - B)(f^{eq} - f) + B\Omega^{S} \qquad \text{Eq. 2.5}$$

where B is determined by the solid ratio ε of a solid-occupied node:

$$B = \frac{\varepsilon(\tau - 0.5)}{(1-\varepsilon) + (\tau - 0.5)} \quad \text{Eq. 2.6}$$

In addition, Ω^S describes bounce-back of liquid hitting the particle:

$$\Omega^S = f_-(\boldsymbol{x}, t) - f(\boldsymbol{x}, t) + f^{eq}(\rho, \boldsymbol{U_s}) - f_-^{eq}(\rho, \boldsymbol{u}) \quad \text{Eq. 2.7}$$

Where $\boldsymbol{U}_S$ is the solid node's velocity at the next time step. $f_-(\boldsymbol{x}, t)$ is derived by setting the e_i to $-e_i$ in $f(\boldsymbol{x}, t)$. It describes the bounced back state of the distribution function when facing a solid node.

Subsequently, the hydrodynamic force $\boldsymbol{F}_f$ and torque $\boldsymbol{T}_f$ experienced by a solid particle can be evaluated by:

$$\boldsymbol{F_f} = c\ h\left[\sum_n (B_n \sum_i \Omega_i^s\ e_i)\right] \quad \text{Eq. 2.8}$$

$$\boldsymbol{T_f} = c\ h\left\{\sum_n \left[(x - x_C) \times (B_n \sum_i \Omega_i^s\ e_i)\right]\right\} \quad \text{Eq. 2.9}$$

Where c is the lattice speed, h is the unit lattice length, and $c = h/\Delta t$, with Δt being the time step in the LBM. In the equations, n is the number of lattices or nodes that are partially occupied by solid partial, i is a discrete direction of a lattice point. By summing up the impact of liquid on each affected node, it is possible to get the overall hydrodynamic force applied to a particle.

LBM allows the macroscopic kinematic viscosity u and density ρ calculated from the particle distribution function. In our simulation, we further considered fluid turbulence in the model, as it becomes significant when the Reynolds number reaches 5,000 or larger [28]. For this, a static Smagorinsky model is used, in which liquid viscosity is modified based on liquid velocity.

Particle movement is handled by Newton's law of motion described below. Three major forces are considered: $\boldsymbol{F_c}$ is the contact force due to particle-particle collision. $\boldsymbol{F_f}$ is the hydrodynamic force described in Eq. 2.8. The gravity is described as mg. T_c and T_f are the corresponding torques of F_c and F_f. The particle mass and moment of inertia are m and I respectively, while the acceleration and angular acceleration are a and $\ddot{\theta}$.

$$ma = F_c + F_f + mg \quad \text{Eq. 2.10}$$

$$I\ddot{\theta} = T_c + T_f \quad \text{Eq. 2.11}$$

With the equations, particle translation and rotation can be calculated.

2.3.2 DEM model:

To model the particle-particle interaction, we applied the discrete element method (DEM) to model the behavior of bulk particles in the USP apparatus II. There are various models for the contact forces. Here in our model, Hertz–Mindlin's contact force law is used [87].

$$F_c = k_n \delta_{n_{ij}} - \gamma_n v_{n_{ij}} \quad \text{Eq. 2.12}$$

$$T_c = k_t \delta_{t_{ij}} - \gamma_t v_{t_{ij}} \quad \text{Eq. 2.13}$$

Where k_n and k_t are the elastic constants of normal and tangential contact. δ_{nij} and δ_{tij} are the normal and tangential overlap of the distance between two particles. γ_n and γ_t are the viscoelastic damping constant of normal and tangential contact. v_{nij} and v_{tij} are the relative velocity of the normal and tangential components.

The parameters of k_n, γ_n, k_t, γ_t could be calculated as follows:

$$k_n = \frac{4}{3} Y^* \sqrt{R^* \delta_n} \quad \text{Eq. 2.14}$$

$$\gamma_n = -2\sqrt{\frac{5}{6}} \beta \sqrt{S_n m^*} \geq 0 \quad \text{Eq. 2.15}$$

$$k_t = 8G^* \sqrt{R^* \delta_n} \quad \text{Eq. 2.16}$$

$$\gamma_t = -2\sqrt{\frac{5}{6}} \beta \sqrt{S_t m^*} \geq 0 \quad \text{Eq. 2.17}$$

The parameters of S_n, S_t, *and* β, could be calculated with the following equations:

$$S_n = 2Y^* \sqrt{R^* \delta_n} \quad \text{Eq. 2.18}$$

$$S_t = 8G^* \sqrt{R^* \delta_n} \quad \text{Eq. 2.19}$$

$$\beta = \frac{\ln(e)}{\sqrt{\ln^2(e) + \pi^2}} \quad \text{Eq. 2.20}$$

$$\frac{1}{Y^*} = \frac{1 - v_i^2}{Y_i} + \frac{1 - v_j^2}{Y_j} \quad \text{Eq. 2.21}$$

$$\frac{1}{G^*} = \frac{2(2 + v_i)(1 - v_i)}{Y_i} + \frac{2(2 + v_j)(1 - v_j)}{Y_j} \quad \text{Eq. 2.22}$$

$$\frac{1}{R^*} = \frac{1}{R_i} + \frac{1}{R_j} \quad \text{Eq. 2.23}$$

$$\frac{1}{m^*} = \frac{1}{m_i} + \frac{1}{m_j} \quad \text{Eq. 2.24}$$

In the above equations, e is the coefficient of restitution, Y is Young's modulus, v is the Poisson ratio, μ_s is the coefficient of static friction, μ_r is the coefficient of rolling friction, m is the mass of the particle, and R is the radius of the particle. The subscripts of i and j stand for the two particles in contact. The superscript * of a value means the value calculated with the value of particle i and j.

2.4 Simulation setup

In our simulation that couples hydrodynamic and particle dynamic simulations, the LBM component was implemented by calling an open-source library, *Palabos* (Parallel Lattice Boltzmann Solver) [60]. Particle dynamics were modeled with *LIGGGHTS* (LAMMPS Improved for General Granular and Granular Heat Transfer Simulations), an open-source DEM library [107]. Coupling was done by another open-sourced library called LBDEM coupling [16, 100]. This coupling library will shuffle the parameters of particles such as coordinates, velocity, and radius between the LBM model and DEM model. The hydrodynamic force and torque on the particle are calculated based on Eq. 2.8 and Eq. 2.9. The force and torque on particles will further drive the movement and rotation of particles as an external force and torque on the particles. The overall algorithm is shown in Figure 2.2. A 3D model of USP Apparatus II was generated and ported to the LBM module (Figure 2.3). The shape and dimension of the paddle and vessel were designed following the specification of USP <711>[12]. The paddle was also implemented as an immersed

moving boundary. Thus, the rotation of the paddle will drive the movement of fluid. The hydrodynamic force from the fluid will further drive the movement of particles.

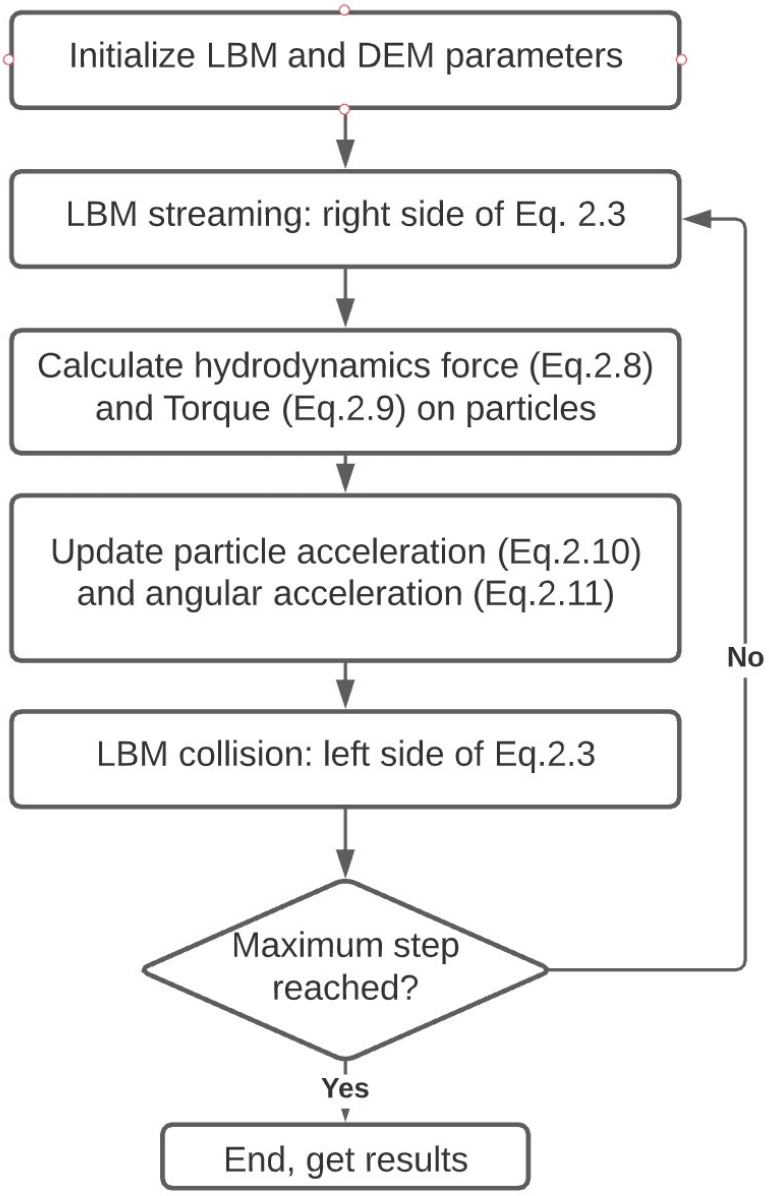

Figure 2.2. LBM-DEM coupling algorithm to simulate particle dynamics in liquid.

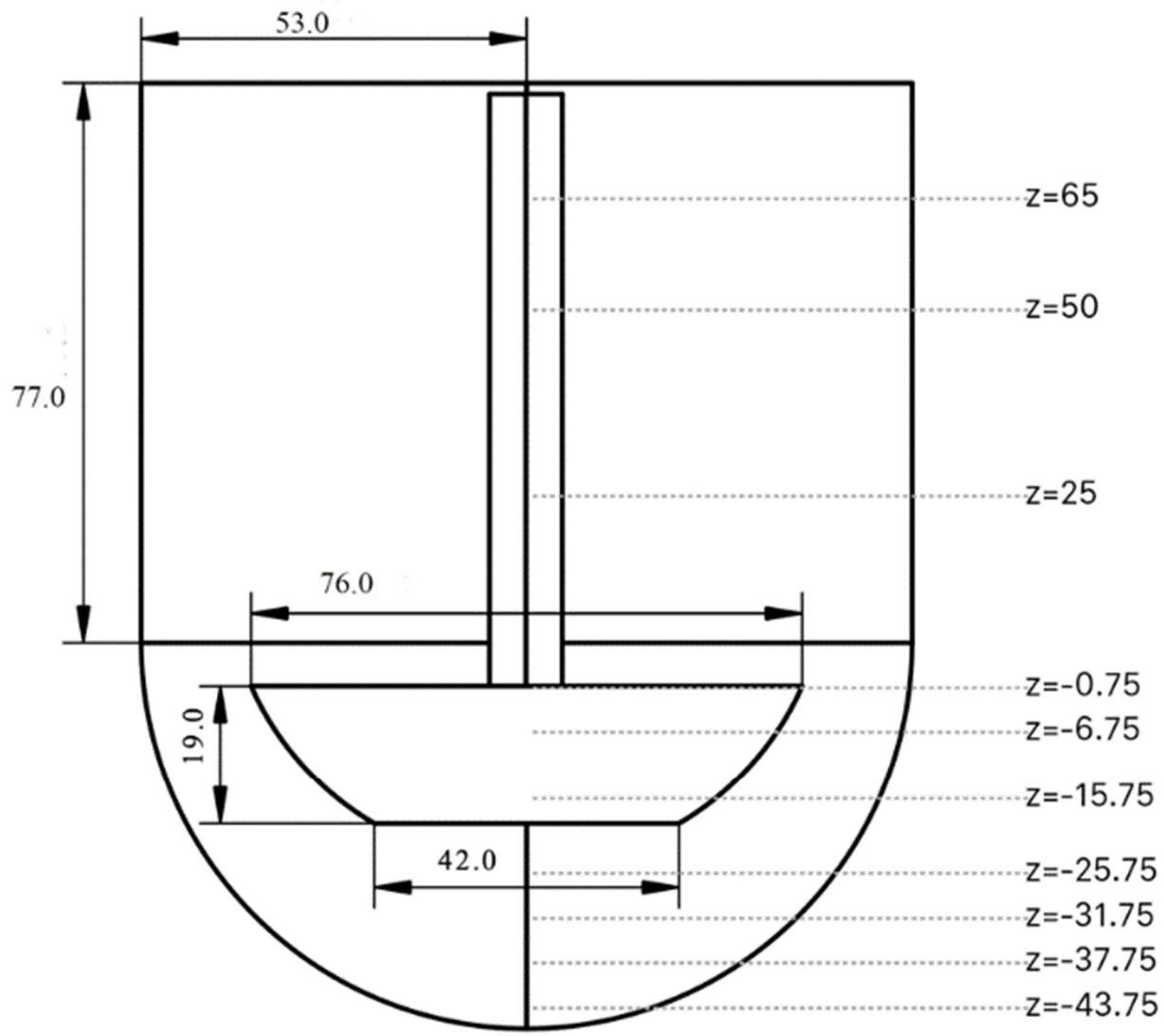

Figure 2.3. Shape of USP apparatus II, paddle, and vessel. Ten different iso-surfaces along the z-axis were selected for comparison with LDV data. All units are in mm.

Table 2.1 Parameters used in LBM-DEM Simulation

Temperature (T)	37 °C
Fluid Density (ρ_f)	993.3 kg/m³
Kinetic Viscosity (v_k)	6.97e-7 mm²/s
Water Volume (V)	1 L
Particle radius (R)	500 μm
Particle density (ρ_p)	1100 kg/m^3
Number of particles (N)	~1060
Young's modulus (Y)	6.13e6 Pa
Poisson's ratio (v)	0.225
Coefficient of restitution (e)	0.8
Coefficient of static friction (μ_s)	0.2
Coefficient of rolling friction (μ_r)	0.020
Timestep (dt)	6.67e-5(s)
Grid size	204 x 204 x 243

2.5 Results and discussion

Simulations were conducted based on the coupling approach described in the previous section. The first task was to perform only LBM calculations of hydrodynamics in the USP Apparatus II model and compare computed fluid velocities to experimental values reported in the literature. The second task was to run coupled LBM-DEM simulations and examine how the hydrodynamics determined particle dynamics in the apparatus.

2.5.1 LBM simulation of fluid in dissolution device

Using the simulation parameters shown in Table 2.1, we conducted LBM simulations without any solid particles present. Figure 2.4 shows the calculated results of liquid velocities in USP Apparatus II under 50 rpm after 300 seconds from the initial static state. The color intensities in the bottom of the panel correspond to the velocity scale. In contrast, the length and color of the streamlines in the right panel are commensurate with the scale and directionality of velocity. Liquid flow mainly occurs away from the vertical center of the vessel, where liquid velocities are the lowest. The paddle tip has the highest speed, driving fluid movement.

We further compared velocity values with experimental values determined by LDV [29]. As shown in Figure 2.3, we extracted velocity values at ten different positions along the z-axis from the simulation result and plotted them along with the LDV data. We decomposed each velocity into three directions—tangential, radial, and axial—and compared the scales with experimental values. Figure 2.5 shows tangential velocities from the simulation, superimposed with the literature data. We can generally observe an increase in tangential velocity from the center to the wall of the vessel along each horizontal line. Note that the origin along the X-axis of each figure is at the vessel center. The increase of tangential velocity results from the increasing velocity of the paddle along its axis. Along the vertical axis of the vessel from top to bottom, the largest position of velocity seems to shift from the center of the figure (or a quarter from the wall) towards the wall. Significantly, velocity values closely resemble those observed experimentally, especially the trends along the horizontal and vertical directions.

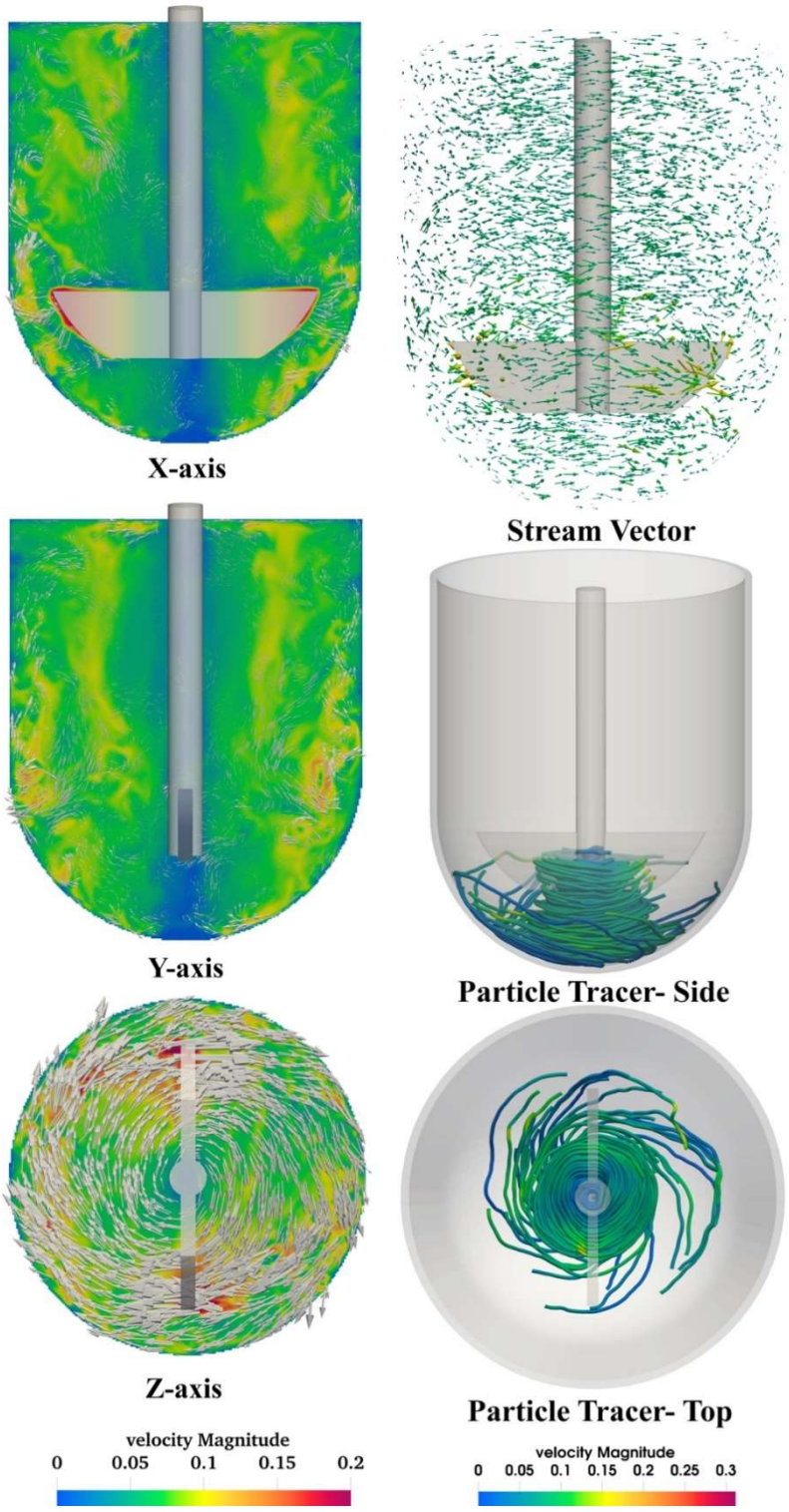

Figure 2.4 Left: Velocity distribution from X-axis, Y-axis, and Z-axis viewed under 50 rpm. Right top: Vector of stream velocity distribution in whole USP apparatus II. Right middle and bottom: particle movement tracer at the bottom of USP apparatus II.

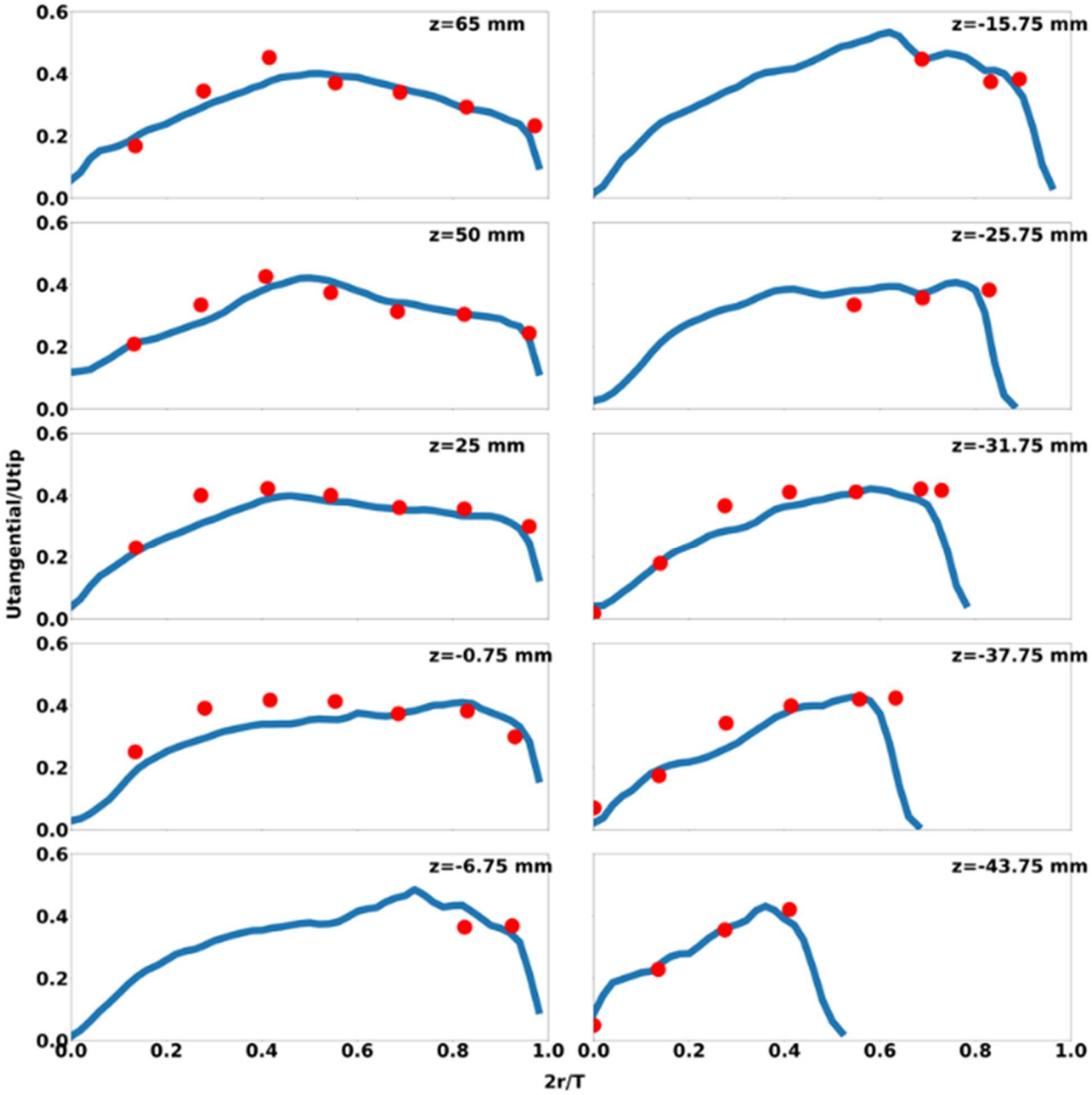

Figure 2.5. Comparison between LDV data and CFD predictions of tangential velocities on different iso-surfaces. The blue line represents simulation results, while the red dots are the LDV data.

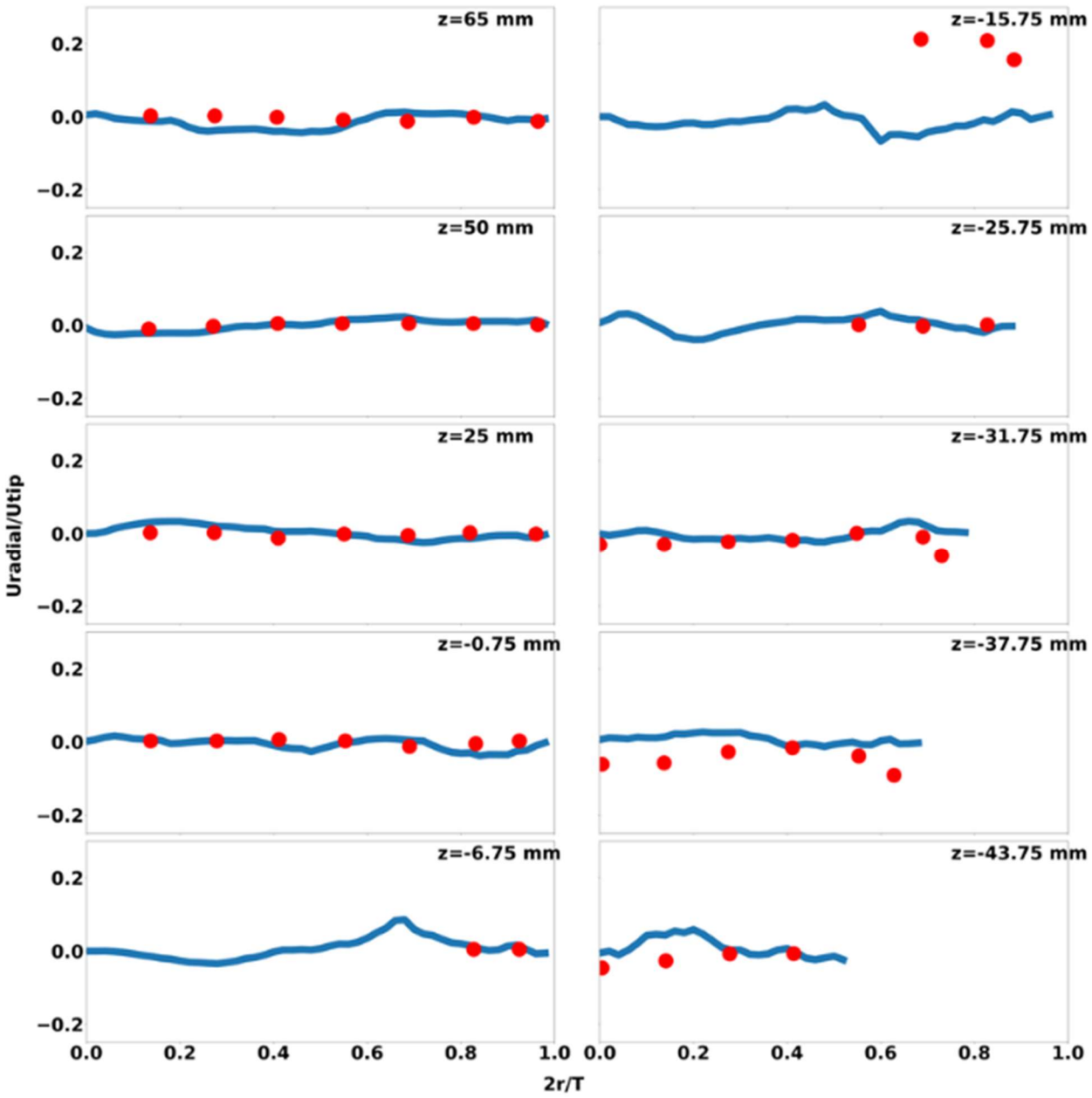

Figure 2.6. Comparison between LDV data and CFD predictions of radial velocities on different iso-surfaces. For radial velocity, positive values indicate that fluid moved out of the vessel center. The blue line represents simulation results, while the red dots are the LDV data.

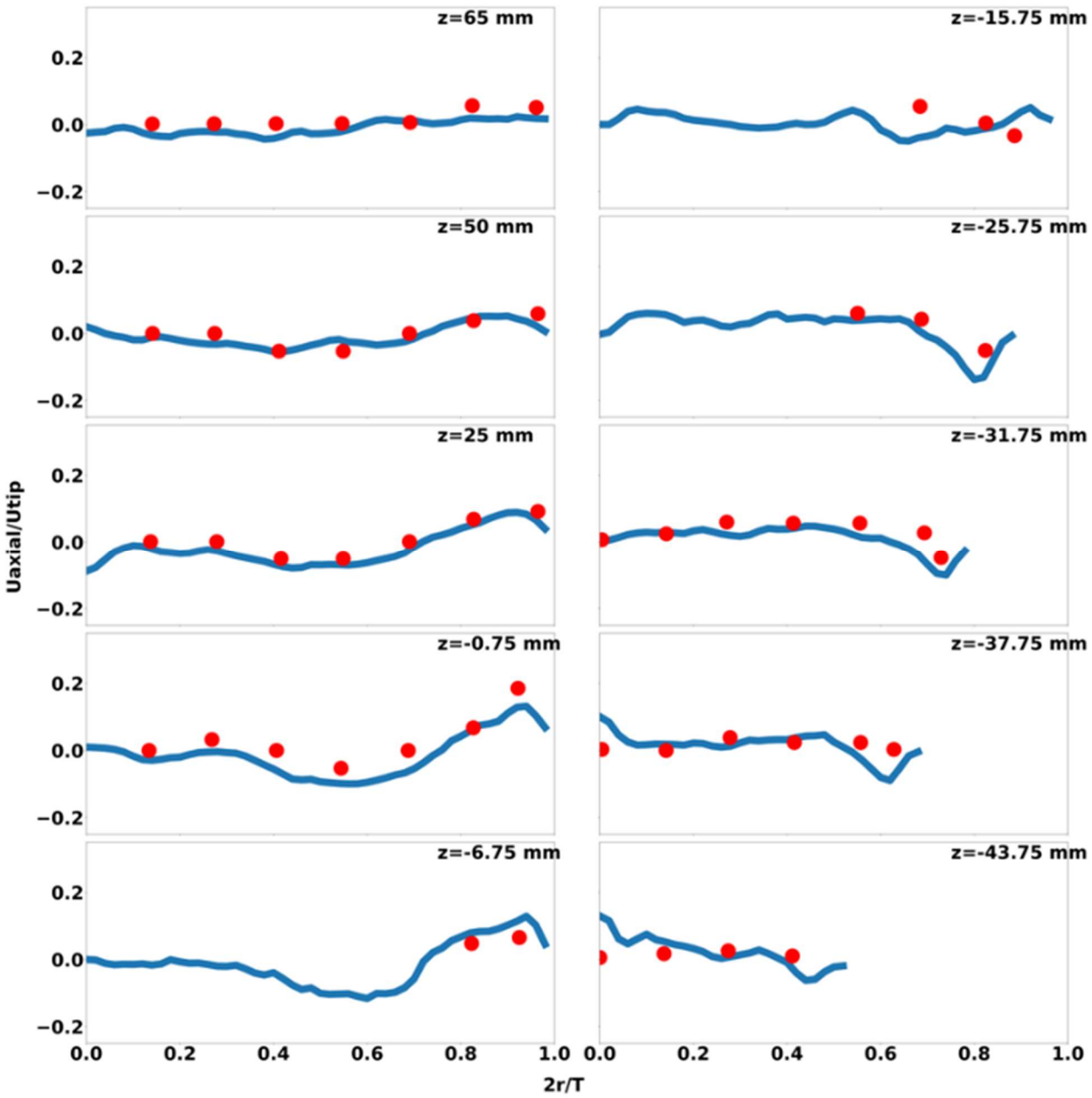

Figure 2.7. Comparison between LDV data and CFD predictions of axial velocities on different iso-surfaces. For axial velocity, positive values indicate fluid moving up. The blue line represents simulation results, while the red dots are the LDV data.

Figure 2.6 and Figure 2.7 show radial and axial velocity values calculated from the LBM simulation, respectively. The radial velocities center around near-zero; most values match experimental data, except for the z position at -15.75 mm. Given that other data points are closely matched, we suspect that the deviation may be caused by experimental errors resulting from possible interference of paddle movement with the laser measurement. For the axial velocity

distribution (Figure 2.7), most simulated values fluctuate around zero, especially at horizontal positions further away from the paddle (z = 65 and 50 mm). Upward flow can be seen near the wall at respective places above the paddle (z = 25, -0.75, and -6.75 mm). For the positions below the paddle, we observed upward flow. The half-moon shape of the paddle likely induced different flow patterns (Figure 2.3). The velocity on the paddle's top tip is higher than the velocity at its bottom tip. Based on Bernoulli's principle, the fluid will move upward from the lower part of the vessel to the upper part. This force, we believe, is the driving force for the drug particles to move upward in the USP apparatus II vessel.

2.5.2 Particle dynamics under hydrodynamics

Around one thousand solid particles were simulated in USP Apparatus II in 1L liquid under various rotational speeds of the paddle. Table 2.1 lists the computational parameters for the coupled DEM-LBM simulation. Figure 2.8 shows both fluid dynamics and particle velocities after 250 seconds from the initial state where particles were kept static at the center of the vessel bottom. We traced particle movement for 100 seconds, allowing several observations.

First, the streamlines of fluid show that liquid velocity positively correlates with the paddle's rational speed. Tracing of the fluid also suggests upward movement from the bottom of the vessel. Particle velocities are significantly affected by the paddle's stirring rate. At 50 or 60 rpm, all particles were concentrated at the bottom of the vessel. Particle path lines converge toward the center of the vessel. As the paddling speed increased, particle velocities and spatial distributions became more prominent, as illustrated by the streamlines (Figure 2.8). Particle path lines start to diverge, indicating that the particles move away from the vessel center. Particles also move faster at a higher paddle rotation speed, indicated by thicker path lines. The movement of the particles formed the so-called "coning effect," in which particle aggregation occurs at the bottom of the dissolution vessel due to insufficient agitation. From the illustrations of fluid dynamics (Figure 2.4 and Figure 2.8), it is apparent that the fluid velocities along the center axis are much smaller, contributing to the settling of solid particles. The coning effect seems to be reduced when the padding speed becomes more significant, as shown in Figure 2.9. From the histogram of particle frequency, or the number of particles that appear within a unit area, along the horizontal axis from the center of the vessel, the particle distribution becomes flattened and

extended to the wall at a higher padding speed. The inset images in Figure 2.9 also confirm the trend of broader spatial distributions as the stirring rate goes from 50 to 100 rpm.

There is empirical literature to derive the minimal rotation speed from fluid properties by which the coning phenomena disappear, NC_{rpm} (no coning rpm), by the Zwietering equation [108, 109].

$$\mathbf{NC}_{rpm} = \boldsymbol{A d_p^l} \left(\frac{\boldsymbol{\rho_p - \rho_f}}{\boldsymbol{\rho_f}} \right)^{\boldsymbol{m}} \left(\frac{\boldsymbol{\mu_f}}{\boldsymbol{\rho_f}} \right)^{\boldsymbol{n}} \quad \text{Eq.2.25}$$

Studies report that for non-viscous fluids such as dilute aqueous solution (<=2.1 mPa·s), constant parameters A, l, m, and n values are found to be 57, 0.22, 0.52, and -0.23 respectively [108-110]. For our simulations in which the diameter of particle d_p = 1000 μm, particle density ρ_p = 1.1 g/cm^3, fluid density ρ_f = 1.0 g/cm^3, and fluid viscosity μ_f = 0.692 mPa·s, NC_{rpm} is calculated as 85 rpm. From Figure 2.9, it seems that particles start to disperse more significantly when the padding speed reaches 85 rpm. The coning effect could be more drastic if we include more particles in the simulation. To further quantitatively evaluate particle movement, standard deviations (STD) of particle coordinates, as well as changes in the distance from the center of the vessel of the particles from the initial state, were calculated and plotted together as a function of paddling speed (Figure 2.10). Interestingly, the rotation speed determines both quantities linearly. The slope change of the STD line at 85 rpm may indicate a different behavior or dissipation of coning effect.

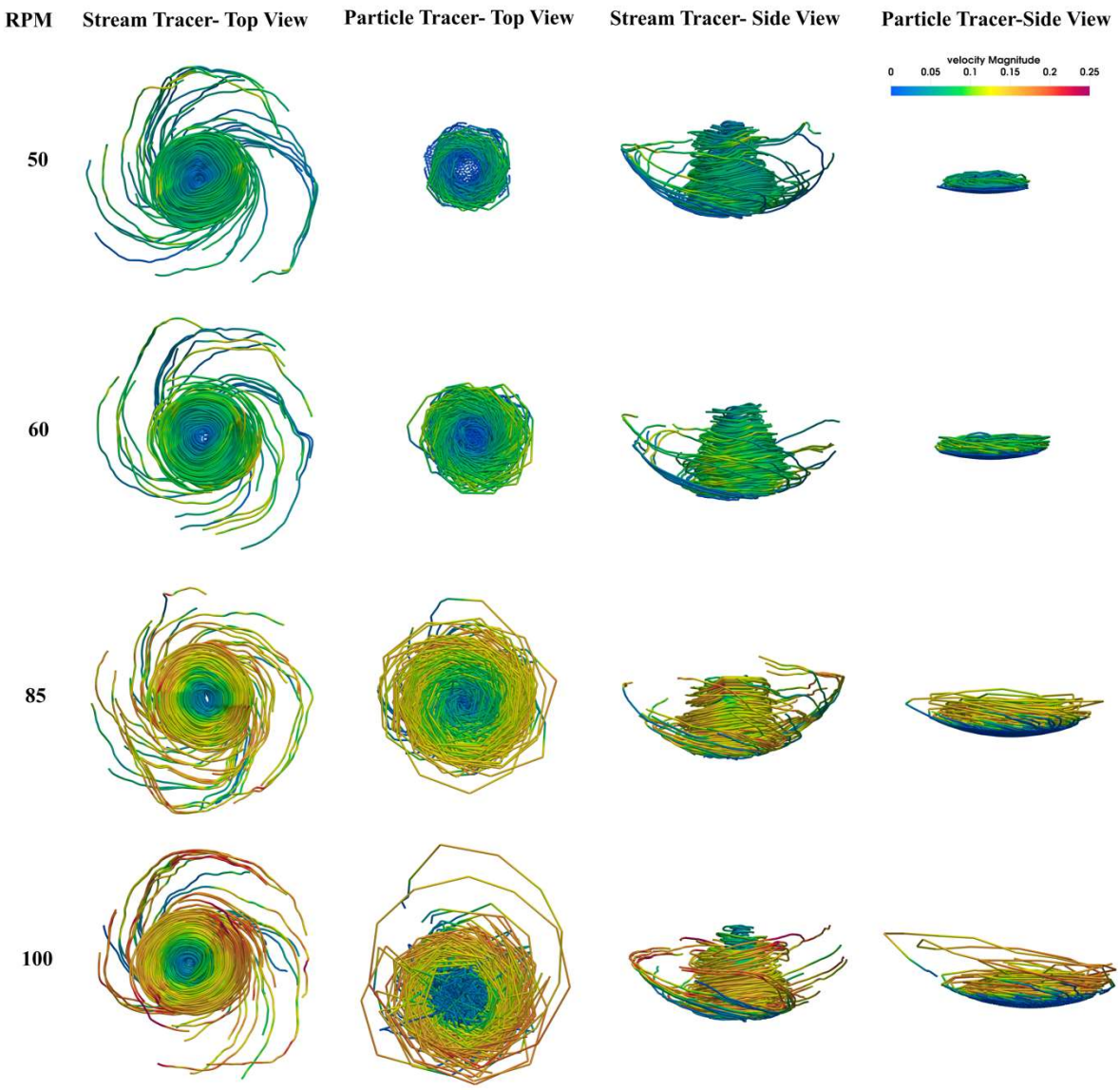

Figure 2.8. Comparison of fluid and particle movement at different RPMs. The stream tracer shows the fluid motion, while the particle tracer shows the particle movement.

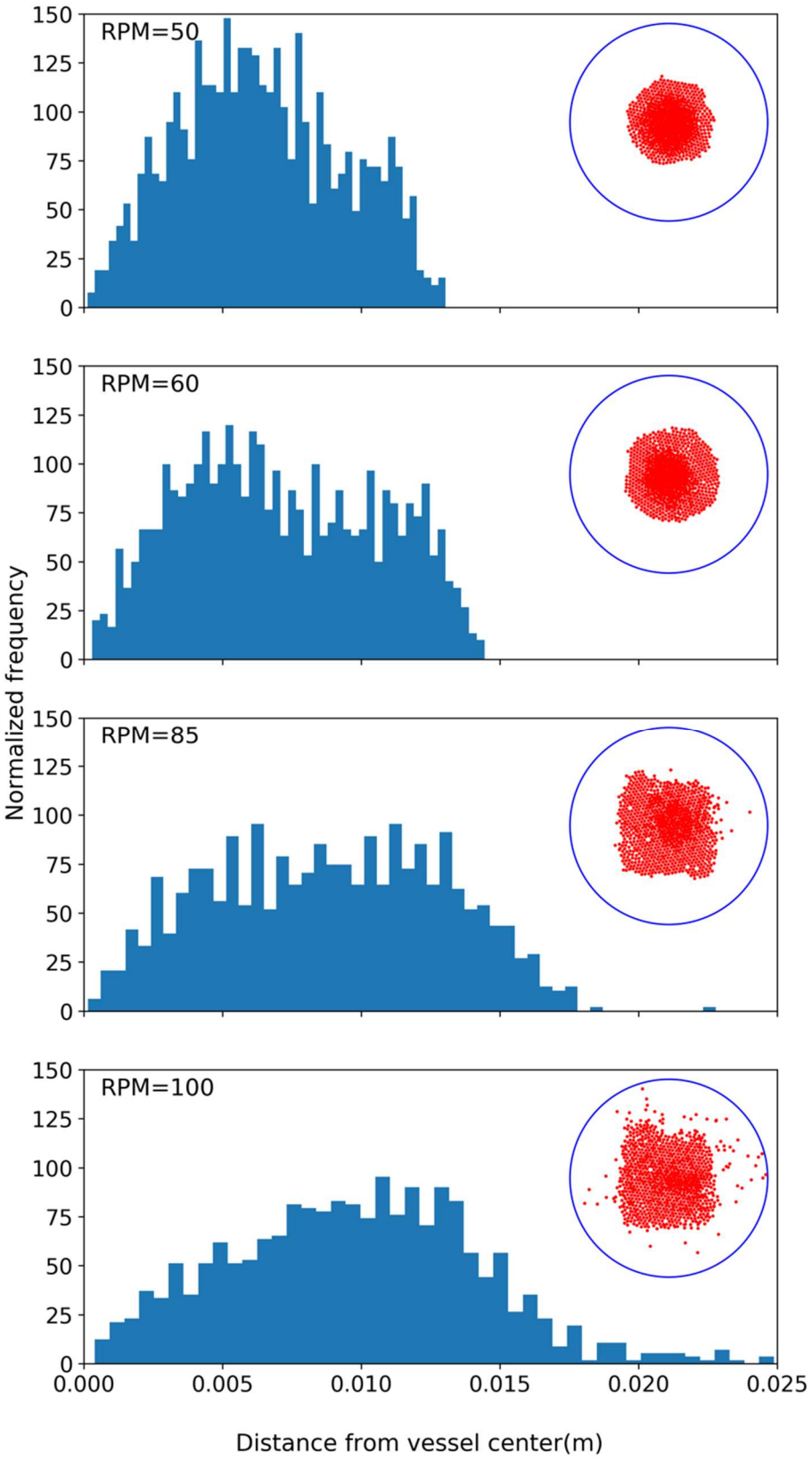

Figure 2.9. Comparison of particle distribution histogram at different rotating speeds

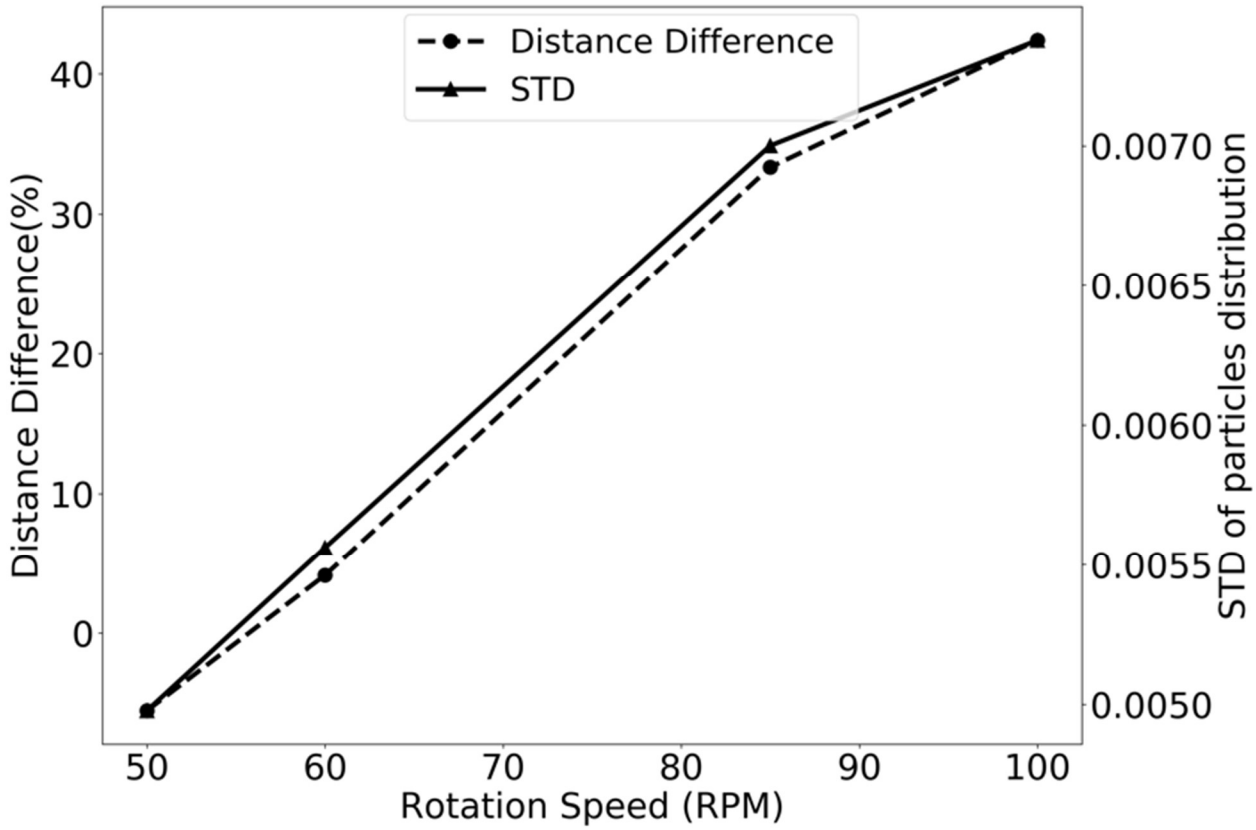

Figure 2.10. Relationship between standard deviation (STD) of particle distribution and rotation speed of USP apparatus II paddle. Change in the distance is evaluated between the initial state and the state 250 seconds after the simulation started.

2.5.3 Model performance

We performed the coupled LBM and DEM on a Linux cluster with multiple nodes and cores. The LBM component of the simulation was the performance-limiting step, while the DEM of particle dynamics was much faster. Figure 2.11 examines and plots the scaling of the LBM computation of fluid dynamics. The speed of the LBM model grew roughly linearly when the number of cores increased to 300. Continuous increase of the core number showed a slower boost in performance, likely due to the communication overhead between the LBM and DEM.

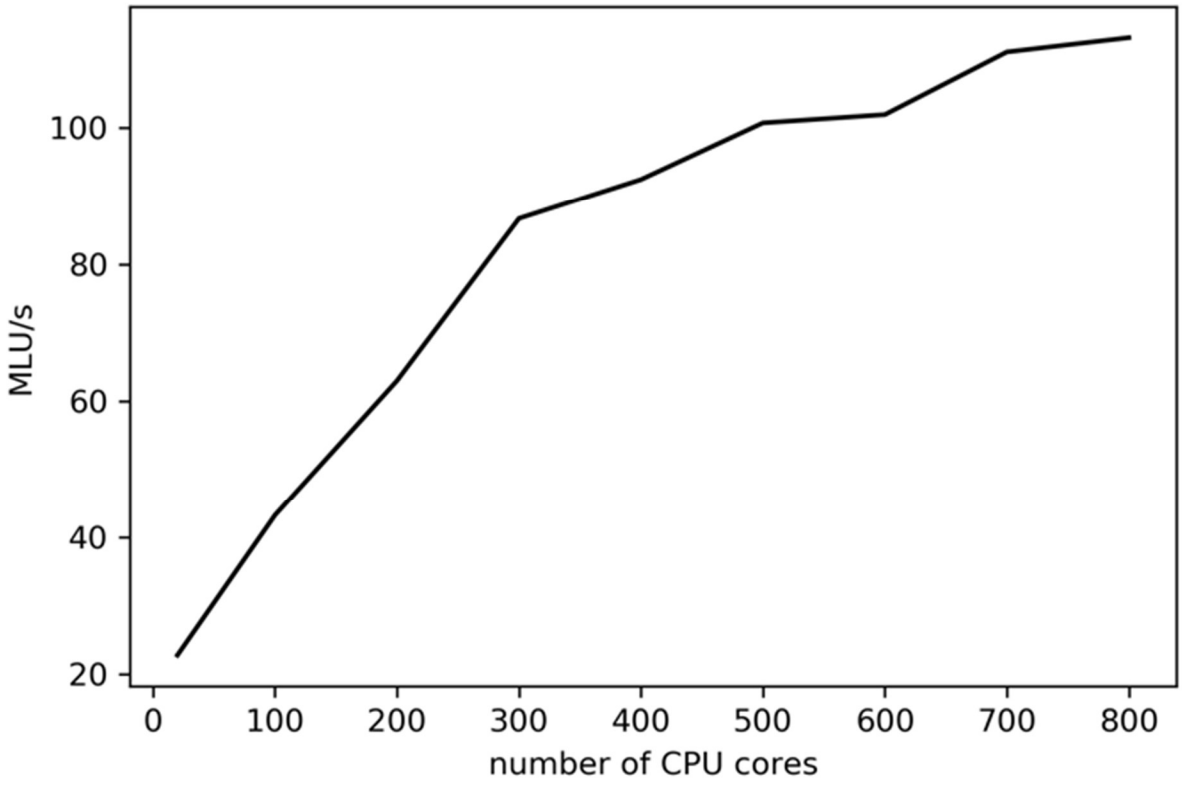

Figure 2.11. Scalability millions of lattice units processed in one second as a function of the number of cores

The simulation conducted in this study demonstrated that coupled LBM and DEM could simulate multiple particles moving in an agitated fluid environment. Simulation results further reproduced experimental results of hydrodynamics in USP Apparatus II, illustrating the suitability and fidelity of LBM in computing fluid dynamics in the scale of a dissolution device used in the pharmaceutical industry. Additionally, we successfully implemented the coupling between LBM and DEM, as demonstrated by the coordinated kinetics between fluid and particle dynamics. This coupling will allow us to further integrate particle dissolution in the computational framework and simulate tablet disintegration and dissolution.

From our implementation of the method, we identified some limitations. The solid particles were simplified as spheres, which may not represent real drugs or excipient particles of various shapes. The immersed moving boundary method works well when a particle is much larger than the lattice size. When a particle is smaller, we used interpolation of lattice velocities to derive the particle's velocity. This process could potentially generate uncertainties of particle dynamics

because of the one-way coupling and ignoring (insignificant) responding forces from moving particles to the fluid.

2.6 Conclusion

Prediction of tablet disintegration and dissolution based on tablet microstructure, formulation, and manufacturing factors is challenging. This study attempted a coupled LBM and DEM simulation approach to compute particle dynamics in USP Apparatus II under various stirring speeds. LBM permitted good scalability and easy implementation of fluid dynamics, while DEM made it possible to calculate individual particle's movement and particle-particle collisions and interactions. The immersed moving boundary scheme was implemented to couple the interactions between solid particles and the fluid phase. Simulation results reproduced experimentally observed fluid dynamics in the USP Apparatus II and illustrate "tight binding" between particle and fluid dynamics. We will implement the dissolution of particles in the next phase of our study.

Acknowledgment: The authors thank Dr. David Sperry from Eli Lilly Co. for the insightful discussion. The financial support from CPPR and Astra Zeneca Co. is also appreciated.

CHAPTER 3. SIMULATION OF PARTICLE DISSOLUTION COUPLED WITH FLUID DYNAMICS IN DISSOLUTION TEST APPARATUS

3.1 Abstract

Computer modeling of the tablet dissolution process can speed up the development of drug formulations. Based on the quality-by-design (QbD) concept, *in-silico* models can assist in quantitatively predicting the effect of different formulation ingredients and processing parameters. By understanding the drug particle dissolution process's underlying mechanisms, we can design the new drug formulation based on *in-silico* simulations. In this paper, we present a new model to simulate the process of drug particle dissolution in USP apparatus II. By coupling the lattice Boltzmann method and discrete element method with the immersed moving boundary method, we developed a model to realize the real-time simulation of drug particle dissolution behavior within USP apparatus II. We first validated our model with a single particle dissolution simulation and compared the results with experimental results. Then we performed a bulk dissolution simulation within USP apparatus II to show our model's scalability. We show our model could be helpful to understand the factors affecting the dissolution process. The real-time simulation of drug particle dissolution shows the power of computer simulation in formulation development, and paves the path toward computer-aided drug formulation development.

3.2 Introduction

Drug particle dissolution within complex fluid dynamics such as USP apparatus II is vital for understanding the kinetics of different pharmaceutical formulations. By understanding the kinetics of drug particle dissolution, we can facilitate designing new formulations. However, until now, we have not had a well-developed computational model to simulate the whole process of drug particle dissolution in USP apparatus II. Here, we propose a new method to simulate drug particle dissolution by coupling the lattice Boltzmann method and discrete element method. Our model can realize the real-time simulation of the tablet dissolution process in USP apparatus II.

3.2.1 Current experimental methods:

The kinetics of single-particle dissolution can be measured with experimental methods such as UV-Vis spectrometry and optical microscopy [111, 112]. The imaging results from the particle morphology measurement are validated against mathematical models or chemical analysis results.

In 2008, Marabi et al. applied the optical microscopy technique to study single-particle dissolution via obtaining the image of single-particle dissolution [111]. These results were validated against the mathematical model of single sphere particle dissolution [111]. In 2014, Svanbäck et al. further developed this method; instead of only comparing it with the theoretical model, they used UV-spectrophotometry to measure the dissolution of particles in solute [112]. They observed a close relationship between the particle morphological results and chemical analytical results.

Measuring bulk particle dissolution kinetics can be performed with UV-Vis spectrometry or conductivity measurements [39, 113]. We can further measure the particle size distribution with laser diffraction analysis as well [114]. By combining these tools, we can obtain a big picture of the bulk particle dissolution behavior.

3.2.2 Mathematical dissolution models

Besides experimental methods, mathematical methods are also developed to predict the dissolution of particles [115]. Two major mathematical models describe particle dissolution. One is a diffusion layer-based model, and the other is a convection–diffusion-based model.

The diffusion layer-based model suggests a thin layer exists on the solid-liquid interface; the concentration of drug particle solute decreases on this thin layer until it is the same as the surrounding environment. Examples of these models are the Noyes–Whiney equation and the Nernst–Brunner equation [101, 116, 117]. These models do not consider the convection of fluid, but they are simple methods to describe the diffusion-controlled release of drug solute. Thus, they are widely used to describe drug particle dissolution behavior. These models can be further developed to consider the impact of other parameters such as particle shape and particle size distributions [118, 119].

To study the impact of hydrodynamics on drug particle dissolution, we must consider the convection of fluid. The convection–diffusion model describes the effect of hydrodynamics on solid particle mass transfer rate. This model could be described as below:

$$\frac{\delta c}{\delta t} = \nabla \cdot (\mathrm{D}\nabla \mathrm{c}) - \nabla \cdot (\mathbf{v}\mathrm{c}) + R \qquad \text{Eq. 3.1}$$

Where c is the drug concentration, t is the time, D is the diffusion coefficient, $\mathbf{v}$ is the velocity and R is the source term. However, this equation could only be barely solved. Different numerical approximations can be employed to solve this model, such as the finite element method (FEM) and finite volume method (FVM). Another approach is to simplify this model by considering simple situations such as static sphere particle dissolution and deriving an analytical solution for this scenario.

Due to the difficulty of describing the fluid dynamics directly, it is usually impossible to derive an exact expression of the solid dissolution in complex hydrodynamics. These complex physical interactions between the fluid and solid particles are generally solved with two parts: computational fluid dynamics (CFD) or the lattice Boltzmann method (LBM) simulation of fluid dynamics and the Noyes–Whitney equation description of the mass transfer between solid particles and fluid. By coupling these two parts, we can show the impact of hydrodynamics on particle dissolution.

Currently, several groups have developed different methods to simulate the drug particle dissolution behaviors. Some of the studies utilize X-ray micro-tomography (XMT) to scan drug particles' micro-structure. Then, the structure is rebuilt numerically. The drug particle simulation results are compared with experimental results and showed good agreement between them [40, 114]. Other studies focused more on single-particle dissolution, such as the dissolution of particles in the laminar flow [120].

3.2.3 CFD study of USP apparatus II

As an *in-silico* method, the CFD method has gained more attention in studying hydrodynamics in USP apparatus [32, 34, 121-124]. The hydrodynamics within USP apparatus II have also been studied with multiple methods. Baxter et al. applied the particle image velocimetry (PIV) method to visualize the particle distribution and compared it with CFD simulation results [26, 30]. Bai et al. used the laser‐Doppler velocimetry (LDV) technology to measure the velocity distribution and applied the CFD simulation using the software Fluent [27, 29]. Their study discovered the dramatic change of strain rate at the bottom of USP apparatus II, emphasizing the importance of tablet location during the USP apparatus II test. Bai et al. also performed an early stage of simulation to study the blending time of USP apparatus II with CFD and combined CFD with Noyes–Whitney equation to simulate tablet dissolution [27, 29, 32-34]. The dissolution coefficient is predicted with CFD, and the mass transfer from tablet to fluid is calculated with the Noyes–Whitney equation. However, in their method, the expected dissolution coefficient needs to be scaled to match the actual dissolution constant. This is because their model that was used to predict dissolution constant is not accurate enough.

3.2.4 Our model advantage over revious ones:

Even though a lot of effort has been put into the study of drug particle dissolution under the hydrodynamic influence, we need to solve many problems before we can get a complete computational model for drug particle dissolution simulation. For example, Cao et al. combine COMSOL with DigiDiss (an in-house direct simulation code of drug particles)[39, 40]. The fluid dynamics from the COMSOL simulation were then imported into DigiDiss. This means the coupling is only one-way, and the particle's impact on hydrodynamics could not be simulated in

their model [40]. Also, importing COMSOL simulation results to DigiDiss means the simulation could not be done in real-time. These limitations reduced the feasibility of this model. Here in our model, a directly coupled fluid and particle dissolution model is built. We could simulate the hydrodynamic from fluids to particles and vice versa. Also, the coupling between the velocity field and concentration field is done in real-time. We do not need to import the velocity field from another software. We compare our model with previous experiments to verify the dissolution behavior of particles in hydrodynamic conditions in different hydrodynamic conditions.

3.3 Methodology

3.3.1 Lattice Boltzmann Method (LBM)

In our simulation, the lattice Boltzmann method is coupled with the discrete element method to study the interaction between particles and fluid.

The convection-diffusion equation in Eq. 3.1 can be solved with the lattice Boltzmann method by implementing two lattice equations as shown in Eq. 3.2 and Eq. 3.7 [125-127]. The function f (**x**,t) governs the hydrodynamic conditions while the function *g(**x**,t)* governs the concentration distribution. The probability of finding a particle at location x at time t is equal to *f (**x**,t)* and *g(**x**,t)*. By passing the velocity field in *f* to *g*, we can simulate the impact of hydrodynamic conditions on mass concentration distribution.

$$f_\alpha(\boldsymbol{x} + e_\alpha \delta t, t + \delta t) - f_\alpha(\boldsymbol{x}, t) = -\frac{1}{\tau}[f_\alpha(\boldsymbol{x}, t) - f^{eq}(\boldsymbol{x}, t)] \qquad \text{Eq. 3.2}$$

The viscosity of fluid v is related to the dimensionless relaxation time τ as shown in Eq. 3.3, where c_s is the lattice sound speed.

$$v = \mathrm{c_s^2}\left(\tau - \frac{1}{2}\right)\delta t \qquad \text{Eq. 3.3}$$

The local equilibrium distribution function $f^{eq}(\boldsymbol{x}, t)$ could be expressed as below:

$$f^{eq} = \rho \mathrm{w}_\alpha \left[1 + \frac{1}{2}\frac{\boldsymbol{u}\cdot\boldsymbol{c_\alpha}}{c_s^2} + \left(\frac{\boldsymbol{u}\cdot\boldsymbol{c_\alpha}}{c_s^2}\right)^2 - \frac{u^2}{2c_s^2}\right] \qquad \text{Eq. 3.4}$$

Where the fluid density ρ and velocity $\boldsymbol{u}$ could be calculated as below:

$$\rho = \sum_{\alpha=0}^{q} f_\alpha \quad , \rho \boldsymbol{u} = \sum_{\alpha=0}^{q} f_\alpha \boldsymbol{c_\alpha} \qquad \text{Eq. 3.5}$$

We can represent the right side of Eq. 3.2 as Ω:

$$\Omega = -\frac{1}{\tau}[f_\alpha(\boldsymbol{x}, t) - f^{eq}(\boldsymbol{x}, t)] \qquad \text{Eq. 3.6}$$

The LBM equation for concentration distribution is :

$$g_\alpha(\boldsymbol{x} + e_\alpha \delta t, t + \delta t) - g_\alpha(\boldsymbol{x}, t) = -\frac{1}{\tau'}[g_\alpha(\boldsymbol{x}, t) - g^{eq}(\boldsymbol{x}, t)] \qquad \text{Eq. 3.7}$$

Similarly, the local equilibrium distribution function $g^{eq}(\boldsymbol{x}, t)$ could be expressed as below:

$$g^{eq} = \mathrm{Cw}_\alpha \left[1 + \frac{1}{2}\frac{\boldsymbol{u} \cdot \boldsymbol{c_\alpha}}{c_s^2} + \left(\frac{\boldsymbol{u} \cdot \boldsymbol{c_\alpha}}{c_s^2}\right)^2 - \frac{u^2}{2c_s^2}\right] \qquad \text{Eq. 3.8}$$

The concentration or density of drug *C* could be described as:

$$C = \sum_{\alpha=0}^{q} g_\alpha \qquad \text{Eq. 3.9}$$

The diffusion coefficient *D* could be described as:

$$D = \mathrm{c_s^2}\left(\tau' - \frac{1}{2}\right)\delta t \qquad \text{Eq. 3.10}$$

For the D3Q19 and D3Q7 models, the discrete velocity vectors $\boldsymbol{e_\alpha}$ and weighting factors w_α on each direction could be shown as in Eq. 3.11 and Eq. 3.12 respectively. Here in our method, the D3Q19 model is used for velocity simulation, and the D3Q7 model is used for concentration simulation [72, 73].

$$\{e_\alpha, w_\alpha\} = \begin{cases} c[(0,0,0)], \frac{1}{3} & \alpha = 0 \\ c[(\pm 1,0,0), (0,\pm 1,0), (0,0,\pm 1)], \frac{1}{18} & \alpha = 1,2,3,\ldots,6 \\ c[(\pm 1,\pm 1,0), (\pm 1,0,\pm 1), (0,\pm 1,\pm 1)], \frac{1}{36} & \alpha = 7,8,9,\ldots,18 \end{cases} \qquad \text{Eq. 3.11}$$

$$\{e_\alpha, w_\alpha\} = \begin{cases} c[(0,0,0)], \frac{1}{4} & \alpha = 0 \\ c[(\pm 1,0,0),(0,\pm 1,0),(0,0,\pm 1)], \frac{1}{8} & \alpha = 1,2,3,\dots,6. \end{cases} \quad \text{Eq. 3.12}$$

To simulate the situation where a solid particle dissolves into fluid, we use a source term C_w to describe the change of drug concentration due to particle dissolution.

$$g_\alpha(\boldsymbol{x} + e_\alpha \delta t, t + \delta t) = g_\alpha^+(\boldsymbol{x}, t) + 2w_\alpha C_w \quad \text{Eq. 3.13}$$

We implement the immersed moving boundary method to simulate the hydrodynamic interaction between the fluid and solid particles [15]. This is done by replacing the right side of Eq. 3.2 with another form:

$$\Omega = \frac{1}{\tau}(1 - B)(f^{eq} - f) + B\Omega^S \quad \text{Eq. 3.14}$$

$$B = \frac{\varepsilon(\tau - 0.5)}{(1 - \varepsilon) + (\tau - 0.5)} \quad \text{Eq. 3.15}$$

Where ε is the ratio of the solid particle in the current lattice node.

$$\Omega^S = f_-(\boldsymbol{x}, t) - f(\boldsymbol{x}, t) + f^{eq}(\rho, \boldsymbol{U_s}) - f_-^{eq}(\rho, \boldsymbol{u}) \quad \text{Eq. 3.16}$$

In Eq. 3.16, the term $\boldsymbol{U}_S$ represents the velocity of the solid node.Further, $f_-(\boldsymbol{x}, t)$ is the bounce back form of $f(\boldsymbol{x}, t)$.

3.3.2 Discrete Element Method (DEM):

We model tablet particles as solid particles in DEM. Each particle is explicitly modeled and treated as the fundamental unit. A particle (e.g., API) may dissolve in liquid, resulting in its particle size decreasing and molecules being released to the environment. A particle (e.g., excipient) may take up water from the liquid environment, swell, and exert forces on neighboring particles (in the tablet). To model the drug and excipient particles in a tablet, we must consider the interaction or bonding force between two particles.

As two solid particles approach each other, there is an attractive force due to the *van der Waals* interaction (and possible electrostatic interaction as well, if the particles bear surface

charges). As they continue to get closer, especially during the tablet compression stage, the particles undergo deformation, firstly the recoverable, elastic, and then (partially) plastic deformation. Such deformation requires energy, thus indicating the repulsive nature when a particle is compressed. As shown in Figure 3.1, the figure conveys an overlapping δ between two particles and is assumed to represent the elastic deformation suggesting recovery of the particle, which can be described by Hook's law. A few models have described interparticle interactions for the DEM simulation. One such model is Edinburgh Elasto-Plastic Adhesion (EEPA) Model, proposed by Thakur, et al. in 2014 [128]. As shown in Figure 3.2, the two figures model the loading, unloading, reloading, and adhesive phases of particle-particle interactions. The loading stiffness parameter k1 governs the loading process, once unloaded or reloaded, the contact force will follow the unload/reloading stiffness parameter k_2. If the unloading process continues, the contact force will switch to negative, which becomes an adhesive force until it reaches the maximum $-k_{adh}\delta^n_{min}+f_0$. If the unloading continues, the adhesive force will reduce until it comes to the constant adhesive strength f_0.

s

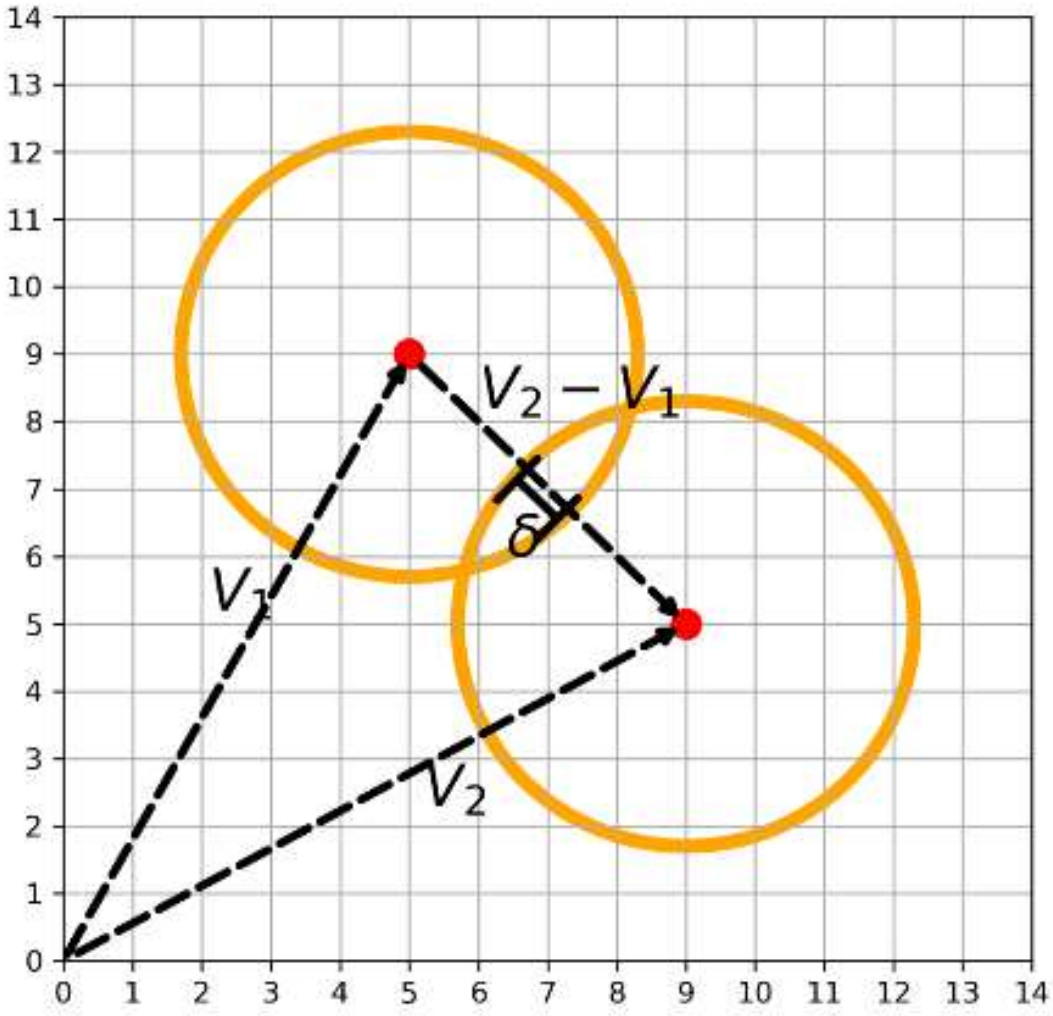

Figure 3.1. DEM particle overlap, δ shows the overlap between to DEM particles.s

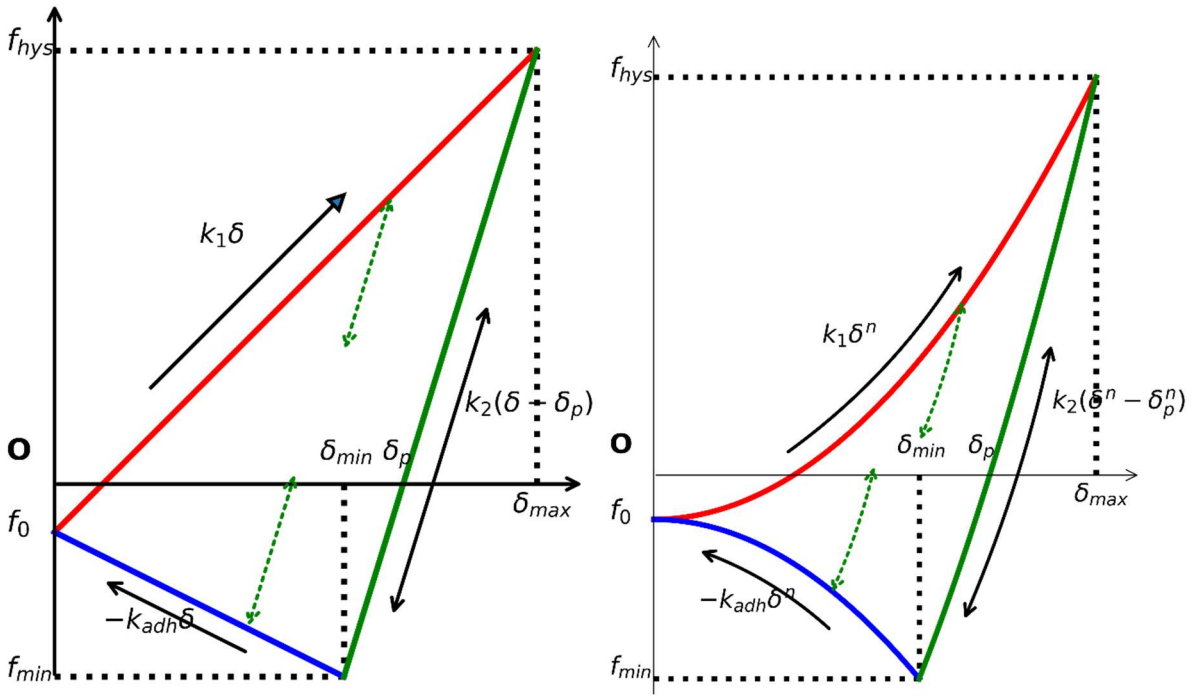

Figure 3.2. Normal contact force-displacement function (left: linear model, rights: nonlinear model)

The total contact normal force $\boldsymbol{f_n}$ includes two parts: hysteretic spring force f_{hys} and normal damping force f_{nd}, with $\boldsymbol{u}$ as a unit normal vector pointing from contacting point to particle center.

$$\boldsymbol{f_n} = (f_{hys} + f_{nd})\boldsymbol{u} \qquad \text{Eq. 3.17}$$

$$f_{hys} = \begin{cases} f_0 + k_1\delta^n \\ f_0 + k_2(\delta^n - \delta_p^n) \\ f_0 - k_{adh}\delta^n \end{cases} \qquad \begin{matrix} k_1\delta^n < k_2(\delta^n - \delta_p^n) \\ k_{adh}\delta^n < k_2(\delta^n - \delta_p^n) < k_1\delta^n \\ k_2(\delta^n - \delta_p^n) < k_{adh}\delta^n \end{matrix} \qquad \text{Eq. 3.18}$$

$$f_{nd} = \beta_n v_n \qquad \text{Eq. 3.19}$$

Where v_n is the magnitude of the relative normal velocity, and β_n is the normal dashpot coefficient.

In a similar approach of using DEM to simulate the tableting process, when particles are pushed against each other, the same elastic repulsion model is used reciprocally to describe their attraction when pulled apart [96].

In the EEPA model, the adhesive force is considered the combination of several different forces such as *van der Waals* forces, sintering and chemical bonding, electrostatic forces, mechanical forces, and so on.

In our model, we use a simple EEPA model to simulate the interaction force between particles. Because the relative movement between particles is small, the damping for f_{nd} is neglected in our model.

3.3.3 DEM particle mass transfer to LBM fluid

On the LBM side, we use the source term C_w as the mass flux in Eq. 3.13 to simulate the mass transfer from the solid DEM particle to the LBM simulated fluid field.

On the DEM particle side, the drug dissolved from solid particles is simulated with the Noyes-Whitney equation as shown below[101]. Where A is the surface of solid particles on solid/liquid interface (m^2), K is the dissolution constant (m/s), C is the current concentration, C_s is the saturated concentration (kg/m^3), W is the weight of the particle (kg) and t is time (s).

$$\frac{dW}{dt} = -\mathrm{KA}(\mathrm{C_s} - \mathrm{C}) \qquad \text{Eq. 3.20}$$

Thus, in our simulation, the dissolution process and convection-diffusion process are considered two steps, one after the other.

Therefore, for each timestep, on the unit lattice cell covered with the DEM particle, the source term could be expressed as below, where δt is the physical timestep and δx is the unit physical length of each lattice node.

$$C_w = -\frac{\delta t}{\delta x}\mathrm{K}(\mathrm{C_s} - \mathrm{C}) \qquad \text{Eq. 3.21}$$

This equation connects the DEM particle with the LBM fluid mass transfer.

To update the radius of the particle, we calculate the mass transfer from the particle's surface to the fluid. The equation is described as below.

$$\frac{d}{dt}\left(\rho_s \frac{4\pi}{3}\left(r^i\right)^3\right) = -\int_{A^i} \xi dA \qquad \text{Eq. 3.22}$$

Of which, the ξ is the mass flux (mass dissolved in per unit time at per unit lattice cell), ρ_s is the density of particle, and r_i is the radius of *ith* particle in DEM model.

Due to the mass transfer from particles to fluid, the radius of particles will be updated based on the radius update Eq. 3.22.

Currently in our model, as the particle dissolves and the radius reduces to be smaller than the lattice unit, we still use the immersed moving boundary method to handle the solid-fluid interaction. This might cause a larger error when calculating the interaction force. Further improvement could be implemented to recalibrate the interpolation function Eq. 3.15.

3.4 Simulation setup

3.4.1 Single particle dissolution:

To validate our model, we simulate the single-particle dissolution process under complex hydrodynamics. A stirring model is set up and results are compared with previous experimental results[40]. A sodium carbonate sphere particle with a diameter of 1mm is placed 2.4mm above the magnetic stirrer. The space of simulation is 12mm × 12 mm × 8 mm. The setup is shown in Figure 3.3. The sodium carbonate particle has a solubility of 30.7 g/100 g in the water at 25 °C [129]. The diffusion coefficient D is 1.12×10^{-9} m^2/s and the dissolution constant K is set as1.0×10^{-5}m/s [39].

Different from the previous simulation, where the velocity field is simulated with external software COMSOL Multiphysics, in our simulation, the velocity field was directly simulated with lattice Boltzmann method with *palabos* [40, 60]. The real-time velocity field is coupled with the DEM particles simulated with LIGGGHTS [83]. The coupling between LBM and DEM is handled with the immersed moving boundary method in LBDEMcoupling [15, 16].

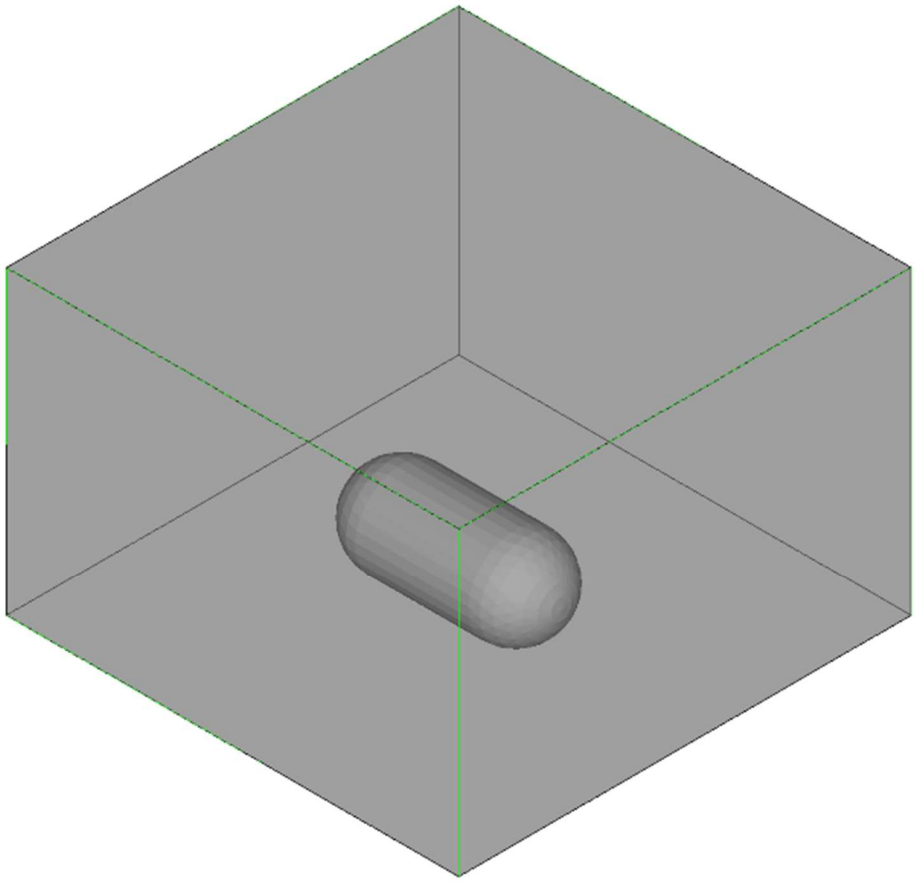

Figure 3.3. The geometry of the stirrer setup. One stirrer is placed in a cube of 12mm ×12mm × 8mm.

3.4.2 Bulk particle dissolution in USP apparatus II

To investigate the the hydrodynamic condition's impact on particle dissolution, different paddle rotation speeds and other conditions were investigated in previous studies [26, 28, 31, 130]. In our model, we demo the ability of our model by simulatingsimulate different scenarios, such as different USP apparatus II paddle rotation speed and particle dissolution constant K, to demonstrate our model's ability. These experiments show our model's the accuracy and flexibility of our model.

Table 3.1. Parameters used for USP apparatus II simulation.

Temperature (T)	37 °C
Fluid Density (ρ_f)	993.3 kg/m³
Water Kinetic Viscosity(v_k)	6.97e-7 m²/s
Diffusion Coefficient (D)	1.12e-9 m²/s
Dissolution constant (K_0)	1.0e-5 m/s
Water Volume (V)	850 mL
Particle radius (R)	500 μm, 1500 μm
Particle density (ρ_p)	2540 kg/m^3
Number of particles (N)	100~2000
Young's modulus (Y)	6.13e6 Pa
Poisson's ratio (v)	0.225
Coefficient of restitution (e)	0.8
Coefficient of static friction (μ_s)	0.2
Coefficient of rolling friction (μ_r)	0.020
Loading stiffness (k_1)	1.e5
Unloading stiffness (k_2)	4.e6
Adhesion stiffness (k_{adh})	5.e4
Adhesion Exponent (n *for* k_{adh})	10
Overlap Exponent (n *for* k_1 *and* k_2)	1.5
Timestep (dt)	6.67e-5(s)
Grid size of the model	306×306×363

As shown in Figure 3.7, a 3D USP apparatus II is modeled with the lattice Boltzmann method, the dimension is based on the parameters in USP general chapter 711 [12]. For the dissolution particles, we use sodium carbonate as an example. As shown in Figure 3.8, around 2000 particles with a radius of 500 μm are compressed into a tablet. These particles are first filled into a punching mold. Then a cylinder punch die is used to press these particles to make them a cylinder shape tablet. The average overlap between particles is 10% of the radius. This DEM-modelled tablet is placed at the bottom center of USP apparatus II. The parameters used in the model are listed in Table 3.1. We adopted most parameters from sodium carbonate, but for the compression model, the parameters are based on our simulations.

3.5 Results and discussion

3.5.1 Single particle dissolution

A magnetic stirrer bar is placed at the bottom of the beaker and shows the side and top views of the velocity field. Our simulation results show a good match with previous simulations.

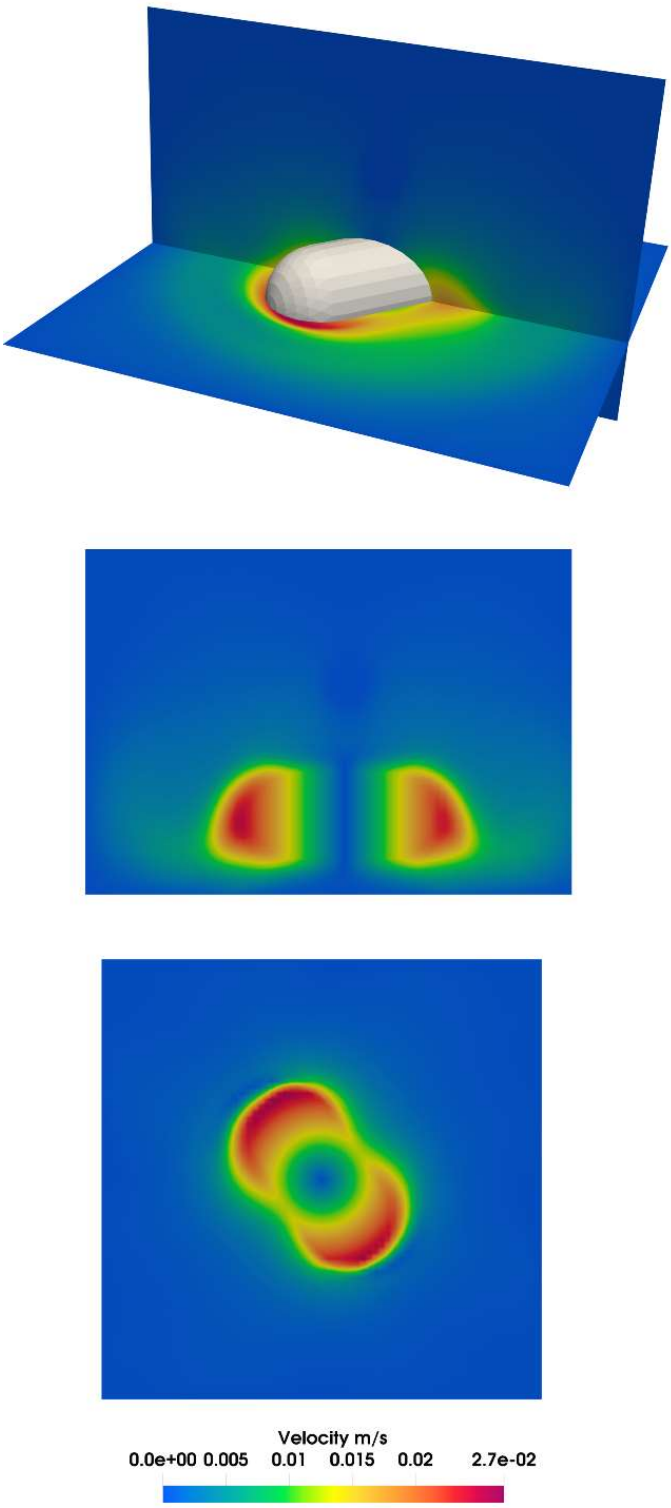

Figure 3.4. Overview (top), Side view (middle), and top view (bottom) of lattice Boltzmann simulation of stirring bar induced velocity field.

The mass transfer between solid-state particles and fluid will increase the sodium carbonate concentration in water. The concentration distribution of sodium carbonate's concentration distribution at different particle release fractions is shown in Figure 3.5. Please note that because we use the uniform color bar for all three distributions, we note that the difference in concentration distribution is as big as shown in the previous simulation in Hui's paper [40].

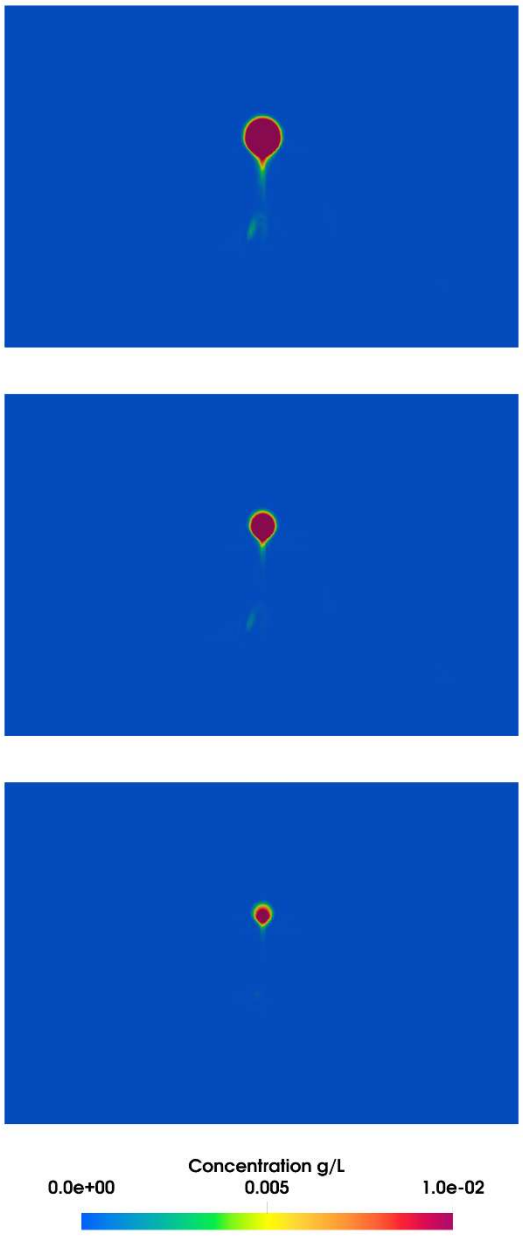

Figure 3.5. Particle dissolution process. Different release fraction 0%, 50%, 90%.

The particle release fraction over time is plotted and compared with experimental results [40]. As shown in Figure 3.6, our results show a good match with previous experimental results. This result means that our model could accurately simulate the complex hydrodynamics and model the dissolution of a single particle. For the next step, we will apply this model to bulk particle dissolution in USP apparatus II.

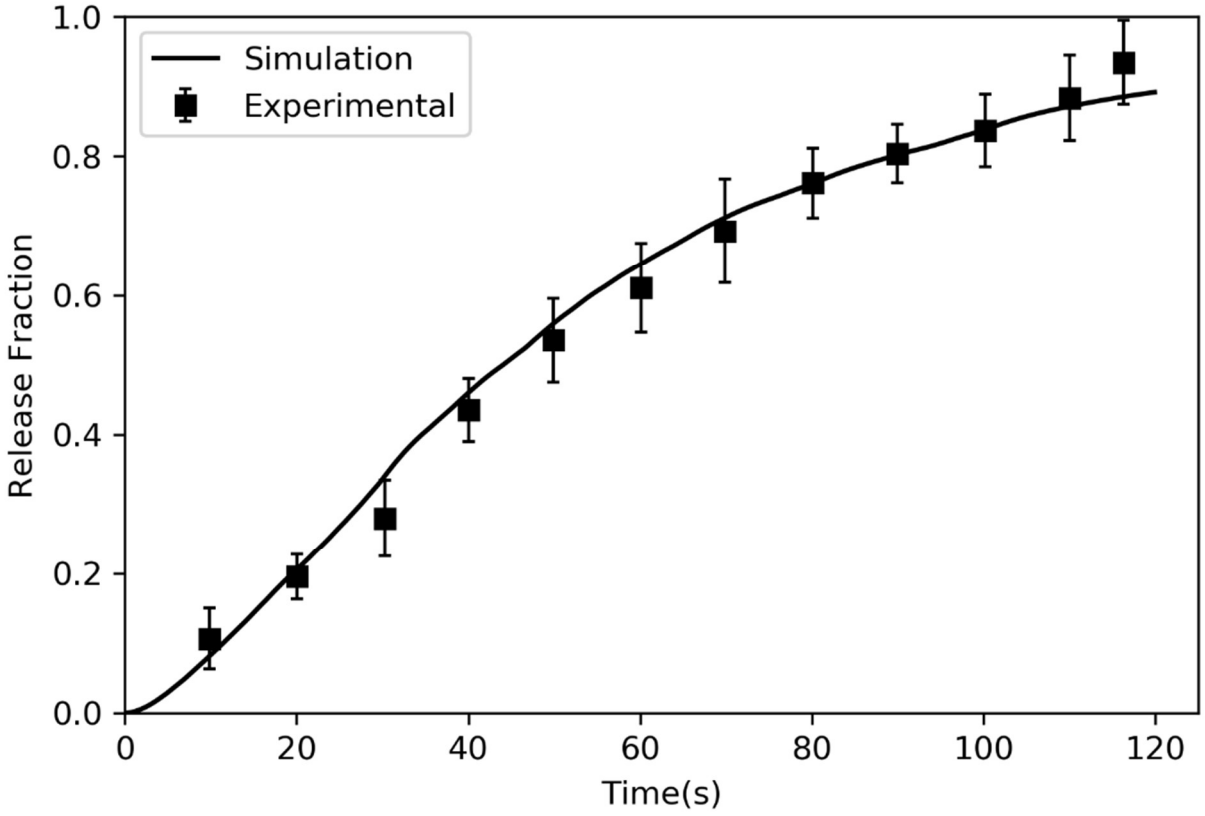

Figure 3.6. Particle release fraction over time. The simulation result (solid line) shows a good match with the experimental result (dot with error bar).

3.5.2 Bulk particle dissolution in USP apparatus II

Figure 3.7 shows the velocity field and concentration field, respectively. A close look at the particles is shown in Figure 3.8. As we can observe in Figure 3.7 that, there is a highly concentrated area under the paddle at the bottom of USP apparatus II. We can see in Figure 3.8, the particles located at the surface dissolved faster than those located in the middle. Also, the particles located on the side of the bulk dissolve faster than those located at the top of the particle bulk. For our model, when the local radius exceeds saturated concentration, the particle will

recrystallize. Thus, the particle's radius could be larger than the original radius.

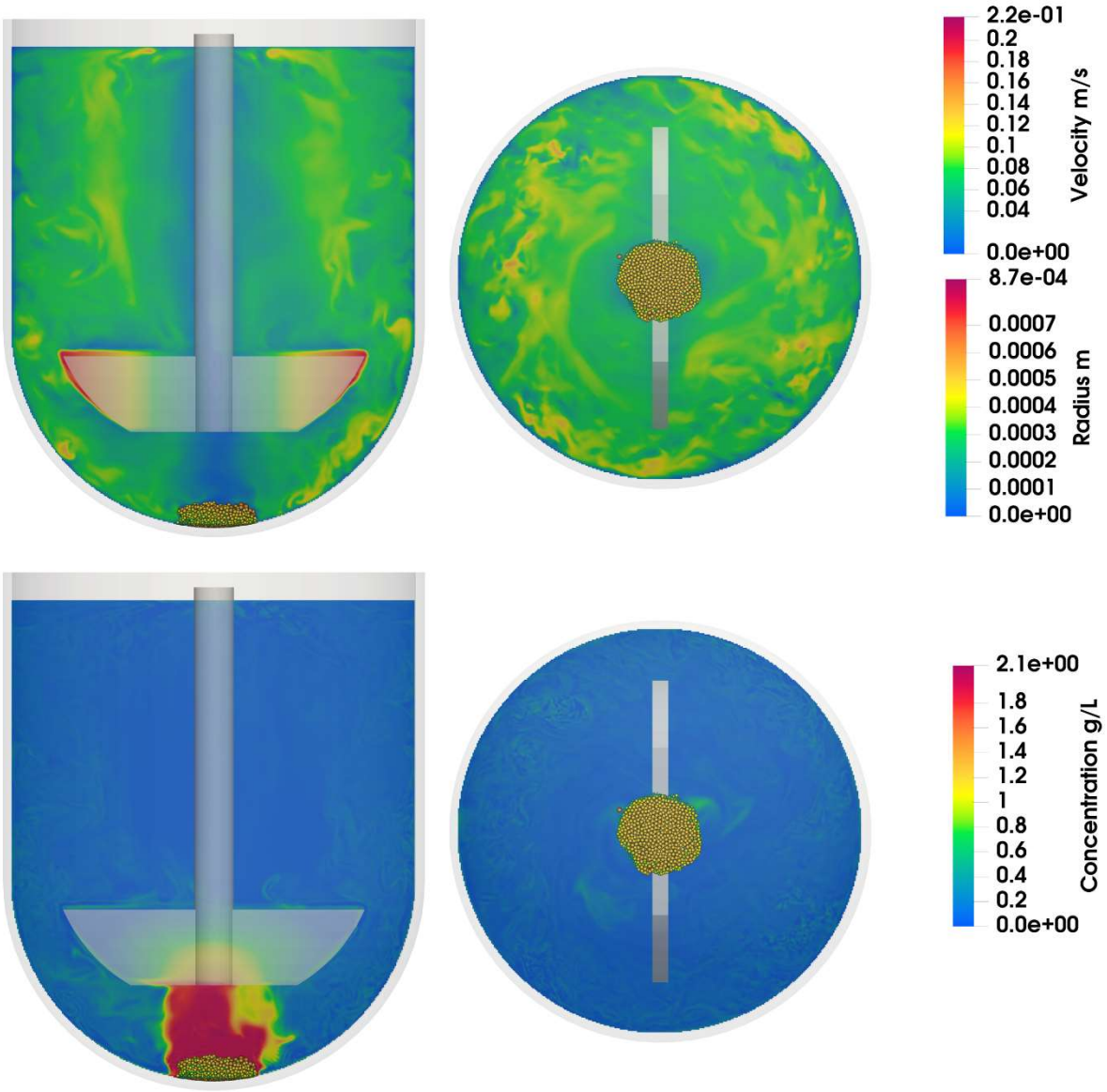

Figure 3.7. Side view and top view of the simulation scheme at the time of 20s. First row: velocity distribution. Second row: concentration distribution. The tablet particles are placed at the bottom of USP apparatus II. The density of the drug dissolved from the particles is shown in the figure.

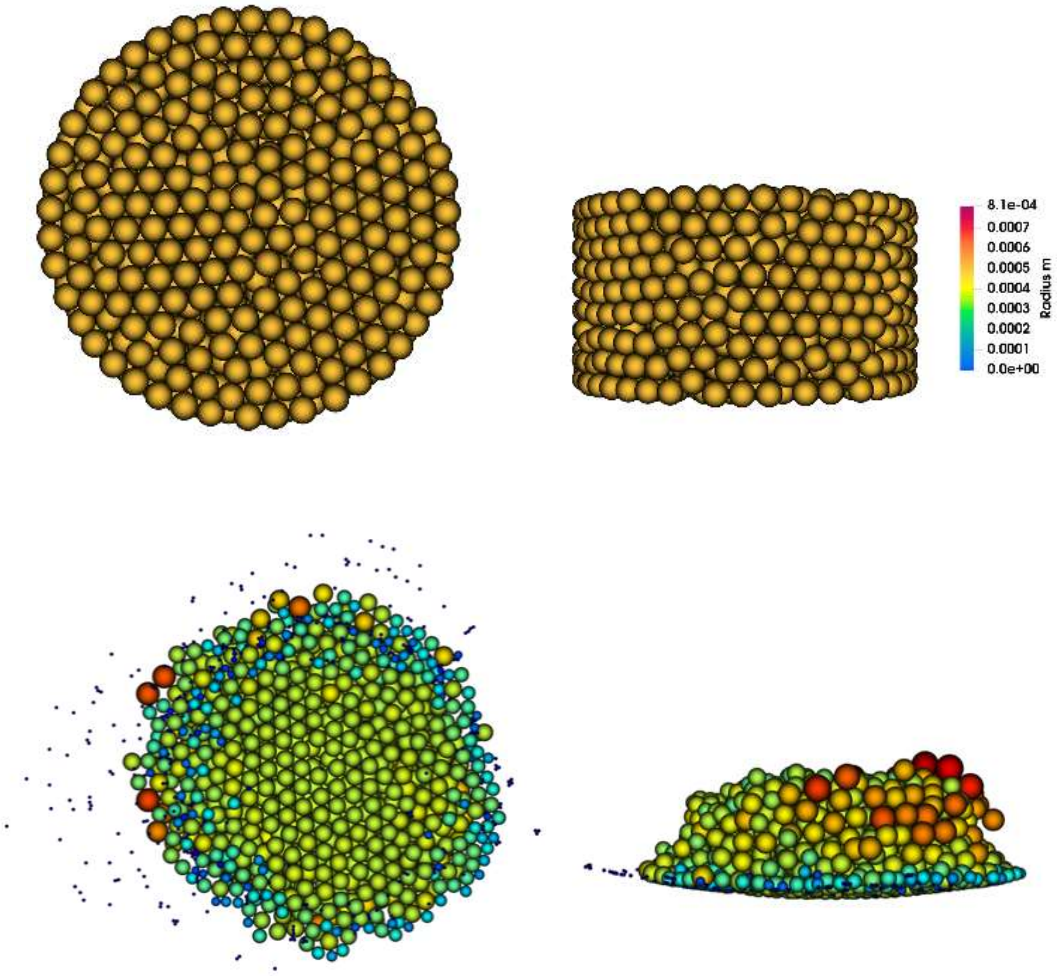

Figure 3.8. Visualization of particles. Top two: tablet particles before dissolution test. Bottom two: particles after dissolution test for the 20 s. The color indicates the particle's radius. We can see that the particles on the surface will dissolve first.

3.5.3 Dissolution detail

Different from previous studies, we can directly visualize the drug particle dissolution process in our model. Thus, we can efficiently study the drugs' distribution within the fluid. With our new scheme, we can directly observe the drug's distribution in USP apparatus II. We notice that the drug is focused near the paddle. The drug's concentration moves up to the paddle. We can observe there is one highly concentrated region at the bottom of USP apparatus II. In Figure 3.9, we can see the drug concentration develop. By visualizing the drug concentration's movement over time, we notice that the drug is first concentrated under the paddle in USP apparatus II. Then,

the paddle movement distributes the drug concentration, which was to the outer side of USP apparatus II. We notice the drug concentration on the outer side area of USP apparatus II is higher than the inner side area of USP apparatus II. This pattern could indicate the drug concentration's movement direction. This drug concentration gradient could suggest that we should be careful when sampling from USP apparatus II.

Because the drug concentration distribution is not uniform within the USP apparatus II, we compare the concentration over time plot at four different sampling spots as indicated in Figure 3.10. We notice the bottom spot concentration increases fast, and because of the complex hydrodynamics at that region, the concentration value variation is most significant at the bottom spot. Also, we notice the sampling spot closer to the rotating paddle has a higher concentration variation. Further, compared to the orange middle sampling spot, the red sampling spot at the middle of USP apparatus II has lower value variation. The concentration is lower than the orange middle spot at the beginning. However, the three sampling spots above the paddle will converge to the same constant value after 200 s.

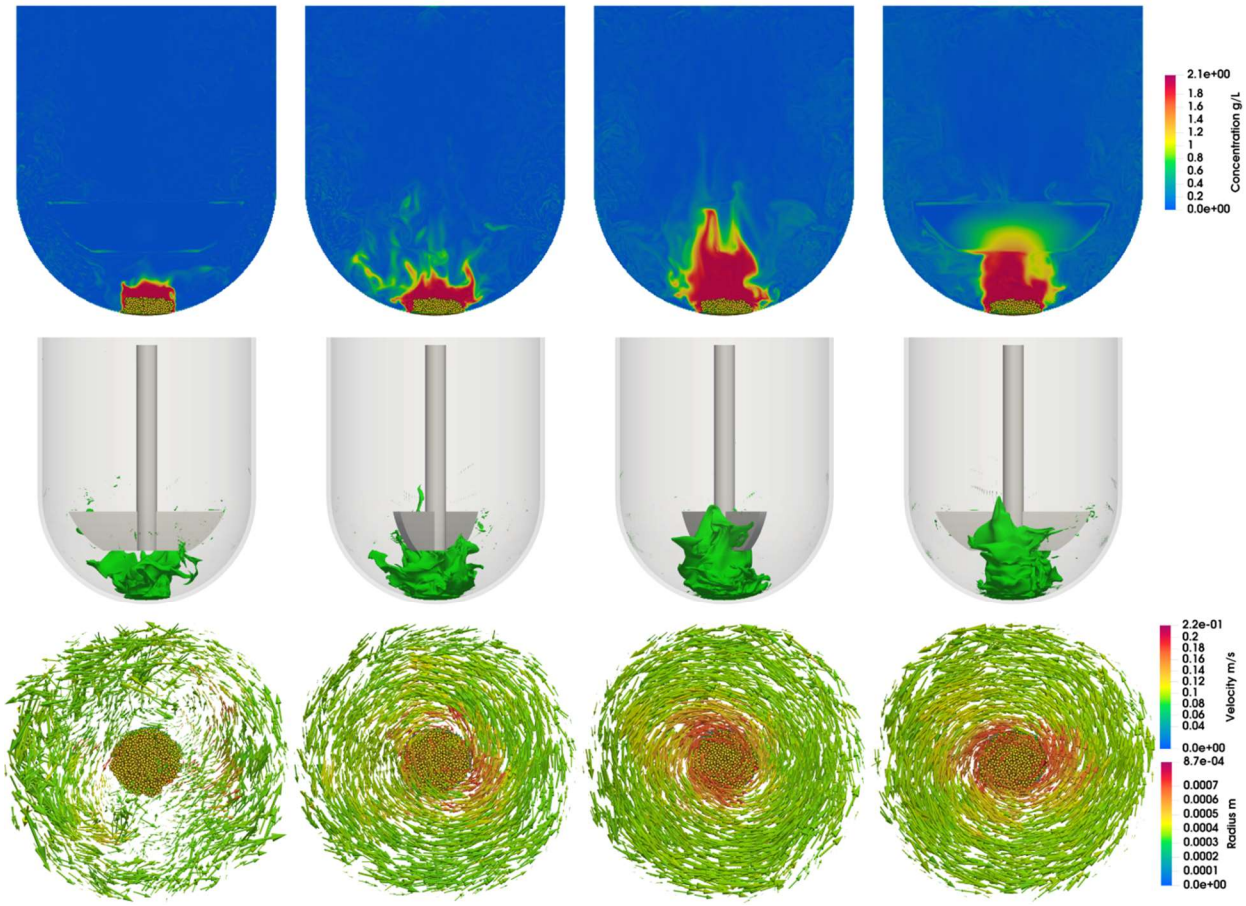

Figure 3.9. Visualization. For each row, from right to left, represent the 5s, 10s, 15s, and 20s time spots. The first row shows the change of drug concentration distribution overtime. The second row shows the contour of 1g/L concentration and the relative position with the paddle. The third row shows the vector of the velocity field.

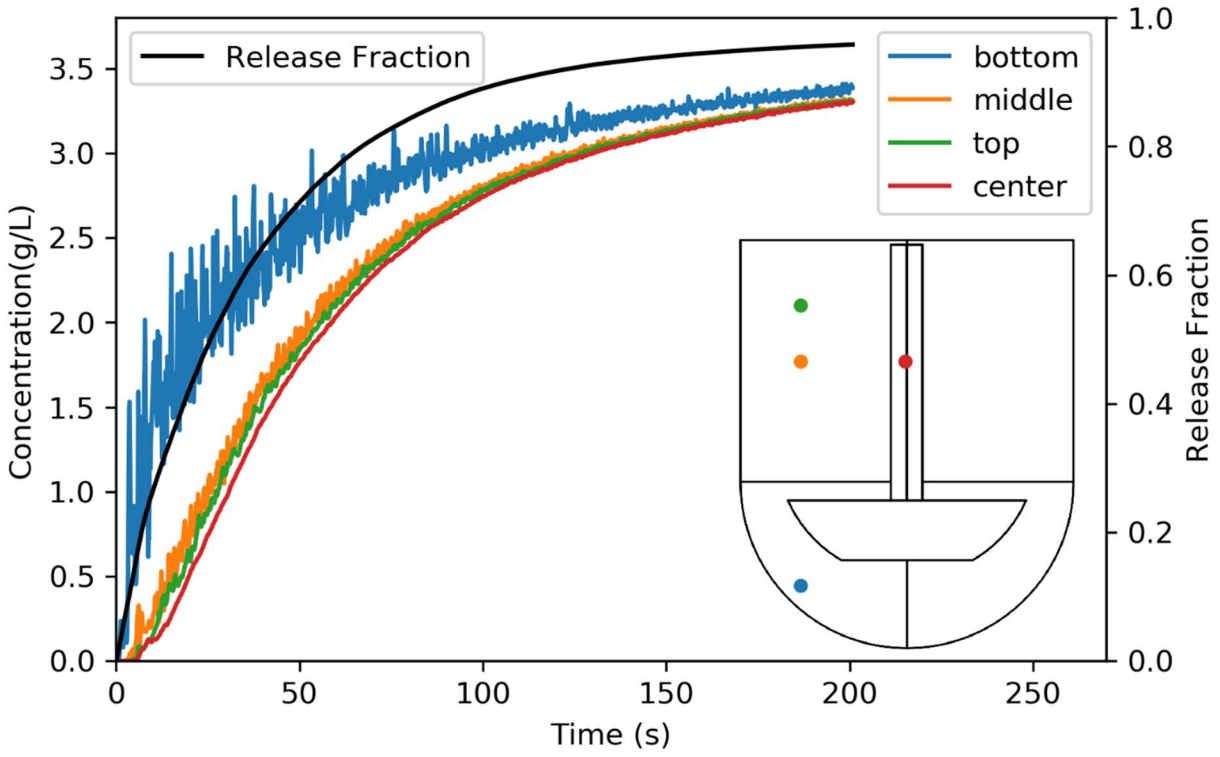

Figure 3.10. Concentration change over time at different sampling positions in USP apparatus II. The sampling position is shown in the lower right figure. The color of the sampling position is the same as the plot. The USP general chapter 711 suggests the sampling zone should be halfway between the dissolution medium surface and the top of the rotating paddle and should not be less than 1cm from the wall of the USP apparatus II vessel [12]. This is represented by the orange dot in the figure.

3.5.4 Contour:

In Figure 3.11, we visualize the velocity of fluid near the particles with vectors, and can observe the fluid's movement pattern in USP apparatus II. There is a tangent flow near the particles. This observation explains why the particles located on the side of the particle bulk dissolve faster. Higher velocity induced higher convection. Also, we can observe that as the rotation speed increases, the velocity near the tablet will increase as well, which further increases the dissolution speed. At RPM=85, we observe that the particles are distributed wider than those at lower RPMs. These observations indicate that a higher rotation speed will increase the dissolution speed, not only because the higher fluid velocity induced more elevated convection, but also because higher velocity will reduce the particles' coning effect. Because higher fluid velocity will drive the particle to spread wider at the bottom of the apparatus, the particles have more area contacting the

fluid and thus dissolve. The increased dissolution area and convection rate explain why higher rotation speed leads to higher dissolution speed.

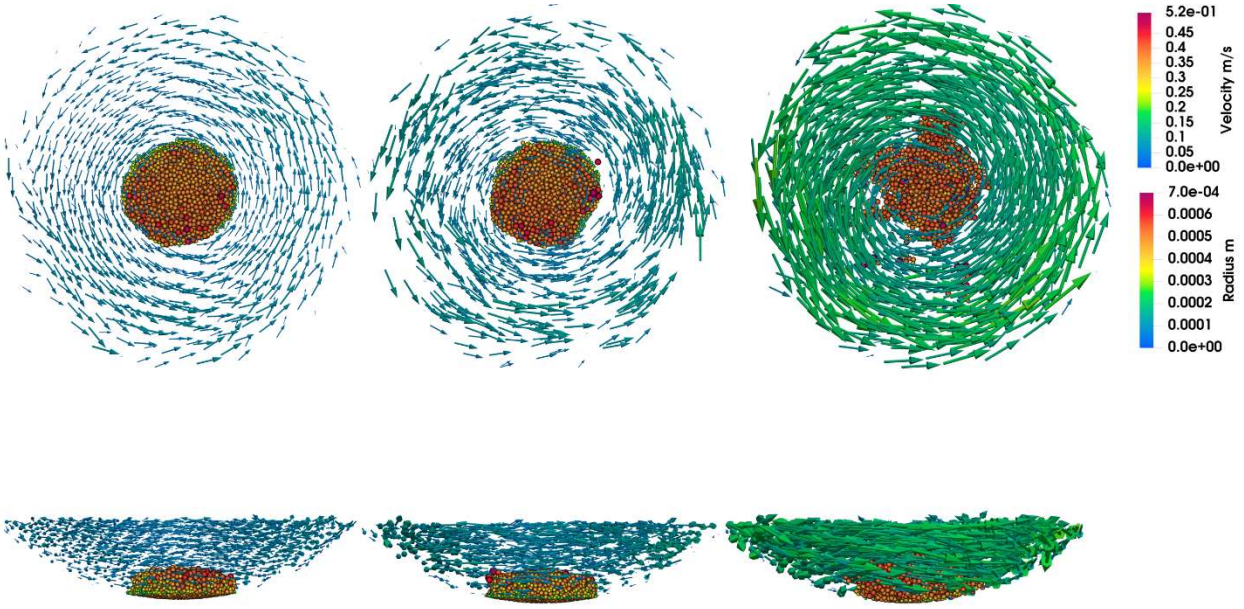

Figure 3.11 Vector visualization of the velocity field. The vector size is proportional to the magnitude of velocity. The direction of the arrow indicates the direction of fluid movement. The vector color also indicates the velocity magnitude. Column from left to right: RPM=40, RPM=50, and RPM=85. First row: view from the top. Second row: view from the side.

3.5.5 Impact by stirring rate:

To study the impact of different rotation speeds, a tablet dissolution process in USP apparatus II is simulated under different paddle rotation RPMs (40, 50, and 85). In Figure 3.12, we compare the impact of paddle rotation speed. We can see that higher rotation speed induces higher velocity and a faster particle dissolution rate. The velocity on the outer part of USP apparatus II in each velocity field is higher than the inner part. There is a noticeable low-velocity region in the middle of USP apparatus II. Also, as the rotation speed increases, the overall velocity

increases. In terms of the concentration field, the increase of rotation speed will facilitate the dissolution of the drug by introducing higher velocity in the highly concentrated area. We can see that as the rotation speed increases, the high concentration region at the bottom of USP apparatus II spreads wider. This is because higher velocity will induce the concentration field's elevated convection.

Next, we plot the concentration in USP apparatus II over time for the different rotation speeds of 40, 50, and 85. As shown in Figure 3.13, a higher rotation speed will induce a faster drug concentration increase. This is further confirmed in Figure 3.11, higher rotation speed induced faster drug particle fraction release speed.

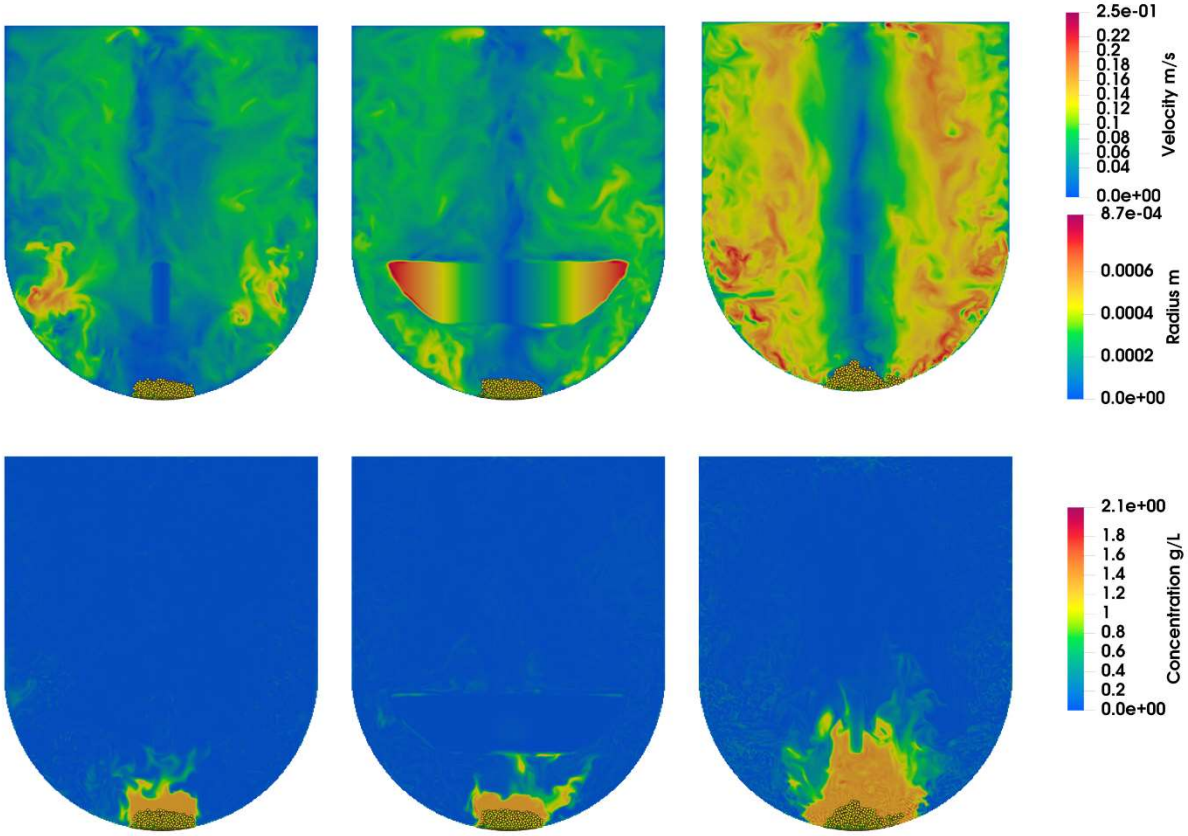

Figure 3.12. Comparison of concentration and velocity distribution in USP apparatus II at time = 8s at different paddle rotation speeds (RPM). First row: concentration field. Second row: velocity field. For each column from left to right: RPM=40, RPM=50, and RPM=85.

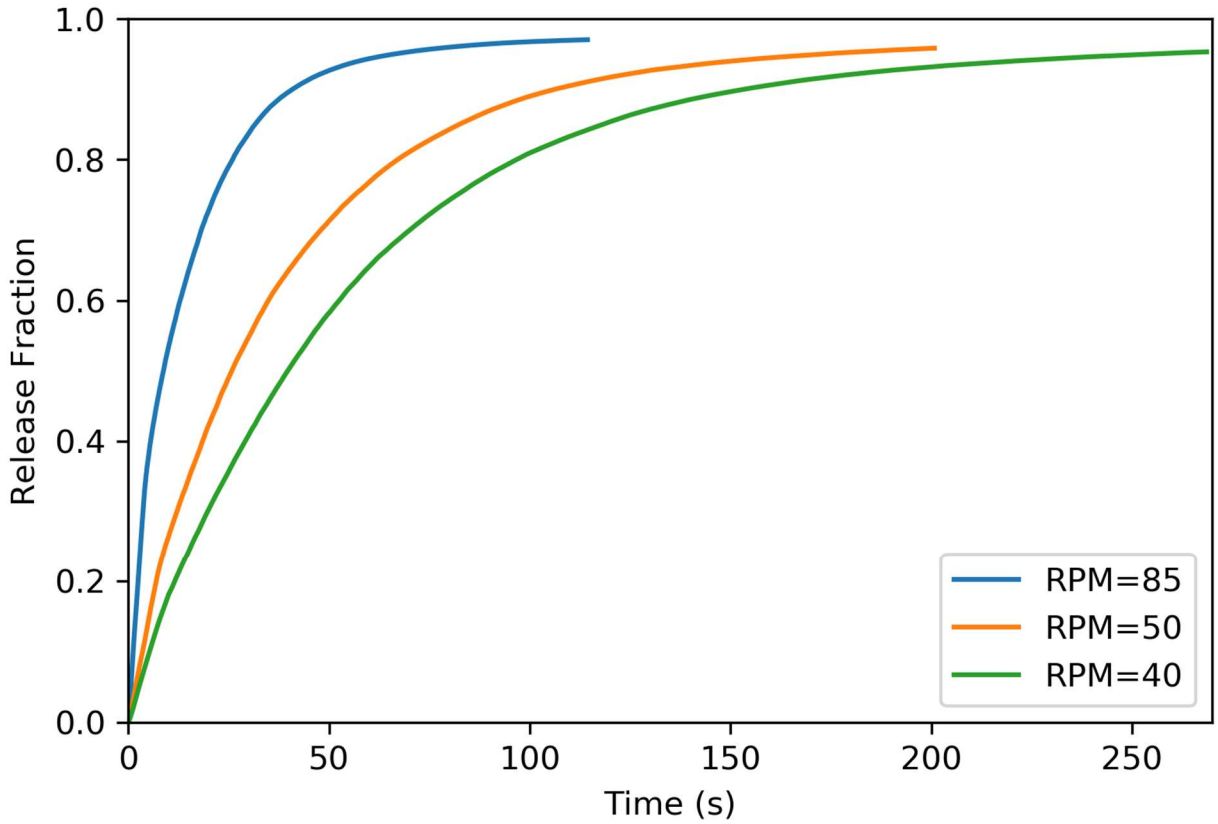

Figure 3.13. Concentration over time for different rotation speeds. A higher rotation speed results in a faster increase in drug release fraction.

3.5.6 Impact by dissolution rate:

We analyze the concentration of drug change over time at the sampling point in USP apparatus II. Here, we should note that to reduce computation time, we used a lower resolution of 101×101×121 grid to do the simulation for this experiment. First, we analyze the impact of different dissolution constants K. Here K_0 is the dissolution constant of sodium carbonate. As shown in Figure 3.14, a higher dissolution constant K will induce a faster concentration increase.

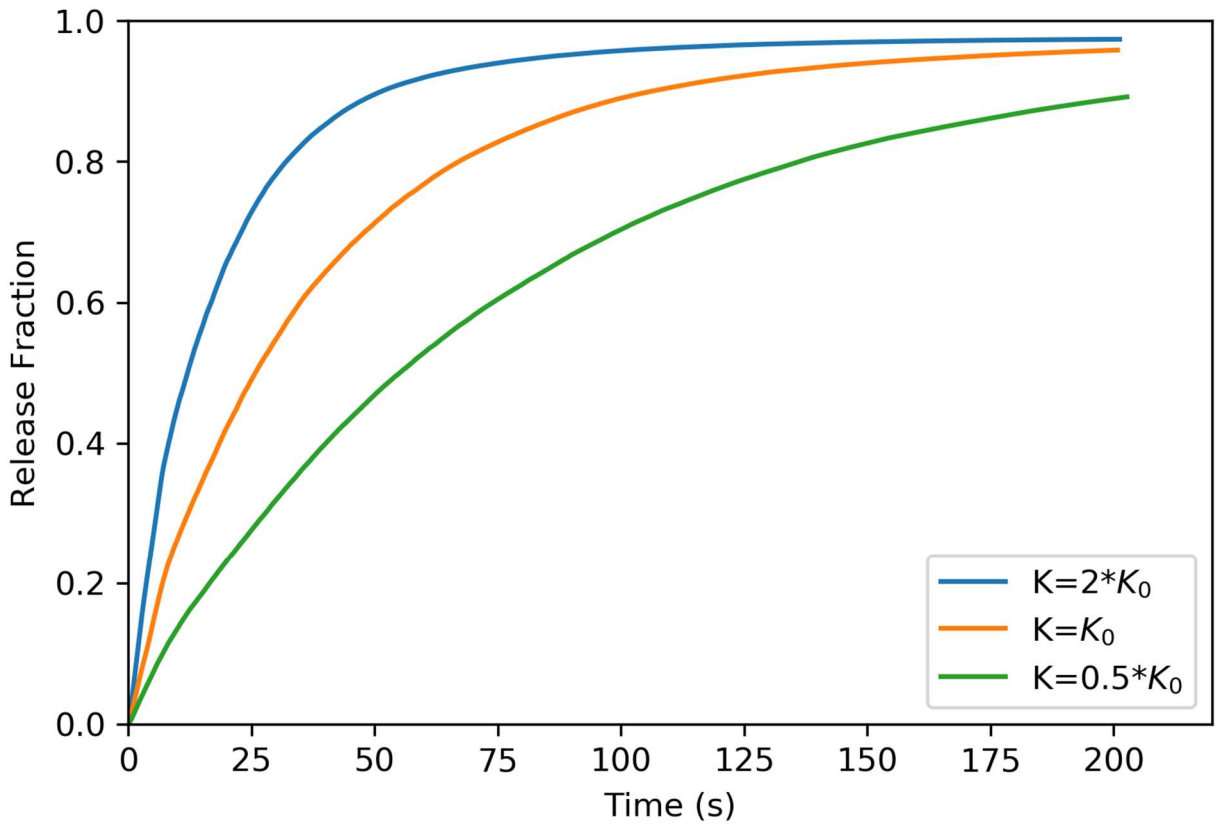

Figure 3.14. Concentration over time for different dissolution constant K. A higher dissolution constant results in a faster increase in drug release fraction.

3.6 Conclusion:

In this paper, we showed a comprehensive coupled LBM and DEM model for the USP apparatus II dissolution simulation. Previous models for the USP apparatus II dissolution test could not directly predict the dissolution of particles and the concentration change in real-time. Most of them could only simulate the velocity field in USP apparatus II [27, 33]. Thus, they can only predict tablet dissolution by calculating the dissolution constant on the tablet's surface [27]. Other efforts try to simulate the velocity field with commercial software and import the velocity field to simulate the concentration field [39, 40]. However, this kind of simulation is not scalable, and the coupling is only one direction, which means tablet particles' impact could not be considered. Compared to their models, our model can simulate the bidirectional fluid-particle interaction. Also, the simulation runs in real-time, which means the hydrodynamic condition the paddle rotation causes is directly coupled with the mass transfer and convection–diffusion of drug particles.

1. By characterizing the concentration field near the particles, we found that under certain conditions, when the drug dissolves fast, particles on the side of the tablet dissolve faster than those on the top of the tablet. Further, by analyzing the concentration and velocity field, we showed that the drug concentration of the top of the tablet is usually higher than that of the side of the tablet. Tangent velocity means that particles on the side are exposed to higher fluid velocity, thus the local convection on the side is faster than that on the top of the tablet.
2. We quantitively analyzed the bulk particle dissolution and concentration change in USP apparatus II. With further development, we can quantitively predict the impact of different formulations and processing of the tablet on the drug's pharmacokinetics. This paves the path toward *in-silico* realization of Quality by Design (QbD) concept of drug formulation design.

Our *in-silico* model is one crucial step toward the rational design of drug formulation. However, there are still some limitations that need further improvement. To accurately couple the LBM and DEM models, the lattice around the DEM particles should be dense enough. Currently, in our model, we use a uniform lattice. This makes the current model computationally expensive. One possible optimization to improve the efficiency is to impose multi-level lattices, which means using only dense lattices on the space surrounding the particles. Thus, the overall computation time could be further decreased. Also, currently, the DEM model is still coarse because we only used a maximum of 2,000 particles to represent the tablet. A more accurate model with higher resolution should be further developed.

Our model shows the ability of LBM and DEM in simulating the dissolution process in USP apparatus II. This is the first time the whole dissolution process of tablet particle dissolution in USP apparatus II has benn simulated. Our model shows the ability of the *in-silico* model to simulate the dissolution process. This model could be further used in developing new drug formulations, and assessing the pharmacokinetics of different drugs and formulations. This makes the rational and quantitative design of drug formulation possible.

CHAPTER 4. TABLET COMPRESSION AND DISSOLUTION SIMULATIONS USING COUPLED DISCRETE ELEMENT AND LATTICE BOLTZMANN METHODS

4.1 Abstract

In this paper, we simulate tablet compression and dissolution in the USP apparatus II through the discrete element method (DEM) and lattice Boltzmann method (LBM). The drug particles are represented as DEM particles. The particles are compressed into a tablet to enable us to study the effects of different formulations and processing parameters on tablet dissolution. We first simulate the tablet compression process with DEM, then the tablet is placed in the USP apparatus II, which is simulated with LBM. Overall, we present in this paper the feasibility of coupling DEM with LBM for tablet formulation design and testing.

4.2 Introduction

Tablets constitute a popular oral dosage form. The disintegration of a tablet and, subsequently, the release kinetics of the active pharmaceutical ingredient (API), are facilitated by utilizing swelling polymers as excipients. When a tablet encounters the fluid in the gastrointestinal (GI) tract, water will diffuse into the disintegrates, causing them to swell and the tablet to break up into tiny granules. The disintegration process clearly governs the drug release kinetics, thus playing a pivotal role in determining drug absorption and eventual bioavailability. Given the foregoing, it is essential to fully understand and even predict the disintegration process of a tablet to come up with a rational tablet formulation design and to minimize the time and cost involved in *in vitro* and *in vivo* tests. As disintegration and dissolution tests are routinely used and are required for product release and quality assurance, understanding how a tablet formulation and its manufacturing processes affect dissolution kinetics could further improve compendial methods and new test standards.

To date, two major simulation approaches have been developed for tablet disintegration, namely, data-driven modeling and physics-based prediction. The former treats the disintegration (and dissolution) by generating phenomenological models through the data-fitting of experimental data. The latter attempts to overcome the abovementioned challenge by using first principles to solve the physical processes involved in disintegration. The limitation of data-driven approaches stems from the empirical nature of modeling, making the extrapolation of new formulation designs quite challenging. Our interest, therefore, is focused on the physical approach.

There are a few research efforts in the literature for developing physical models of tablet disintegration. Lamberti et al. introduced the finite element method (FEM), which proved to be a workable model for drug release from tablets [1]. However, this model did not take into account the fact that most tablets have different components that distribute unevenly throughout and can significantly influence the drug disintegration process. Meanwhile, Kimber developed a discrete element model for simulating drug disintegration and dissolution [131-133]. This model was capable of considering the non-uniform distribution of the API and the excipients' heterogeneity. However, it neglected the fluid dynamics around the tablet. The impact of the liquid flow can exert a significant influence on the disintegration (and dissolution), for example, due to mechanical stirring or peristaltic wave in the GI.

As such, we have sought to develop physics-based simulation methods of tablet disintegration and dissolution. We mainly consider modeling three fundamental processes of tablet dynamics, namely, particle-particle interaction, particle-fluid interaction, and hydrodynamics. It is expected that combining the lattice Boltzmann method (LBM) and discrete element method (DEM) would allow us to fully model the particle-liquid dynamics and simulate the disintegration and dissolution process in a liquid environment. Notably, computer modeling and simulation require a quantitative description of a tablet product, including its particle properties and inter-particle interactions. By experimentally determining these properties, we expect to establish a mechanical relationship between the tablet construct and its dissolution kinetics. This could give rise to a rational design and quality assurance of tablet products and, significantly, lead to an improvement on existing compendial methods and the development of new test standards for the industry and regulatory agencies.

Our overall simulation framework is innovative. It fully considers the tablet micro-structure and composition, as well as the liquid environment in which it dissolves. The approach could not only simulate various formulation designs and the impact of manufacturing processes (e.g., compression force) on the disintegration and dissolution process but also enable the simulation of such processes in a biological environment. Moreover, using the computational approach is a novel strategy to help model the tablet structure and inter-particle interactions from experimental measurements. A combination of computer modeling and experimental measurement could shed light on tableting and the quality control of tablet products, resulting in new designs and better performances of solid dosage forms.

4.3 Methodology

We applied numerical methods for tablet compression, disintegration, and dissolution simulations in this project by coupling DEM with LBM. Herein, we introduce the numerical methods used in this paper.

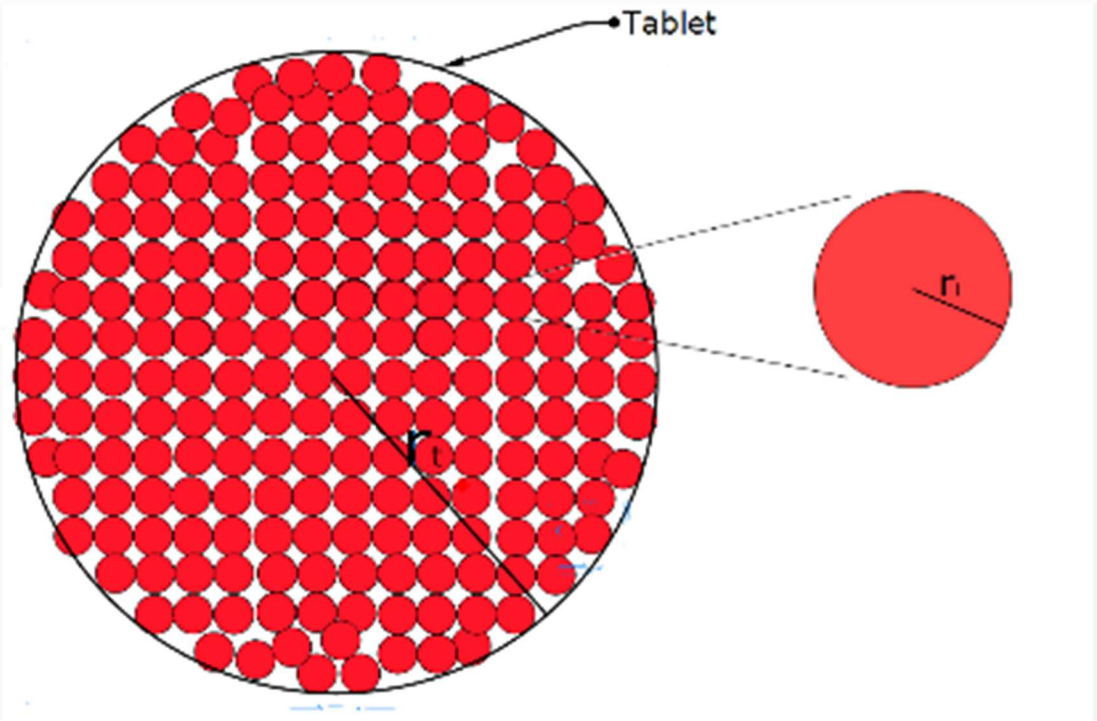

Figure 4.1. The tablet described in the bonded particle model. Each tablet consists of many particles.

4.3.1 Tablet compression simulation with the Edinburgh-Elasto-Plastic-Adhesive (EEPA) DEM model

We modeled a tablet as an ensemble of solid particles, as shown in Figure 4.1. Each particle is explicitly modeled and treated as the fundamental unit. A particle (e.g., API) may dissolve in liquid, resulting in particle size reduction and release of molecules in the environment. A particle (e.g., excipient) may take up water from the liquid environment, swell, and exert forces on neighboring particles (in the tablet). To model the drug and excipient particles in a tablet, we must consider the interactions or bonding forces between two particles.

As two solid particles approach each other, there is an attractive force due to *van der Waals* interaction (as well as possible electrostatic interaction if the particles bear surface charges). As they continue to get closer, especially during the tablet compression stage, the particles undergo the following deformation: recoverable, elastic, and then (partial) plastic deformation. Such deformations require energy, indicating the repulsive nature that emerges when a particle is compressed. The traditional Hertz-Mindlin contact model cannot simulate the loading and

unloading processes of tablet compression. There have been a few contact models describing such interparticle interactions for DEM simulations. One such model is the EEPA contact model [92-95]. When two particles are pushed together, the repulsion is modeled by the overlapping distance (i.e., $\delta_{n_{ij}}$ in Figure 4.2). When they are pulled apart, the attraction force will keep them together until the external force exceeds the attraction force. In a similar approach of using DEM to simulate the tableting process, the same elastic repulsion model when particles are pushed against each other is used reciprocally to describe their attraction when pulled apart [96].

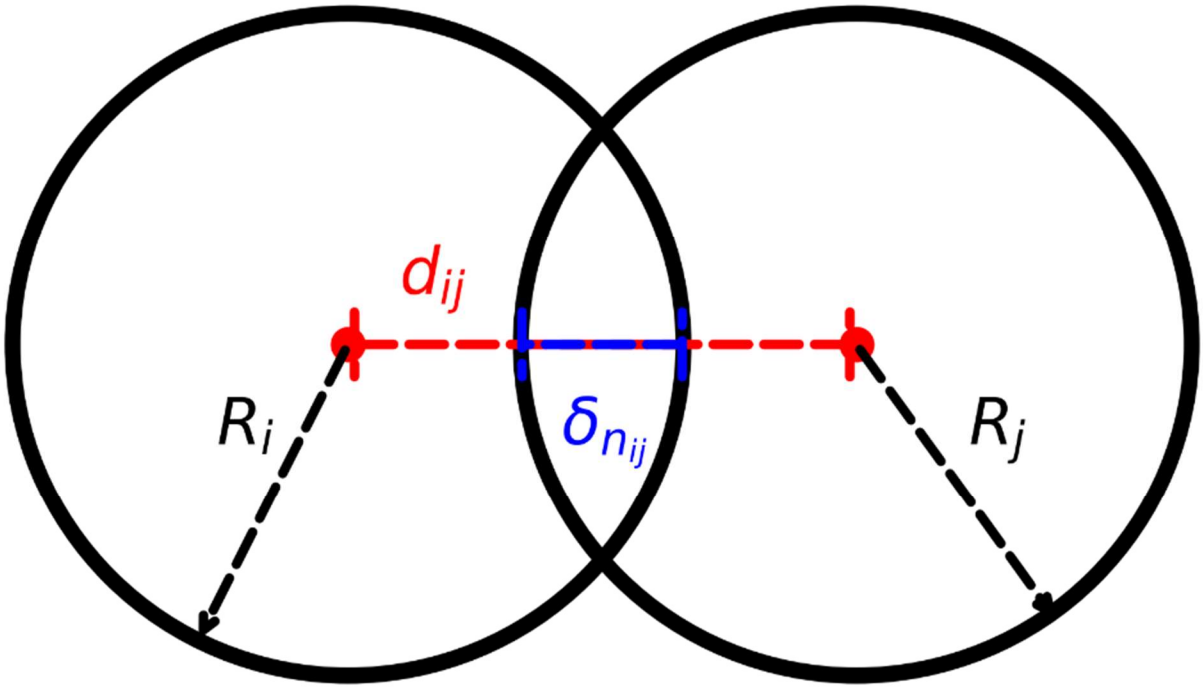

Figure 4.2. DEM particle-particle interaction. The contact force is modeled based on the overlap between particles. When two particles get close to each other, the overlap $\delta_{n_{ij}}$(blue dashed line) between two particles is calculated based on their relative distance d_{ij} (red dashed line), as shown by the red line and the radius *(R_i* and *R_j)* of these particles.

In the EEPA model, we used an adhesive force to represent the effect of several different forces, such as *van der Waals* forces, sintering and chemical bonding, electrostatic forces, and mechanical forces [92-95]. The total force $\mathbf{f_n}$ is the sum of two different components, namely, hysteretic component f_{hys} and damping (dashpot) component f_{nd}.

$$\boldsymbol{f_n} = \left(\mathrm{f}_{hys} + \mathrm{f}_{nd}\right)\mathbf{u} \qquad \text{Eq. 4.1}$$

The hysteretic component of the EEPA model includes three different phases: loading, unloading/reloading, and adhesive phase. These three phases are labeled in Figure 4.3. These models can either be linear (n=1) or non-linear (n ≠1). In Eq. 4.2, we describe the three phases using the following three equations:

$$\mathrm{F_{hys}} = \begin{cases} \mathrm{f_0} + \mathrm{k_1}\delta^{\mathrm{n}} & \delta^{\mathrm{n}} < \mathrm{k_2}(\delta^{\mathrm{n}} - \delta_{\mathrm{p}}^{\mathrm{n}}) \\ \mathrm{f_0} + \mathrm{k_2}(\delta^{\mathrm{n}} - \delta_{\mathrm{p}}^{\mathrm{n}}) & \mathrm{k_2}(\delta^{\mathrm{n}} - \delta_{\mathrm{p}}^{\mathrm{n}}) < \mathrm{k_1}\delta^{\mathrm{n}} \\ \mathrm{f_0} - \mathrm{k_{adh}}\delta^{\mathrm{n}} & \mathrm{k_2}(\delta^{\mathrm{n}} - \delta_{\mathrm{p}}^{\mathrm{n}}) < \mathrm{k_{adh}}\delta^{\mathrm{n}} \end{cases} \qquad \text{Eq. 4.2}$$

In Figure 4.3 and Eq. 4.2, δ is the overlap between two particles, as shown in Figure 4.2. Notably, there is a constant pull-off force $\mathrm{f_0}$. This is the force needed to pull two particles apart when the overlap between two particles is zero. Based on the value of overlap δ, the three different phases can be described as follows:

1. Loading phase (represented by the red lines in Figure 4.3): When two particles approach each other and the overlap δ starts to increase from zero, the hysteretic force will increase either linearly (n=1) or non-linearly (n≠1) with the coefficient of $\mathrm{k_1}$. When the overlap reaches a maximal value δ_{max}, the loading phase will stop.
2. The unloading/reloading phase (represented by the green lines in Figure 4.3): When the two particles move away from each other and the overlap between particles decreases, the forces will start to decrease with the coefficient of $\mathrm{k_2}$. Due to the plastic deformation of a particle in the loading phase, the unloading $\mathrm{k_2}$ will be bigger than the loading coefficient $\mathrm{k_1}$. The particle overlap is called plastic overlap δ_p when the force $\mathrm{f_{hys}} = 0$. If the overlap between particles increases during this time, this means reloading has occurred. In this case, the force will increase with a coefficient of $\mathrm{k_2}$. If the reloading force exceeds the maximum force that the particle experienced in the loading phase, the coefficient will switch back to $\mathrm{k_1}$.
3. The adhesive phase: If the overlap between the particles continues to reduce and become smaller than δ_p, a negative adhesive force that pulls two of the particles together will be created. If the overlap continues to decrease, the adhesive force will reach a minimum value of $\mathrm{f_{min}}$. After reaching the minimal value, the absolute magnitude of the adhesive

force will start to decrease with a coefficient of k_{adh}. The minimal value of f_{min} could be calculated using, where $\Delta\gamma$ is the surface adhesion energy and a is the contacting radius:

$$F_{min} = \frac{3}{2}\pi\Delta\gamma a \quad \text{Eq. 4.3}$$

The damping (dashpot) component of EEPA model f_{nd} could be calculated using Eq. 4.4:

$$f_{nd} = \beta_n v_n \quad \text{Eq. 4.4}$$

where v_n is the magnitude of the relative normal velocity and β_n is the normal dashpot coefficient.

In a similar approach of using DEM to simulate the tableting process, an elastic repulsion model when particles are pushed against each other is used reciprocally to describe their attraction when pulled apart [96].

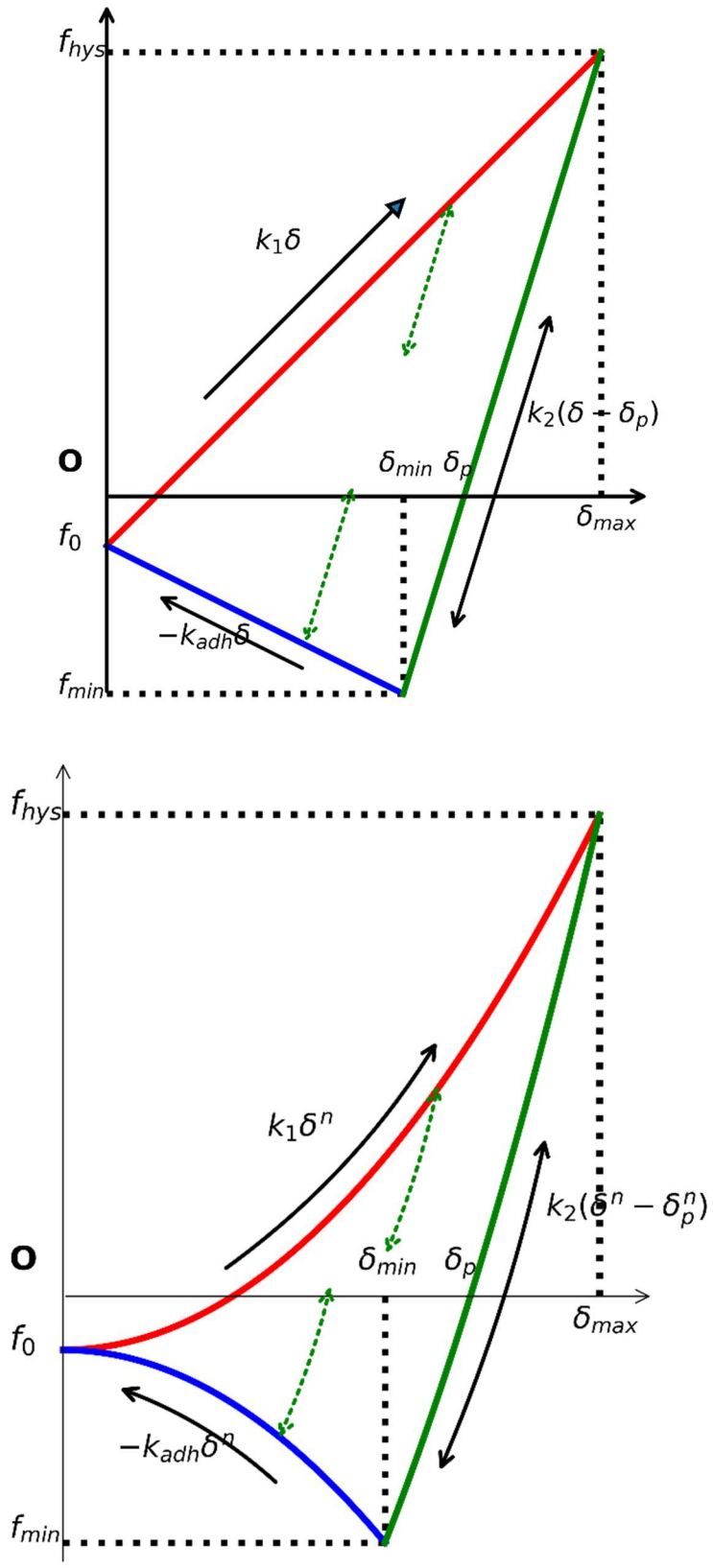

Figure 4.3. EEPA models: linear (n=1) and non-linear (n>1).

4.3.2 LBM and DEM coupled approach for tablet dissolution

We used a coupled LBM and DEM approach to simulate the particle-liquid interactions, as well as the particle-particle interactions in a tablet and in the dissolution medium. The liquid was treated as a continuum, while the particles were treated as individual particles. Herein, we briefly introduce the methods, followed by the preliminary results and our proposed plan in this project.

Lattice Boltzmann Method(LBM)

In LBM, space is discretized as a regular lattice and fluid is described as an ensemble of imaginary fluid molecules that move to neighboring lattice nodes during each timestep. Particle distribution function (*f*) is devised to represent the fluid from which the velocity and pressure of the fluid can be calculated. LBM centers on the Boltzmann equation (Eq. 4.5), where Ω is the so-called collision operator that is often described by the Bhatnagar, Gross, and Krook (BGK) model (Eq. 4.6) [134]:

$$\frac{\partial f}{\partial \mathrm{t}} + \mathrm{c} \cdot \nabla f = \Omega \qquad \text{Eq. 4.5}$$

$$\Omega = \omega(f^{eq} - f) = \frac{1}{\tau}(f^{eq} - f) \qquad \text{Eq. 4.6}$$

where c is the lattice velocity, ω is the collision frequency, and τ is the relaxation factor. With BGK, the Boltzmann equation becomes:

$$f_\alpha(\boldsymbol{x} + e_\alpha \delta t, t + \delta t) - f_\alpha(\boldsymbol{x}, t) = -\frac{1}{\tau}[f_\alpha(\boldsymbol{x}, t) - f^{eq}(\boldsymbol{x}, t) \qquad \text{Eq. 4.7}$$

where $f_\alpha(x,t)$ is the density distribution function at α discretization direction. The left side of the equation describes the change of the distribution function as a result of the exchange of momentum between neighboring lattice nodes due to bulk advection and molecular diffusion. It is called the "streaming" stage. The right side, called the "collision" stage, describes the mixing or collision of molecules that drive the flow to the equilibrium particle distribution function.

Immersed Moving Boundary Method (IMBM)

In order to deal with the interactions between fluid and solid particles, we will adopt the IMBM. As shown in Figure 4.4, the fluid-solid interaction is modeled by considering the solid fraction of each lattice node in space. This is achieved by adding additional collision terms to the solid nodes [135, 136]. The collision operator Ω becomes:

$$\Omega = \frac{1}{\tau}(1-B)(f^{eq}-f) + (1-B)F + B\Omega^S \quad \text{Eq. 4.8}$$

where B is related to the solid ratio ε of node:

$$B = \frac{\varepsilon(\tau - 0.5)}{(1-\varepsilon) + (\tau - 0.5)} \quad \text{Eq. 4.9}$$

F is the external force applied to the boundary point of the particle. The additional term Ω^S is used to describe the liquid-particle interactions.

Particle Dissolution

LBM is used to solve the advection-diffusion equation of dissolution as follows [137]:

$$\frac{\partial C}{\partial t} + \nabla \cdot (C\boldsymbol{u}) = \nabla \cdot (D\nabla C) + q \quad \text{Eq. 4.10}$$

where q is a source term (i.e., dissolution), C is the concentration, and D is the diffusion coefficient. The LBM solution is:

$$g_\alpha(\boldsymbol{x} + \boldsymbol{c}_\alpha \delta t, t + \delta t) - g_\alpha(\boldsymbol{x}, t) = -\frac{1}{\tau}[g_\alpha(\boldsymbol{x}, t) - g_\alpha^{eq}(\boldsymbol{x}, t)] + Q_\alpha(\boldsymbol{x}, t) \quad \text{Eq. 4.11}$$

where $g_\alpha(x,t)$ is the density distribution function of the dissolved molecules at α discretization direction. Since we assume that the dissolved drug concentration has little effect on the dynamics of the liquid medium (i.e., $f_\alpha(x,t)$), the velocity field for $g_\alpha(x,t)$ will be taken directly from the calculation of the liquid. Thus, using the same lattice, both density distribution functions can be solved. By making the concentration on the particle's surface equal to the drug solubility, we can simulate the dissolution of the particle. The dissolved concentration can be calculated by:

$$C = \sum g_\alpha + \frac{Q_\alpha \delta t}{2},\ Q_\alpha = (1 - \frac{1}{2\tau}) w_\alpha q \quad \text{Eq. 4.12}$$

where q is the saturated concentration at a lattice point. With the dissolution of the drug particle, the radius of the particle is reduced. This is achieved by updating the radius of the particles based on the mass flux on their surface, as calculated above.

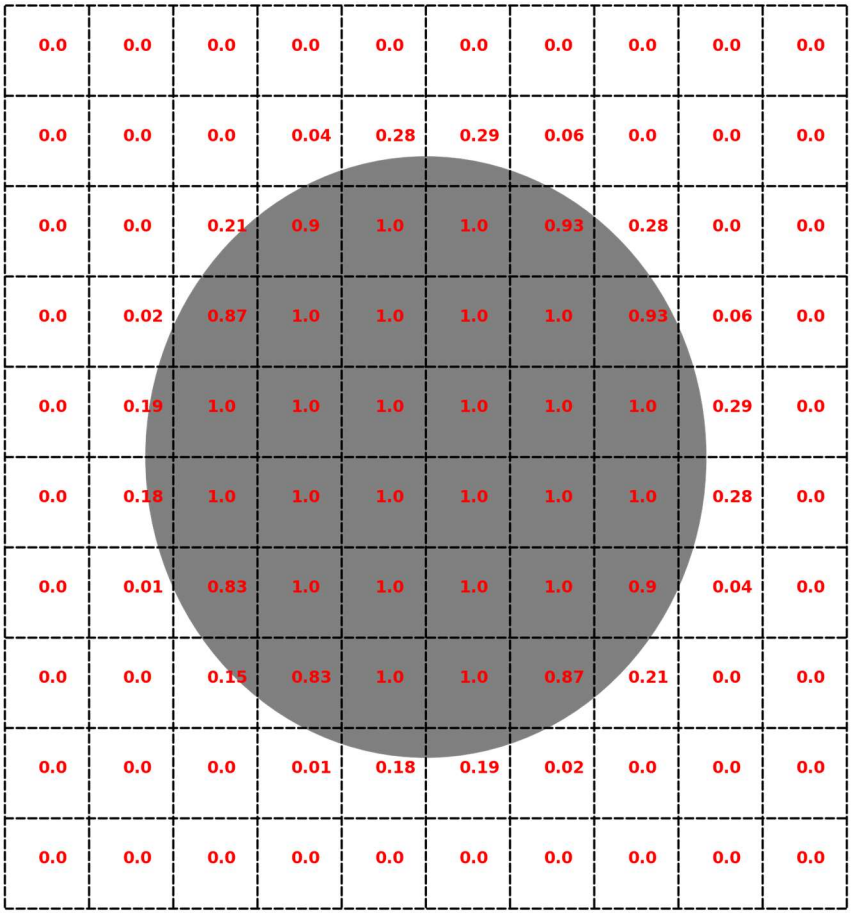

Figure 4.4. Coupling LBM and DEM with IMBM. Solid particle (dark gray cell) in the fluid (blank cell). The solid ratio ε (red number) of each lattice node is calculated based on the part covered by a solid particle in the lattice node.

Particle Water Uptake

A disintegrant particle will absorb water. The uptake of water and the swelling of particle i will change the radius (r_i) of the particle, exerting repulsive forces to its neighboring particles and contributing to the breakup of the tablet. The kinetics can be described by the following equations [131-133]:

$$\frac{\mathrm{d}m_i^w}{\mathrm{dt}} = \sum_{j \neq i} A_i^f \frac{D_i^w}{2r_i} (\rho^w - c_i^w) \qquad \text{Eq. 4.13}$$

where superscript w and p represent water and polymer (or disintegrant), respectively. A, D, and m denote the contact area between two particles, the diffusion coefficient of water, and the mass, respectively. ρ is density and r is particle radius. The equation accounts for water uptake by a

particle from the medium. The water diffusion coefficients in the dry and fully saturated polymer (disintegrant) can be measured or found in the literature [131].

4.4 Experimental setup

4.4.1 Simulation algorithms

LBM and DEM were coupled to simulate the process of tablet compression, disintegration, and dissolution. In particular, we modeled a tablet as an ensemble of particles containing both API and excipients, as shown in Figure 4.1. The parameters used in our model are listed in Table 4.1. The coupled LBM and DEM algorithm of the simulation is listed below.

1) Initialize the parameters and tablet structure (including all particles and their properties).
2) Initialize the LBM and boundary conditions.
3) Conduct LBM streaming and calculate the fluid velocity $\boldsymbol{u}$ and density ρ.
4) Calculate the water update and update the size and mass of each disintegrant particle.
5) Obtain the hydrodynamic force acting on each particle and the interparticle forces. Thereafter, evaluate the particles' movement, including their rotation.
6) Calculate the particle dissolution.
7) Update the bonding of particles in the tablet.
8) Conduct the LBM collision step and update the distribution function.
9) Go to Step 2 until the maximum timestep is reached.

4.4.2 Tablet structure construct

A tablet is not a simple ensemble of API and excipient particles. It is a construct of the particles formed under high pressure in a die (Figure 4.5). Not only do we need to consider the composition of the tablet and the particle properties (size and size distribution), but we also have to fully consider how the particles interact and bond with each other.

To achieve our objective, we conducted DEM simulations to develop *in silico* models of tablets. As shown in Figure 4.5, particles of API and excipients (disintegrants) were randomly packed in the die model based on the input parameters of particle size and API/excipient composition. Random mixing was assumed, and different compression forces were simulated to push the upper die to the powder bed. The force model by EEPA was used to describe the dynamics and kinetics of particle compression. All particles were considered spherical.

In addition to the mechanical properties of and between the particles of the model drug and excipients, we modelled the water uptake characteristics of the disintegrant (e.g., starch and/or its derivatives). As indicated in the water uptake and swelling model (Eq. 4.13), we needed to ascertain the diffusion coefficients of water in the dry and fully saturated states of the disintegrant. We also had to assess the dissolution rate of the disintegrant in water. A more critical aspect was that the mechanical properties needed to be determined between the disintegrant particles and between the disintegrant and the API particle. As explained above, this can be achieved for dry particles. However, it is a difficult task for disintegrant particles due to varying amounts of water content. For this purpose, we planned to introduce an empirical damping constant for the repulsion or attraction forces, or both, when a disintegrant particle is involved.

Combining the DEM simulation and experimental measurement, we expected to build *in silico* models of a particular tablet formulation compressed by pre-determined forces for the disintegration and dissolution simulations. More importantly, the force parameters estimated from the measurements would allow the high-fidelity simulation of actual tablet products.

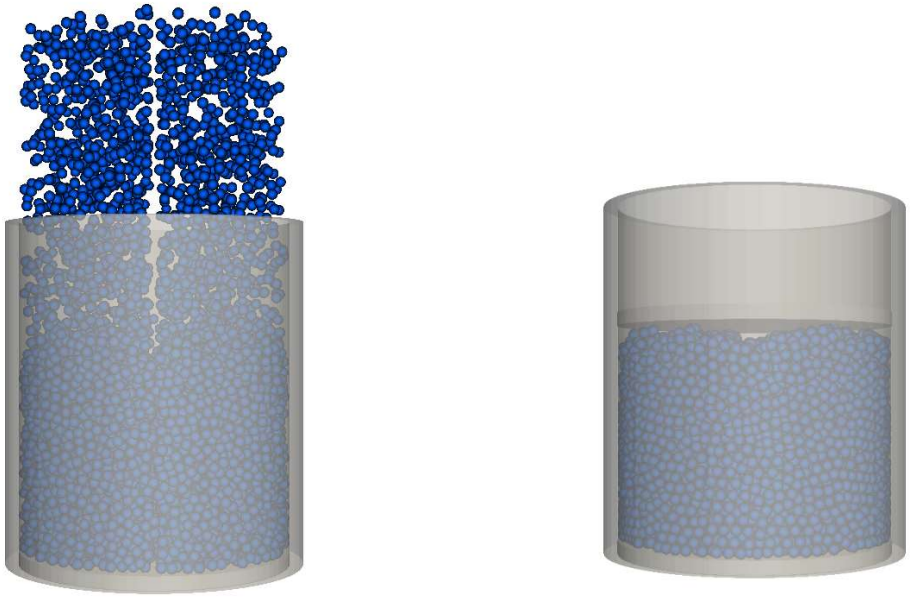

Figure 4.5. Tablet particles packing and compression in a die.

4.4.3 Dissolution simulation in USP apparatus II

Lastly, we simulated tablet disintegration and dissolution in the USP Apparatus II (Figure 4.6). The dissolution vessel and paddle were modeled by meshes and simulation boundaries; the rotation of the paddle was implemented as the moving boundary in LBM. Due to the limitations of our computing power, the tablet was modeled as a compact made of around 1200 particles representing the drug, disintegrant, and diluent.

In particular, by running simulations, we aimed to test the influence of the following parameters/conditions:

1. The bonding strength between particles (to reflect the material properties and compression force)
2. The disintegrating power (to reflect the use of different disintegrants)
3. The dissolution rate of the drug (to reflect different drug products)
4. The stirring rate

By setting up the above calculations, we expected to simulate tablet disintegration under various fluid dynamic conditions. Our simulation could yield detailed insight regarding the mechanical movement of water inside the tablet, which is causing the swelling and expansion of particles. Different from existing efforts of simulating tablet dissolution in USP devices [138], our study is intended to model the microstructure of a tablet, influenced by its formulation composition and tableting process. Furthermore, our approach fully considers the hydrodynamic conditions that a tablet experiences in a dissolution device or even in a biological environment. Our simulation could represent a significant leap in simulating and predicting the *in vitro* dissolution of tablet products.

Table 4.1 Parameters for tablet compression, disintegration, and dissolution simulation

Temperature (T)	37 °C
Fluid Density (ρ_f)	993.3 kg/m³
Paddle Rotation Speed	50 RPM
Water Kinetic Viscosity (v_k)	6.97e-7 m²/s
Diffusion Coefficient (D)	1.12e-9 m²/s
Dissolution Constant (K_0)	1.0e-5 m/s
Water Volume (V)	850 mL
Particle Radius (R)	400 μm, 500 μm
Particle Density (ρ_p)	2540 kg/m^3
Number of Particles (N)	around 1200
Young's Modulus (Y)	6.13e6 Pa
Poisson's Ratio (v)	0.225
Coefficient of Restitution (e)	0.8
Coefficient of Static Friction (μ_s)	0.2
Coefficient of Rolling Friction (μ_r)	0.020
Loading Stiffness (k_1)	1.e5
Unloading Stiffness (k_2)	4.e6
Adhesion Stiffness (k_{adh})	5.e4
Adhesion Exponent (n *for* k_{adh})	10
Overlap Exponent (n *for* k_1 *and* k_2)	1.5
Timestep (dt)	6.67e-5(s)
Grid Size of the Model	306×306×363

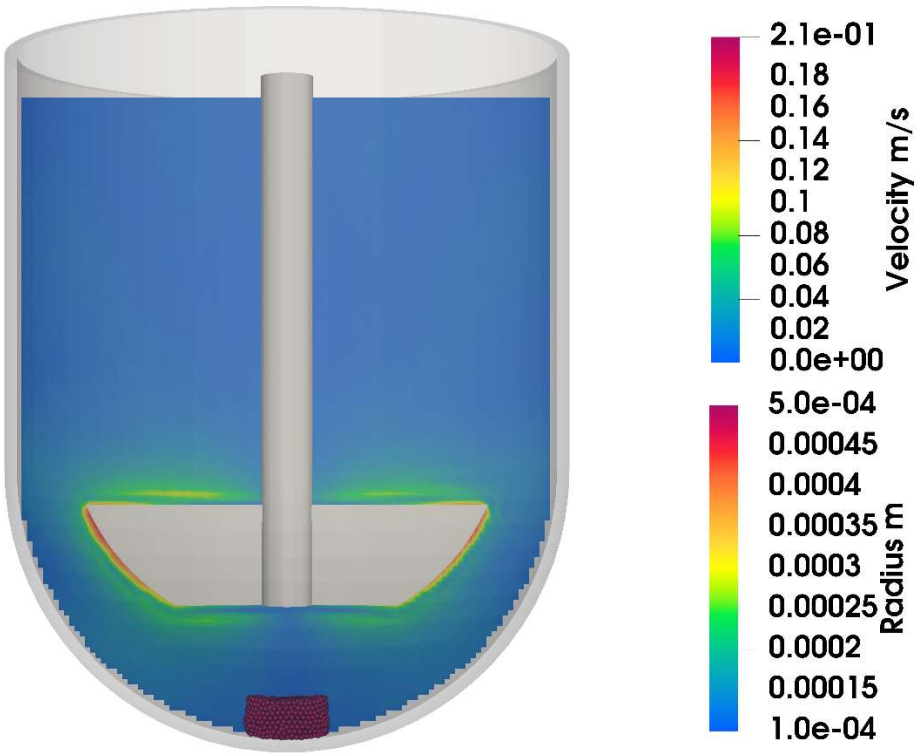

Figure 4.6. USP Apparatus II dissolution test setup. A tablet is compressed at the bottom of USP apparatus II.

4.5 Results

We implemented the above methods by utilizing LBM C/C++ (Palabos®) and DEM libraries (LIGGGHTS®). We tested the integrated LBM/DEM model by setting up an array of benchmark models of tablets formed with 1,200 particle disintegration and dissolution in the fluid (Figure 4.6). The particles were modeled with EEPA DEM and the liquid was modeled by LBM. The fluid-particle interaction was handled through the IMBM. Our results indicated the feasibility and scalability of our model to simulate particle-fluid and particle-particle interactions, as well as the dissolution of particles under hydrodynamic conditions.

4.5.1 DEM compression simulation

Before we performed the tablet dissolution simulations, we needed to compress the drug particles into a compact tablet, which is a widely used drug dosage form. To model this process, we first performed tablet compression with the Mechanical Testing Systems (MTS) Model C43.504 testing frame. With the help of MTS, we were able to measure the compressor movement distance and the overall force on the compressor. Then, we performed DEM simulations to measure the force and moving distance in our model.

In this experiment, we placed 0.1 g VIVAPUR® 200 MCC with an average particle size of 250 μm and bulk density of 0.31–0.37 g/mL in a die with a diameter of 6.3 mm. MTS was used to compress the MCC particles into a tablet. As shown in Figure 4.7, there were two phases: the loading phase and the unloading phase. During the loading phase (indicated by the blue line), as the punch moved down, the particles were compressed and the overall force on the punch increased exponentially. During the unloading phase (indicated by the yellow line), the punch moved up, and the overall force was quickly reduced. To replicate this process, we needed a model that could describe these two phases during compression. As a result, the EEPA model was used, as it could describe the loading and unloading phases by modeling the particle-particle interactions.

The simulations of tablet compression included two steps: packing and compression. In the packing phase, around 1200 particles with a radius of 0.5 mm were placed above the die. Then, these particles fell into the die and relaxed to a staple form. We took gravity, frictional force, rotation, and elasticity into consideration during this step. Once the particles were relaxed and stable in the die, we moved to the compression step. In this step, a punch was placed on top of the particles and moved at a constant rate to simulate the compression process in MTS. We described the particles as soft spheres. The overlap between these spheres increased when the external forces pushed the particles closer to each other. Figure 4.8 shows the DEM simulated particles of pure API before and after compression, illustrating that the compression phase turns the loose particles into a solid tablet. Moreover, we measured the relative distance and overall force during the loading and unloading phases. As shown in Figure 4.9, our simulated compression phase follows the same pattern as that in the MTS compression.

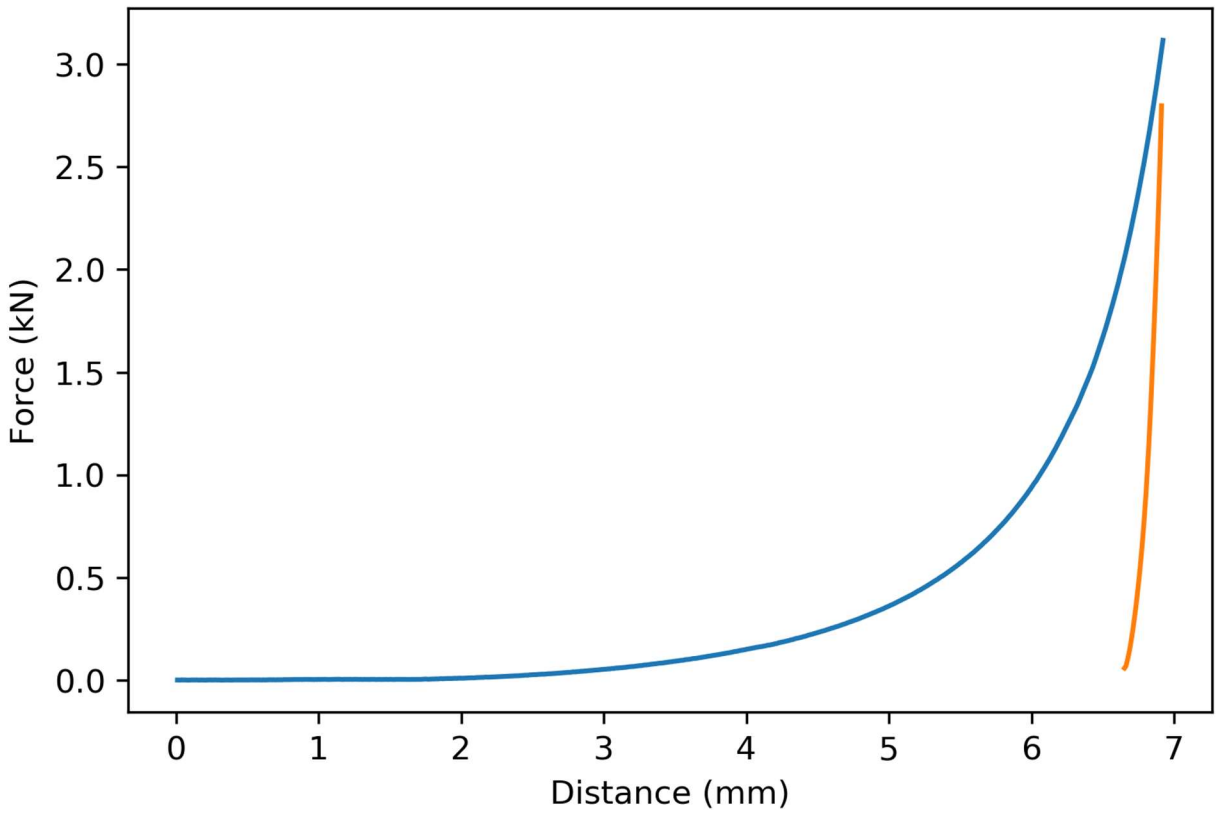

Figure 4.7 Tablet compression with MTS indicating the overall force and the moving distance. The blue line shows the loading phase, while the yellow line shows the unloading phase.

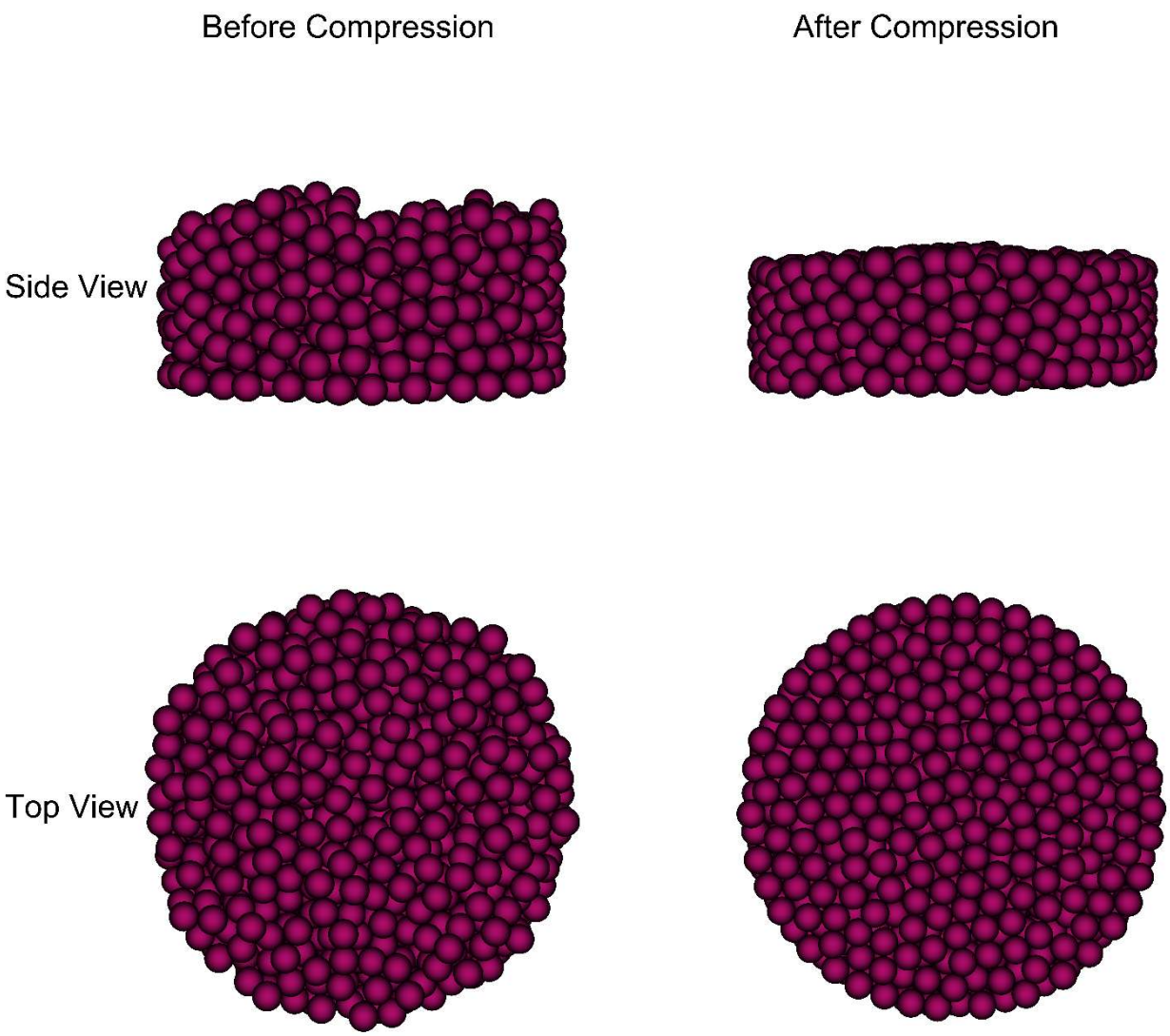

Figure 4.8. Tablet overview before and after compression.

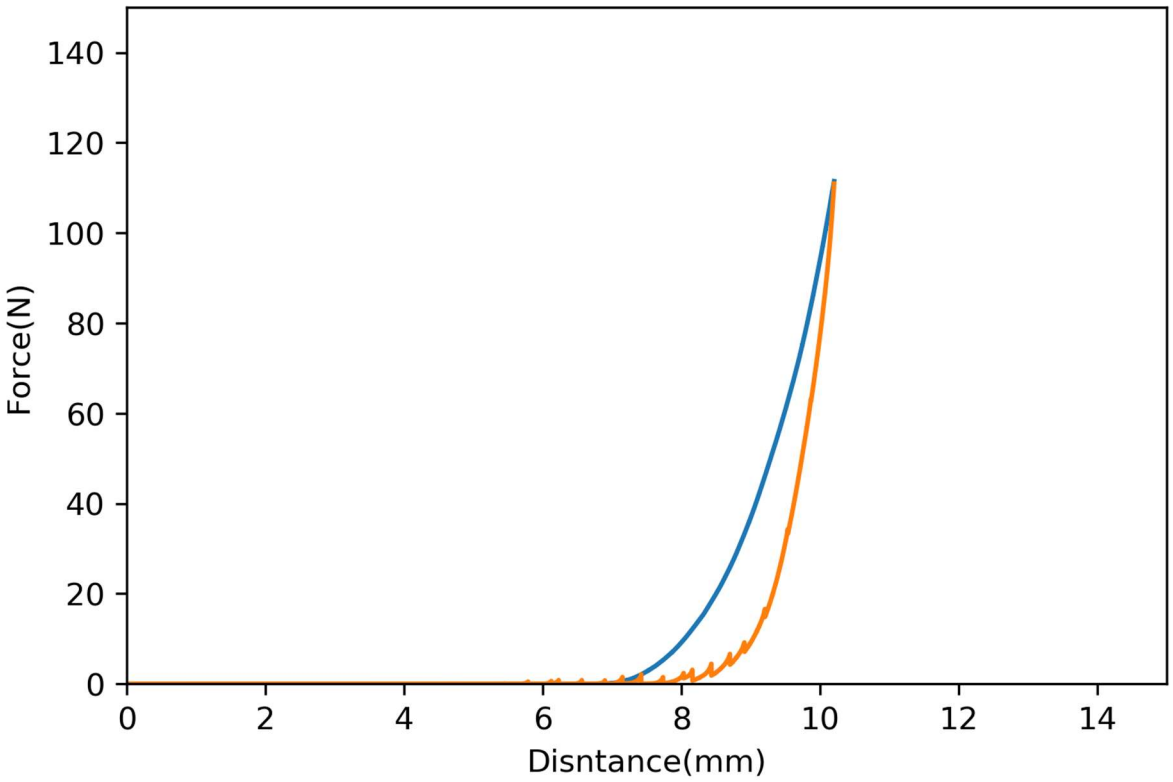

Figure 4.9 DEM simulation of tablet compression. The blue line shows the loading phase, while the yellow line shows the unloading phase.

In addition to the tablets formed with pure API, we also simulated tablets with both API and excipients. As shown in Figure 4.10, we formed the tablet with 75% of its weight constituting API and 25% insoluble excipients. The API particle had a radius of 0.5 mm and the excipient particle had a radius of 0.4 mm. Similar packing and compression steps were performed on these particles to turn them into a tablet. As shown in Figure 4.11, the overall force on the punch is higher compared with the case of pure API because the smaller excipient particles will form more bonds between particles and require higher external force to compress them.

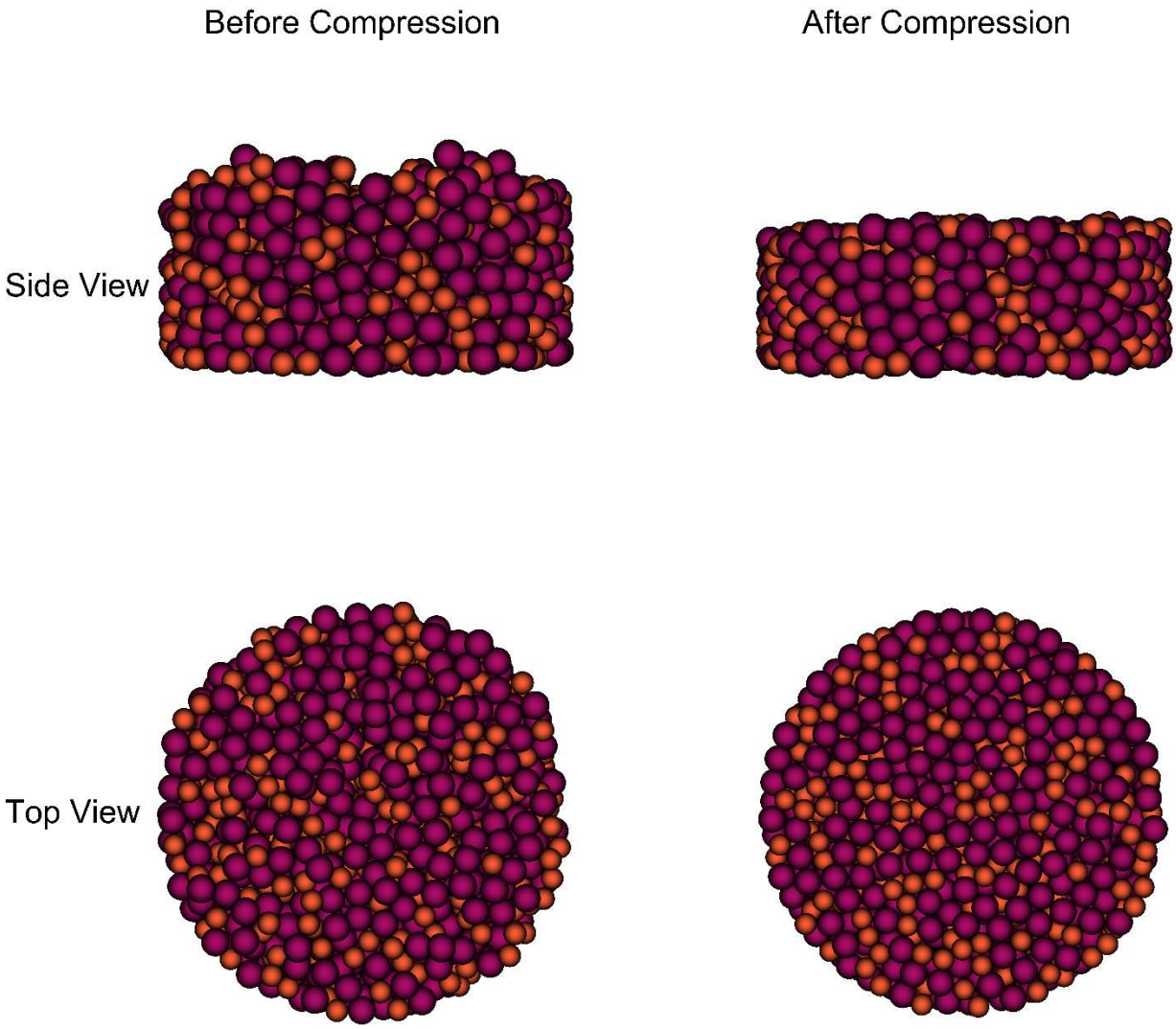

Figure 4.10 Tablet overview before and after compression. This tablet is composed of API (red particles) and excipient (orange particles).

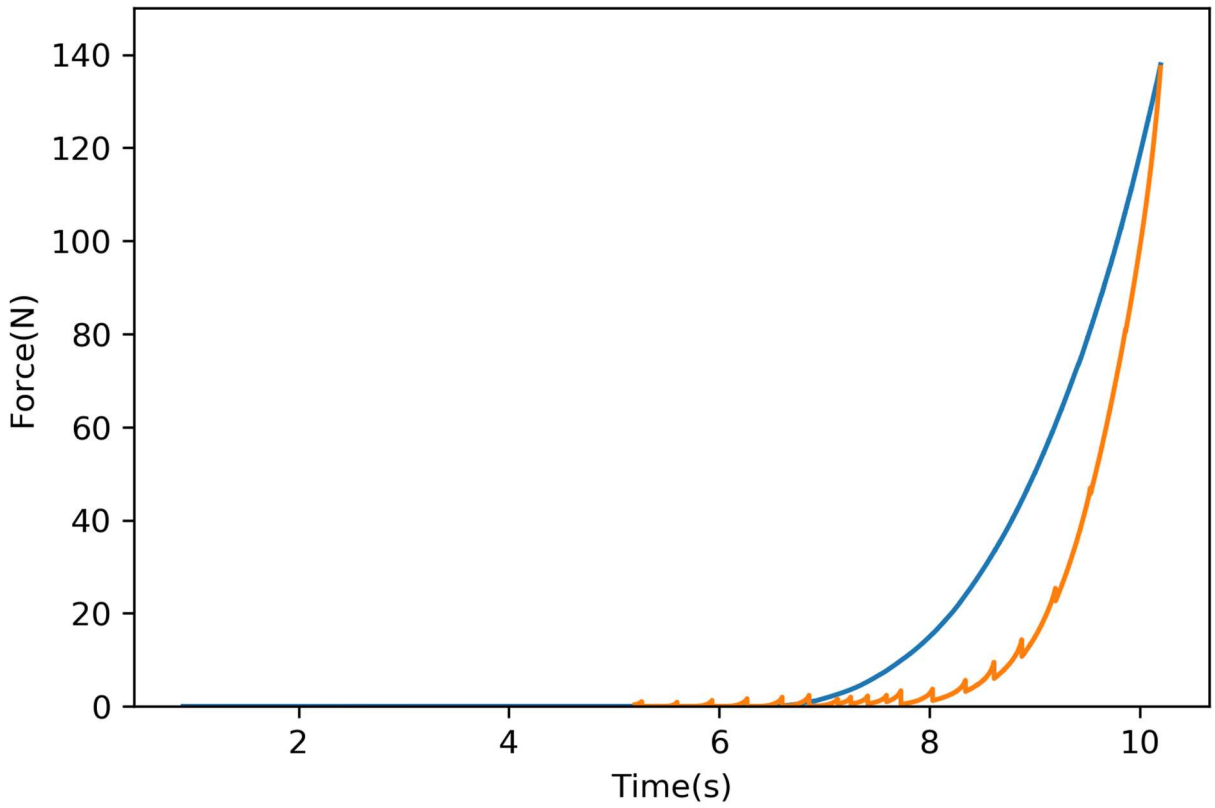

Figure 4.11 DEM simulation of tablet compression. This tablet is composed of API and excipient. The blue line shows the loading phase, while the yellow line shows the unloading phase.

4.5.2 Tablet disintegration and dissolution simulation in USP apparatus II

After we built the DEM simulated tablet, we put the tablet in the USP apparatus II in which the fluid phase is simulated with LBM. We coupled the DEM particles with the LBM fluid through the IMBM. The particle was then placed at the bottom of the USP apparatus II. As the paddle rotated, the fluid moved around and facilitated the disintegration and dissolution of the tablet.

Figure 4.12 presents the velocity field in the USP apparatus II from the side of the device. We can observe that the velocity is fully developed after 6 s. In the fully developed velocity field, there is a low-velocity area in the middle of the USP apparatus II. The field near the paddle has the highest velocity. The concentration field is shown in Figure 4.13. As the tablet particles dissolve, the drug concentration field will change over time. We can also observe that the drug fluid will move upward and be distributed by the paddle.

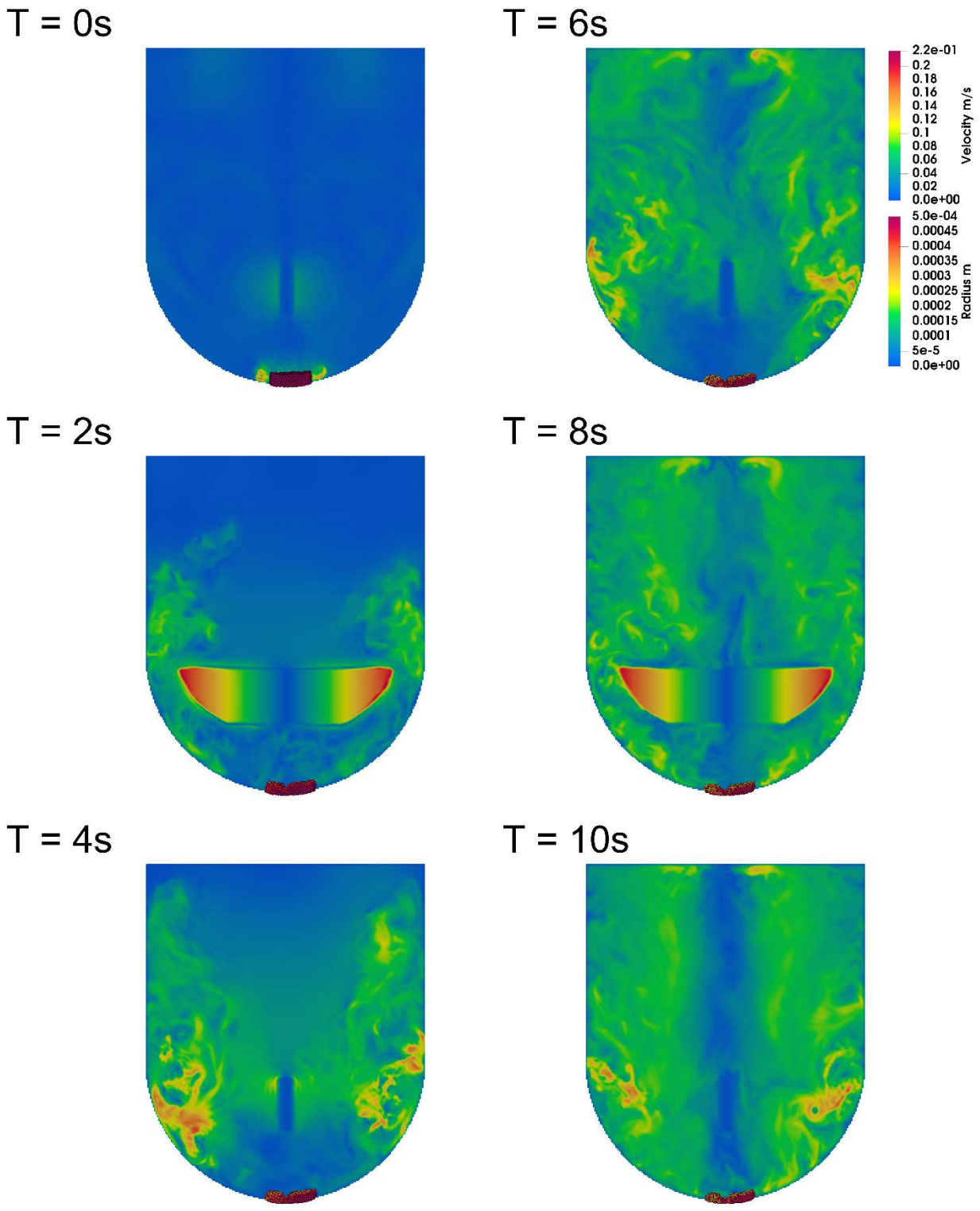

Figure 4.12 Velocity field in the USP apparatus II over time (T).

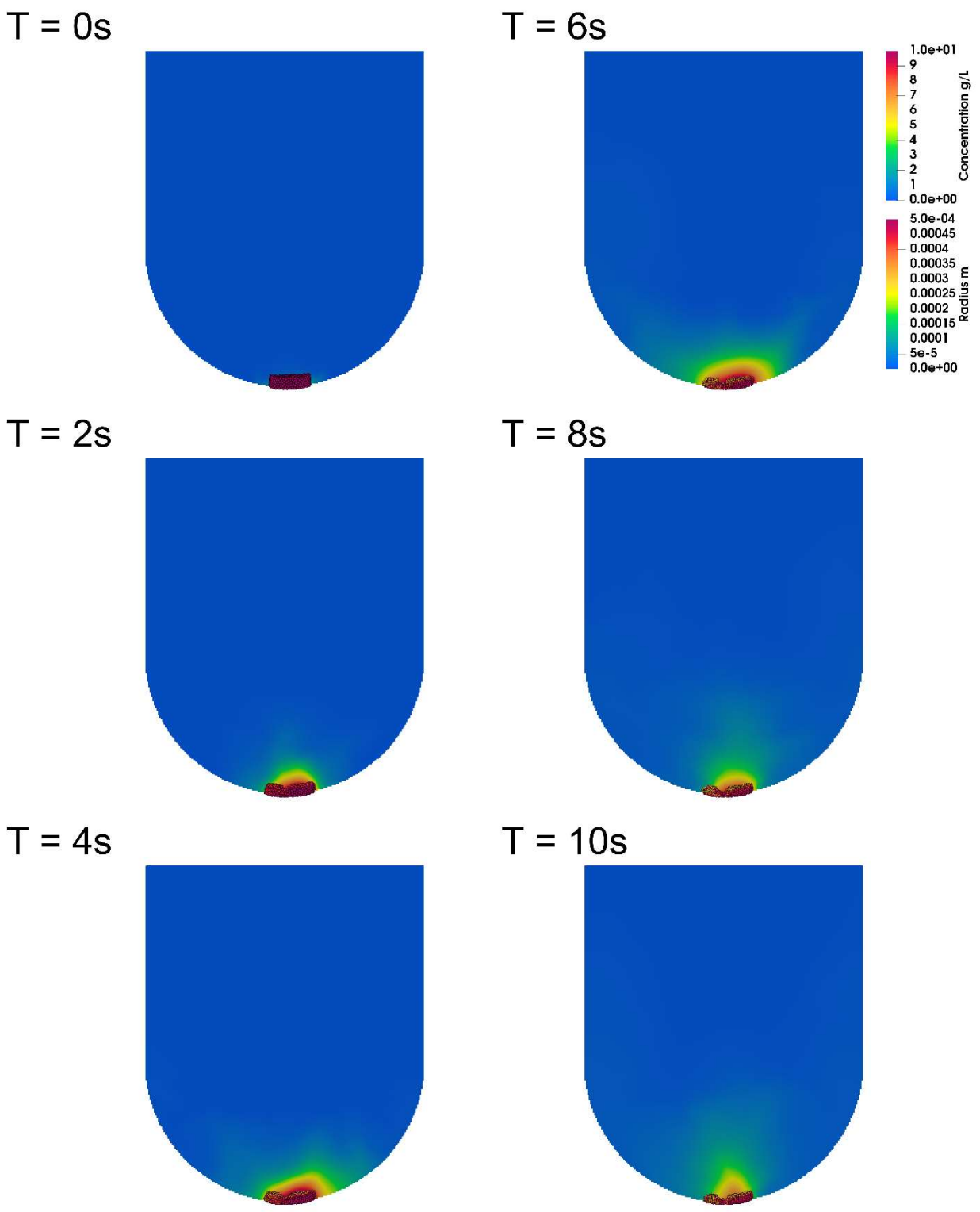

Figure 4.13 Concentration field in the USP apparatus II over time (T).

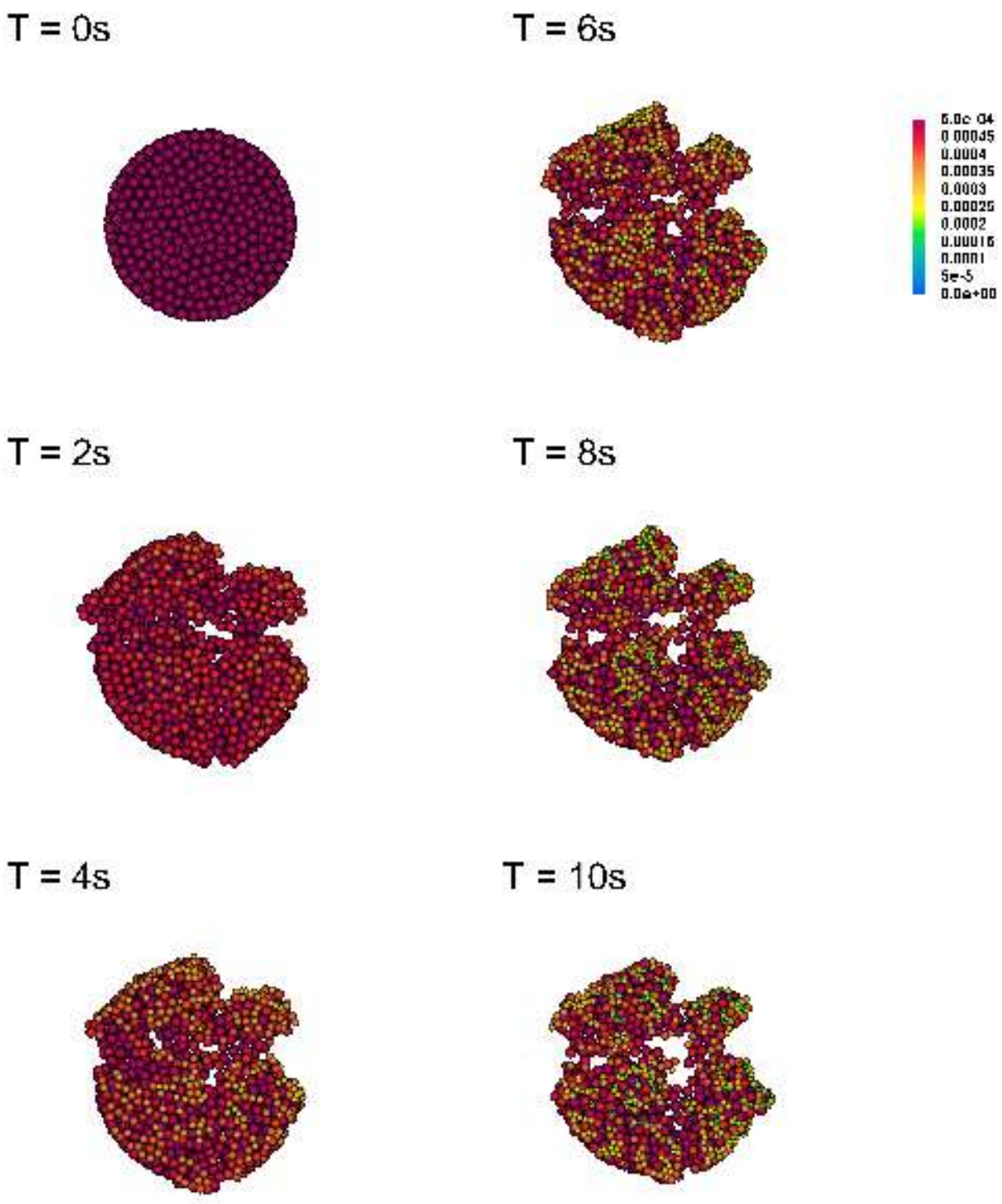

Figure 4.14 Tablet disintegration and dissolution over time (T).
This tablet is composed of pure API and designated as Tablet 1.

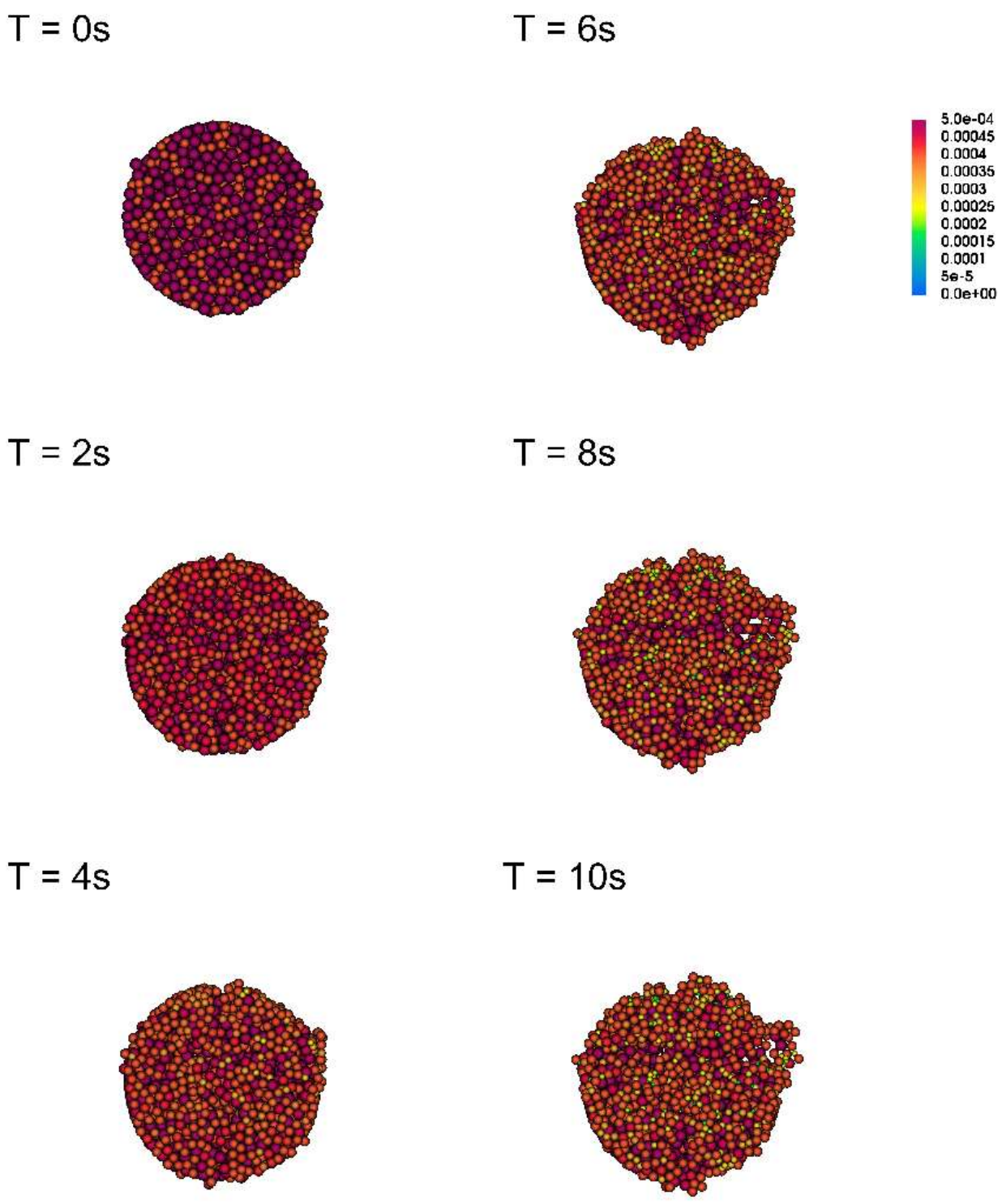

Figure 4.15 Tablet disintegration and dissolution over time (T). This tablet is composed of API (red particle at T=0s) and excipient, which does not absorb water (orange particle at T=0s). It is designated as Tablet 2.

It is evident from Figure 4.14 and Figure 4.15 that the particles on the surface of the tablet dissolved first. Moreover, due to the fluid movement around the tablet, the tablet disintegrated and the particles dissolved in the fluid. The tablet in Figure 4.14 is composed of pure API (Tablet 1). The tablet in Figure 4.15 is composed of 75% API and 25% excipient, which does not absorb water (Tablet 2). By comparing these two figures, we can see that the disintegration and dissolution of Tablet 2 are much slower than those of Tablet 1. As the excipient does not absorb water and will not dissolve, the excipient will reduce the dissolution speed of API particles. Furthermore, the excipient will keep the tablet intact during the dissolution process. This observation is confirmed in Figure 4.16, which shows the release fraction of API in the tablet. We can also see that the release speed of Tablet 2 is much slower than that of Tablet 1.

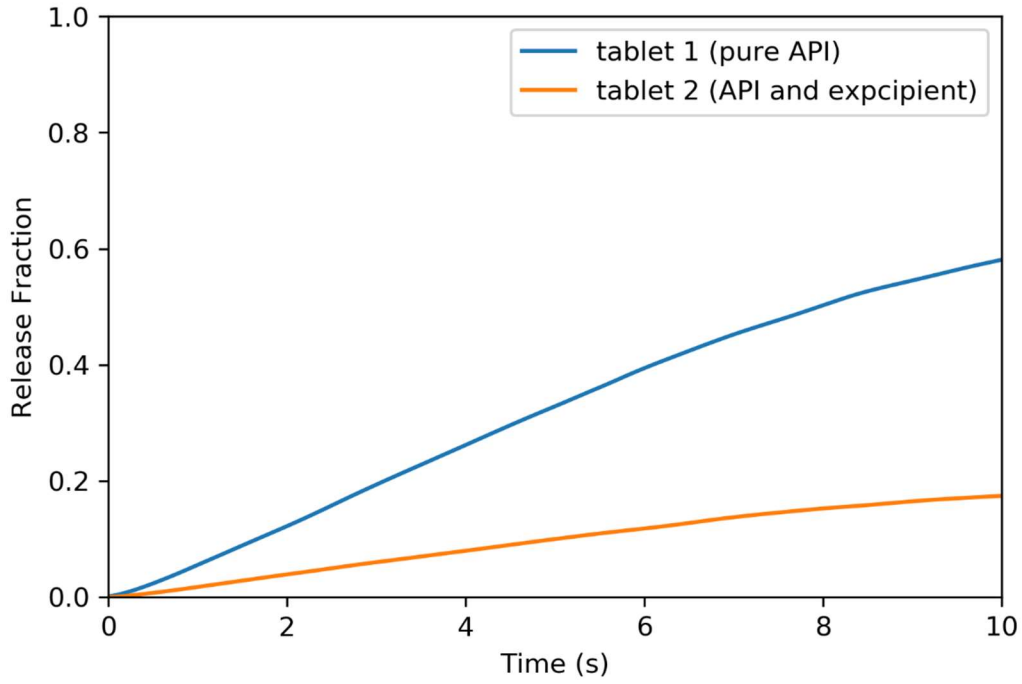

Figure 4.16 Dissolution profile of three different formulations. Tablet with pure API (Tablet 1) and tablet with 75% API and 25% excipient (Tablet 2).

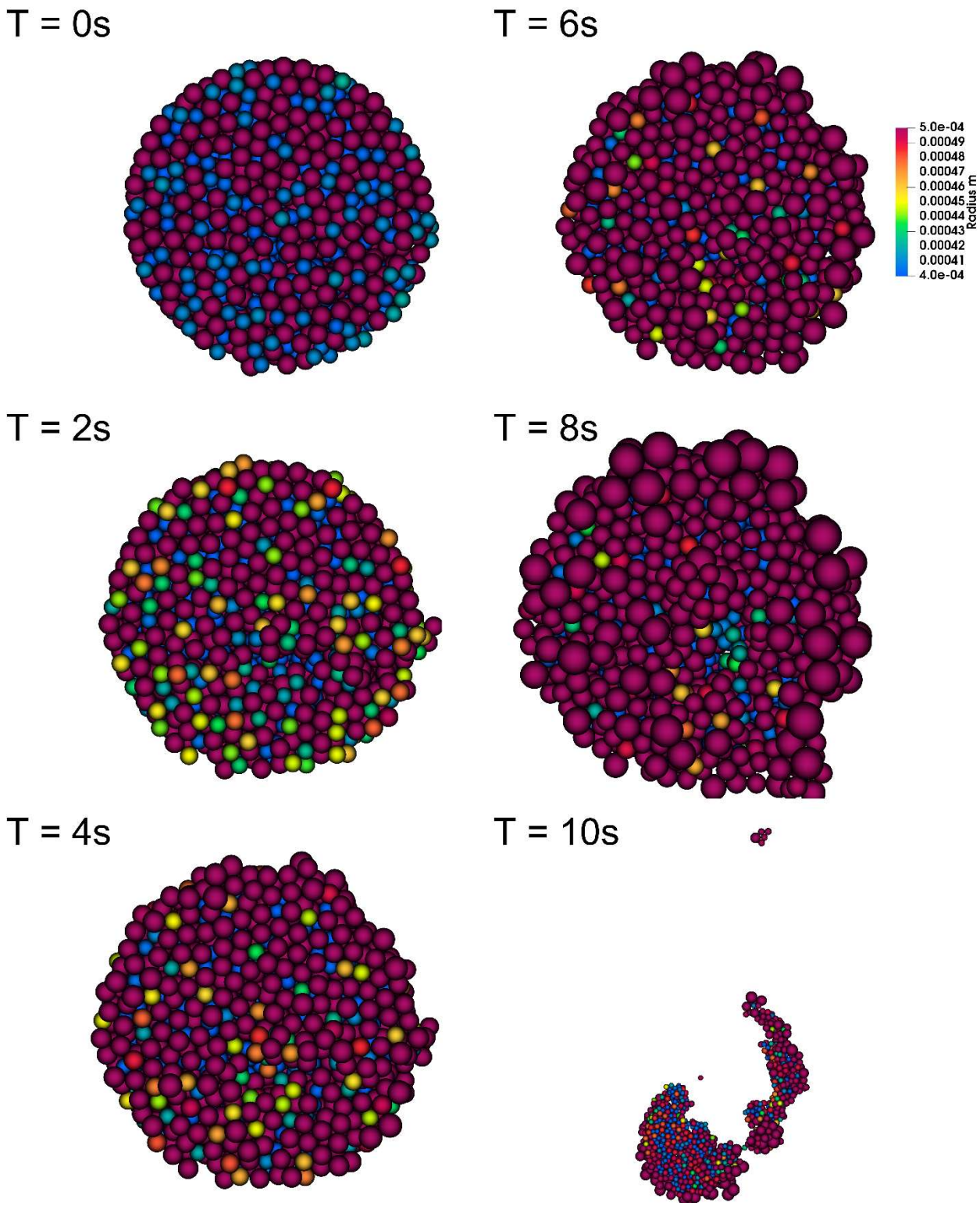

Figure 4.17 Tablet disintegration and dissolution over time (T). This tablet is composed of API (red particle at T=0s) and excipient, which absorb water (blue particle at T=0s). It is designated as Tablet 3.

We then showed an example of disintegration and dissolution for a tablet composed of 75% API and 25% excipient, which could absorb water. As shown in Figure 4.17, as time evolved, the excipient absorbed water from the environment and its radius became bigger. The change in the excipient particle radius resulted in repulsive forces to the neighboring particles, thus causing tablet breakage. At time T=10 s, we can see that the tablet was broken into two parts due to the external force from the water and the internal force attributed to the change in the excipient particle radius. Compared with the previous 2D DEM models by Kimber et al. [4, 6, 139], our 3D model can directly simulate the effect of hydrodynamics in the USP apparatus II instead of using a predefined external force. Moreover, our model can simulate the 3D structure of the tablets instead of just the 2D structure. This makes it easy for this model to be adopted in the design of new drug formulations, as well as in the application of DEM models in 3D-printed drug design.

4.6 Conclusion

In this project, we first simulated the tablet compression process based on the EEPA model. Then, we compared the dissolution profile of different formulations. Our model showed that the existence of unsolvable excipients reduces the dissolution speed of tablets while excipients that absorb water facilitate the breakage of tablets. With these examples, we were able to demonstrate that our model can be used for tablet formulation development. This is the first time that an *in silico* model was built to simulate the entire process of drug release from tablets—from compression to disintegration and dissolution. With further improvements in efficiency and accuracy, we can make a giant leap toward a virtual platform for drug formulation development. Moreover, our platform can be easily adapted to the emerging technology of 3D drug printing. In fact, newly designed 3D printing drugs could be tested using our model before being put into production.

CHAPTER 5. SUMMARY

Tablets are widely developed and manufactured for oral dosages of drugs. The disintegration and dissolution of tablets play an essential role in drug absorption and bioavailability. Thus, fully understating and even predicting the disintegration and dissolution process is vital for the Quality by Design (QbD) concept in drug development. By studying the parameters affecting tablet disintegration and dissolution, we can realize the rational design of new drug formulations.

Most physics-based models that simulate tablet disintegration and dissolution only focus on one aspect of tablet disintegration and dissolution. For example, some models try to imitate tablet particles with the discrete element model (DEM) [3-6]. However, they cannot directly simulate the impact of fluid in the environment. Some models try to mimic the hydrodynamic conditions in the USP apparatus II [32]. However, they fail to directly couple the tablet disintegration and dissolution process. The location distribution of the velocity field near the tablet plays a vital role in the speed of tablet disintegration and dissolution.

This study first developed a coupled LBM and DEM method to simulate the impact of hydrodynamic conditions on tablet disintegration and dissolution to overcome the shortage of previously developed models. By coupling LBM with DEM, we simulated the hydrodynamics in USP apparatus II and the tablet disintegration and dissolution process impacted by the fluid. Then, we simulated the fluid dynamics with the LBM model, the tablet compression and disintegration process with the DEM model, and the tablet particle dissolution process with the immersed moving boundary method by coupling LBM with DEM. For the first time, we realized the seamless simulation of drug formulation development, from tablet packing and compression to tablet disintegration and dissolution in the USP apparatus II. Our work paves the path toward a computational platform for drug formulation development. To build this platform, we took three steps, as shown in Chapters 2, 3, and 4.

Chapter 2 first presented a modeling and simulation framework for tablet disintegration and dissolution based on LBM and DEM. We simulated hydrodynamics in a dissolution device USP apparatus II with LBM. We compared the simulated velocity field against experimental results from previous research to validate our LBM and DEM coupling method. This comparison showed that our computational framework could correctly simulate tablet particle movement in USP apparatus II. The particle coning effect in the USP apparatus II was simulated and compared with

the previously generated governing equations for particle coning in the rotational fluid. The results indicate that our model could correctly simulate the dynamics of fluid and drug particles in USP apparatus II.

In Chapter 3, we realized that to simulate the tablet disintegration and dissolution process, we need to simulate the movement of particles in the fluid and the dissolution of particles in the fluid. As a result, we proposed a coupling method to simulate the drug particle dissolution in the liquid. Two lattice Boltzmann function distributions, namely, fluid velocity fluid and drug concentration field, were coupled. The drug particles were considered the source of new drug concentration in the fluid. We used the mass flux on the drug particle surface to connect the concentration change and update the drug particle radius. Based on our model, a single particle dissolution was first simulated and validated with the experimental results from previous research. Then, we performed simulations with different parameters, such as paddle rotation speed and drug particle dissolution constant. The results indicate that our model could simulate the velocity field and the concentration field in the USP apparatus II dissolution tests

In Chapter 4, we further developed our model to simulate the process of tablet disintegration and dissolution. First, we built a tablet model using the EEPA model that compressed independent particles into a solid tablet. We then placed this tablet model into a fluid field in the USP apparatus II, as measured by LBM, to simulate tablet disintegration and dissolution. We compared the dissolution profiles of different formulations and found that insoluble excipients in the tablet can help to reduce the dissolution speed of the tablet.

Our project provides a computational framework for developing new drug formulations, such as 3D drug printing. Anyone could easily test and verify new 3D-printed drug formulations using our computational platform before being developed into marketable products. In the future, we would further optimize our model to improve its computational efficiency. By realizing the large-scale and high-resolution simulations, our model supports our experimental results.

The goal was to build a computational platform that could connect the disintegration and dissolution kinetics of a tablet with its microstructure, such as the composition of the drug (API), excipient, drug particle size, and distribution in the tablet.

REFERENCES

1. Lamberti, G., I. Galdi, and A.A. Barba, *Controlled release from hydrogel-based solid matrices. A model accounting for water up-take, swelling and erosion.* Int J Pharm, 2011. **407**(1-2): p. 78-86.
2. Wu, C.-Y., et al., *Modelling the mechanical behaviour of pharmaceutical powders during compaction.* Powder technology, 2005. **152**(1-3): p. 107-117.
3. Kimber, J.A., S.G. Kazarian, and F. Štěpánek, *Microstructure-based mathematical modelling and spectroscopic imaging of tablet dissolution.* Computers & Chemical Engineering, 2011. **35**(7): p. 1328-1339.
4. Kimber, J.A., S.G. Kazarian, and F. Štěpánek, *Modelling of pharmaceutical tablet swelling and dissolution using discrete element method.* Chemical Engineering Science, 2012. **69**(1): p. 394-403.
5. Kimber, J.A., S.G. Kazarian, and F. Štěpánek, *Formulation design space analysis for drug release from swelling polymer tablets.* Powder Technology, 2013. **236**: p. 179-187.
6. Kimber, J.A., S.G. Kazarian, and F. Štěpánek, *DEM simulation of drug release from structurally heterogeneous swelling tablets.* Powder Technology, 2013. **248**: p. 68-76.
7. Bagherzadeh-Khalkhali, A., A.A. Mirghasemi, and S. Mohammadi, *Micromechanics of breakage in sharp-edge particles using combined DEM and FEM.* Particuology, 2008. **6**(5): p. 347-361.
8. Frenning, G., *An efficient finite/discrete element procedure for simulating compression of 3D particle assemblies.* Computer Methods in Applied Mechanics and Engineering, 2008. **197**(49-50): p. 4266-4272.
9. Yokoyama, R., et al., *Modeling of Disintegration and Dissolution Behavior of Mefenamic Acid Formulation Using Numeric Solution of Noyes-Whitney Equation with Cellular Automata on Microtomographic and Algorithmically Generated Surfaces.* Pharmaceutics, 2018. **10**(4): p. 259.
10. Wu, Y., D. Kildsig, and E. Ghaly, *Effect of hydrodynamic environment on tablets dissolution rate.* Pharmaceutical development and technology, 2004. **9**(1): p. 25-37.
11. USP, N. *General Chapter< 701> Disintegration*. in *Revision Bulletin. United States Pharmacopeial Convention, Inc., Rockville, MD*. 2008.

12. USP, G.C., *<711> Dissolution.* United States Pharmacopeia, 2011.
13. Rogers, A. and M. Ierapetritou, *Modeling and optimization of continuous pharmaceutical manufacturing processes*, in *Computer Aided Chemical Engineering*. 2015, Elsevier. p. 85-92.
14. Wang, Z., M.S. Escotet-Espinoza, and M. Ierapetritou, *Process analysis and optimization of continuous pharmaceutical manufacturing using flowsheet models.* Computers & Chemical Engineering, 2017. **107**: p. 77-91.
15. Noble, D. and J. Torczynski, *A lattice-Boltzmann method for partially saturated computational cells.* International Journal of Modern Physics C, 1998. **9**(08): p. 1189-1201.
16. Seil, P. and S. Pirker, *LBDEMcoupling: Open-Source Power for Fluid-Particle Systems.* 2017. **188**: p. 679-686.
17. Owen, D., C. Leonardi, and Y. Feng, *An efficient framework for fluid–structure interaction using the lattice Boltzmann method and immersed moving boundaries.* International Journal for Numerical Methods in Engineering, 2011. **87**(1-5): p. 66-95.
18. Mauger, J., et al., *Intrinsic dissolution performance testing of the USP dissolution apparatus 2 (rotating paddle) using modified salicylic acid calibrator tablets: proof of principle.* Dissolution Technologies, 2003. **10**: p. 6-15.
19. Kukura, J., et al., *Engineering tools for understanding the hydrodynamics of dissolution tests.* Drug development and industrial pharmacy, 2003. **29**(2): p. 231-239.
20. Bocanegra, L.M., et al., *Fluid and Particle Laser Doppler Velocity-Measurements and Mass-Transfer Predictions for the Usp Paddle Method Dissolution Apparatus.* Drug Development and Industrial Pharmacy, 1990. **16**(9): p. 1441-1464.
21. Bai, G., Y. Wang, and P.M. Armenante, *Velocity profiles and shear strain rate variability in the USP Dissolution Testing Apparatus 2 at different impeller agitation speeds.* Int J Pharm, 2011. **403**(1-2): p. 1-14.
22. Gao, Z., et al., *Studies of variability in dissolution testing with USP apparatus 2.* J Pharm Sci, 2007. **96**(7): p. 1794-801.
23. Gao, Z., et al., *The random vibration effects on dissolution testing with USP apparatus 2.* Journal of pharmaceutical sciences, 2009. **98**(1): p. 297-306.
24. Gao, Z., A. Thies, and W. Doub, *Vibration effects of lab equipment on dissolution testing with USP paddle method.* Journal of pharmaceutical sciences, 2010. **99**(1): p. 403-412.

25. Kukura, J., J.L. Baxter, and F.J. Muzzio, *Shear distribution and variability in the USP Apparatus 2 under turbulent conditions.* International Journal of Pharmaceutics, 2004. **279**(1-2): p. 9-17.
26. Baxter, J.L., J. Kukura, and F.J. Muzzio, *Hydrodynamics-induced variability in the USP apparatus II dissolution test.* Int J Pharm, 2005. **292**(1-2): p. 17-28.
27. Bai, G. and P.M. Armenante, *Hydrodynamic, mass transfer, and dissolution effects induced by tablet location during dissolution testing.* Journal of Pharmaceutical Sciences, 2009. **98**(4): p. 1511-1531.
28. Bai, G., P.M. Armenante, and R.V. Plank, *Experimental and computational determination of blend time in USP dissolution testing apparatus II.* Journal of Pharmaceutical Sciences, 2007. **96**(11): p. 3072-3086.
29. Bai, G., et al., *Hydrodynamic investigation of USP dissolution test apparatus II.* J Pharm Sci, 2007. **96**(9): p. 2327-49.
30. Baxter, J.L., J. Kukura, and F.J. Muzzio, *Shear-induced variability in the United States Pharmacopeia apparatus 2: Modifications to the existing system.* Aaps Journal, 2005. **7**(4): p. E857-E864.
31. Bocanegra, L., et al., *Fluid and particle laser Doppler velocity measurements and mass transfer predictions for the USP paddle method dissolution apparatus.* Drug Development and Industrial Pharmacy, 1990. **16**(9): p. 1441-1464.
32. Bai, G., Y.M. Wang, and P.M. Armenante, *Velocity profiles and shear strain rate variability in the USP Dissolution Testing Apparatus 2 at different impeller agitation speeds.* International Journal of Pharmaceutics, 2011. **403**(1-2): p. 1-14.
33. Bai, G., *Hydrodynamics investigation of in-vitro dissolution testing.* 2006.
34. Bai, G. and P.M. Armenante, *Velocity distribution and shear rate variability resulting from changes in the impeller location in the USP dissolution testing apparatus II.* Pharmaceutical Research, 2008. **25**(2): p. 320-336.
35. Laaksonen, H., J. Hirvonen, and T. Laaksonen, *Cellular automata model for swelling-controlled drug release.* Int J Pharm, 2009. **380**(1-2): p. 25-32.
36. Yeom, S.B., et al., *Application of the discrete element method for manufacturing process simulation in the pharmaceutical industry.* Pharmaceutics, 2019. **11**(8): p. 414.

37. Frenning, G., *Compression mechanics of granule beds: A combined finite/discrete element study.* Chemical Engineering Science, 2010. **65**(8): p. 2464-2471.
38. Furukawa, R., et al., *DEM Modelling of Granule Rearrangement and Fracture Behaviours During a Closed-Die Compaction.* Aaps Pharmscitech, 2017. **18**(6): p. 2368-2377.
39. Cao, H., et al., *A modelling framework for bulk particles dissolving in turbulent regime.* Chemical Engineering Research and Design, 2016. **114**: p. 108-118.
40. Cao, H., et al., *CFD-DNS simulation of irregular-shaped particle dissolution.* Particuology, 2019.
41. Jia, X. and R.A. Williams, *A Hybrid Mesoscale Modelling Approach to Dissolution of Granules and Tablets.* Chemical Engineering Research and Design, 2007. **85**(7): p. 1027-1038.
42. Chen, S. and G.D. Doolen, *Lattice Boltzmann method for fluid flows.* Annual review of fluid mechanics, 1998. **30**(1): p. 329-364.
43. Kang, Q., et al., *Lattice Boltzmann simulation of chemical dissolution in porous media.* Phys Rev E Stat Nonlin Soft Matter Phys, 2002. **65**(3 Pt 2B): p. 036318.
44. Qian, Y.-H., D. d'Humières, and P. Lallemand, *Lattice BGK models for Navier-Stokes equation.* EPL (Europhysics Letters), 1992. **17**(6): p. 479.
45. Schiller, U.D. and O. Kuksenok, *Lattice-Boltzmann Modeling of Multicomponent Systems: An Introduction.* Reviews in Computational Chemistry, Vol 31, 2019. **31**: p. 1-61.
46. Körner, C., et al., *Parallel lattice Boltzmann methods for CFD applications*, in *Numerical Solution of Partial Differential Equations on Parallel Computers*. 2006, Springer. p. 439-466.
47. Aidun, C.K. and J.R. Clausen, *Lattice-Boltzmann method for complex flows.* Annual review of fluid mechanics, 2010. **42**: p. 439-472.
48. Shan, X.W. and G. Doolen, *Multicomponent Lattice-Boltzmann Model with Interparticle Interaction.* Journal of Statistical Physics, 1995. **81**(1-2): p. 379-393.
49. Uhlmann, M., *An immersed boundary method with direct forcing for the simulation of particulate flows.* Journal of Computational Physics, 2005. **209**(2): p. 448-476.
50. Aidun, C.K., Y. Lu, and E.-J. Ding, *Direct analysis of particulate suspensions with inertia using the discrete Boltzmann equation.* Journal of Fluid Mechanics, 1998. **373**: p. 287-311.

51. Chen, H., S. Chen, and W.H. Matthaeus, *Recovery of the Navier-Stokes equations using a lattice-gas Boltzmann method.* Physical review A, 1992. **45**(8): p. R5339.
52. He, X. and L.-S. Luo, *Lattice Boltzmann model for the incompressible Navier–Stokes equation.* Journal of statistical Physics, 1997. **88**(3): p. 927-944.
53. Hardy, J., Y. Pomeau, and O. De Pazzis, *Time evolution of a two-dimensional classical lattice system.* Physical Review Letters, 1973. **31**(5): p. 276.
54. Higuera, F.J. and J. Jiménez, *Boltzmann approach to lattice gas simulations.* EPL (Europhysics Letters), 1989. **9**(7): p. 663.
55. McNamara, G.R. and G. Zanetti, *Use of the Boltzmann equation to simulate lattice-gas automata.* Physical review letters, 1988. **61**(20): p. 2332.
56. Guo, Z. and T. Zhao, *Lattice Boltzmann model for incompressible flows through porous media.* Physical review E, 2002. **66**(3): p. 036304.
57. Kang, Q., D. Zhang, and S. Chen, *Unified lattice Boltzmann method for flow in multiscale porous media.* Physical Review E, 2002. **66**(5): p. 056307.
58. Obrecht, C., et al., *A new approach to the lattice Boltzmann method for graphics processing units.* Computers & Mathematics with Applications, 2011. **61**(12): p. 3628-3638.
59. Schornbaum, F. and U. Rude, *Massively parallel algorithms for the lattice Boltzmann method on nonuniform grids.* SIAM Journal on Scientific Computing, 2016. **38**(2): p. C96-C126.
60. Latt, J., et al., *Palabos: Parallel Lattice Boltzmann solver.* Computers & Mathematics with Applications, 2020.
61. Obrecht, C., et al., *Multi-GPU implementation of the lattice Boltzmann method.* Computers & Mathematics with Applications, 2013. **65**(2): p. 252-261.
62. Mei, R., L.-S. Luo, and W. Shyy, *An accurate curved boundary treatment in the lattice Boltzmann method.* Journal of computational physics, 1999. **155**(2): p. 307-330.
63. Noble, D.R., et al., *A consistent hydrodynamic boundary condition for the lattice Boltzmann method.* Physics of Fluids, 1995. **7**(1): p. 203-209.
64. Heuveline, V. and J. Latt, *The OpenLB project: an open source and object oriented implementation of lattice Boltzmann methods.* International Journal of Modern Physics C, 2007. **18**(04): p. 627-634.

65. Feichtinger, C., et al., *WaLBerla: HPC software design for computational engineering simulations.* Journal of Computational Science, 2011. **2**(2): p. 105-112.
66. Januszewski, M. and M. Kostur, *Sailfish: A flexible multi-GPU implementation of the lattice Boltzmann method.* Computer Physics Communications, 2014. **185**(9): p. 2350-2368.
67. Tan, J., T. Sinno, and S.L. Diamond, *A parallel fluid-solid coupling model using LAMMPS and Palabos based on the immersed boundary method.* J Comput Sci, 2018. **25**: p. 89-100.
68. Wolf-Gladrow, D.A., *Lattice-gas cellular automata and lattice Boltzmann models: an introduction*. 2004: Springer.
69. Bao, Y.B. and J. Meskas, *Lattice Boltzmann method for fluid simulations.* 2011.
70. Bhatnagar, P.L., E.P. Gross, and M. Krook, *A model for collision processes in gases. I. Small amplitude processes in charged and neutral one-component systems.* Physical review, 1954. **94**(3): p. 511.
71. Harwood, A.R., P. Wenisch, and A.J. Revell. *A real-time modelling and simulation platform for virtual engineering design and analysis*. in *Proceedings of 6th European Conference on Computational Mechanics (ECCM 6) and 7th European Conference on Computational Fluid Dynamics (ECFD 7)*. 2018.
72. Flekkøy, E., *Lattice Bhatnagar-Gross-Krook models for miscible fluids.* Physical Review E, 1993. **47**(6): p. 4247.
73. Liou, T.-M. and C.-S. Wang, *Three-dimensional multidomain lattice Boltzmann grid refinement for passive scalar transport.* Physical Review E, 2018. **98**(1): p. 013306.
74. Haussmann, M., et al., *Direct numerical simulation of decaying homogeneous isotropic turbulence—numerical experiments on stability, consistency and accuracy of distinct lattice Boltzmann methods.* International Journal of Modern Physics C, 2019. **30**(09): p. 1950074.
75. Chetverushkin, B.N., *Parallel computational fluid dynamics : advanced numerical methods : software and applications : proceedings of the Parallel CFD 2003 Conference, Moscow, Russia (May 13-15, 2003)*. 2004, Amsterdam: Elsevier. xvi, 542 pages.
76. Peng, C., et al., *Direct numerical simulation of turbulent pipe flow using the lattice Boltzmann method.* Journal of Computational Physics, 2018. **357**: p. 16-42.

77. Smagorinsky, J., *General circulation experiments with the primitive equations: I. The basic experiment.* Monthly weather review, 1963. **91**(3): p. 99-164.
78. Stillinger, F.H. and A. Rahman, *Improved simulation of liquid water by molecular dynamics.* The Journal of Chemical Physics, 1974. **60**(4): p. 1545-1557.
79. Rahman, A., *Correlations in the motion of atoms in liquid argon.* Physical review, 1964. **136**(2A): p. A405.
80. Alder, B.J. and T.E. Wainwright, *Studies in molecular dynamics. I. General method.* The Journal of Chemical Physics, 1959. **31**(2): p. 459-466.
81. Cundall, P.A. and O.D. Strack, *A discrete numerical model for granular assemblies.* geotechnique, 1979. **29**(1): p. 47-65.
82. Plimpton, S., *Fast parallel algorithms for short-range molecular dynamics.* Journal of computational physics, 1995. **117**(1): p. 1-19.
83. Kloss, C. and C. Goniva, *LIGGGHTS–open source discrete element simulations of granular materials based on Lammps.* Supplemental Proceedings: Materials Fabrication, Properties, Characterization, and Modeling, 2011. **2**: p. 781-788.
84. Kozicki, J. and F.V. Donze, *YADE-OPEN DEM: An open-source software using a discrete element method to simulate granular material.* Engineering Computations, 2009.
85. André, D., et al., *The GranOO workbench, a new tool for developing discrete element simulations, and its application to tribological problems.* Advances in Engineering Software, 2014. **74**: p. 40-48.
86. André, D., J.-L. Charles, and I. Iordanoff. *A new C++ workbench to develop discrete element simulations: GranOO*. in *2nd ECCOMAS Young Investigators Conference (YIC 2013, Bordeaux, France)*. 2013.
87. Jahani, M., A. Farzanegan, and M. Noaparast, *Investigation of screening performance of banana screens using LIGGGHTS DEM solver.* Powder Technology, 2015. **283**: p. 32-47.
88. Brilliantov, N.V., et al., *Model for collisions in granular gases.* Physical review E, 1996. **53**(5): p. 5382.
89. Zhang, H. and H. Makse, *Jamming transition in emulsions and granular materials.* Physical Review E, 2005. **72**(1): p. 011301.

90. Di Renzo, A. and F.P. Di Maio, *An improved integral non-linear model for the contact of particles in distinct element simulations.* Chemical engineering science, 2005. **60**(5): p. 1303-1312.
91. Ai, J., et al., *Assessment of rolling resistance models in discrete element simulations.* Powder Technology, 2011. **206**(3): p. 269-282.
92. Morrissey, J.P., *Discrete element modelling of iron ore pellets to include the effects of moisture and fines.* 2013.
93. Carr, M.J., et al. *Calibration procedure of Discrete Element Method (DEM) parameters for cohesive bulk materials*. in *13th International Conference on Bulk Materials Storage, Handling and Transportation (ICBMH 2019)*. 2019. Engineers Australia.
94. Coetzee, C., *Edinburgh-Elasto-Plastic-Adhesion (EEPA) Contact Model.* 2020.
95. Mohajeri, M.J., H.Q. Do, and D.L. Schott, *DEM calibration of cohesive material in the ring shear test by applying a genetic algorithm framework.* Advanced Powder Technology, 2020. **31**(5): p. 1838-1850.
96. Siiria, S.M., et al., *3D simulation of internal tablet strength during tableting.* AAPS PharmSciTech, 2011. **12**(2): p. 593-603.
97. Mei, R., et al., *Lattice Boltzmann Method for 3-D Flows with Curved Boundary.* Journal of Computational Physics, 2000. **161**(2): p. 680-699.
98. Ladd, A.J.C. and R. Verberg, *Lattice-Boltzmann simulations of particle-fluid suspensions.* Journal of Statistical Physics, 2001. **104**(5-6): p. 1191-1251.
99. Ladd, A.J., *Numerical simulations of particulate suspensions via a discretized Boltzmann equation. Part 2. Numerical results.* Journal of fluid mechanics, 1994. **271**: p. 311-339.
100. Seil, P., *LBDEMcoupling: implementation, validation, and applications of a coupled open-source solver for fluid-particle systems/eingereicht von Dipl.-Ing. Philippe Seil*. 2016, Universität Linz.
101. Noyes, A.A. and W.R. Whitney, *The rate of solution of solid substances in their own solutions.* Journal of the American Chemical Society, 1897. **19**(12): p. 930-934.
102. Cox, D.C. and W.B. Furman, *Systematic error associated with apparatus 2 of the USP dissolution test V: Interaction of two tableted prednisone formulations with glass and plastic vessels.* J Pharm Sci, 1984. **73**(8): p. 1125-7.

103. Qureshi, S.A. and J. Shabnam, *Cause of high variability in drug dissolution testing and its impact on setting tolerances.* European Journal of Pharmaceutical Sciences, 2001. **12**(3): p. 271-276.

104. Cox, D.C., et al., *Systematic error associated with apparatus 2 of the USP dissolution test III: limitations of calibrators and the USP suitability test.* Journal of pharmaceutical sciences, 1983. **72**(8): p. 910-913.

105. Frisch, U., B. Hasslacher, and Y. Pomeau, *Lattice-gas automata for the Navier-Stokes equation.* Physical review letters, 1986. **56**(14): p. 1505.

106. Jahanshaloo, L., E. Pouryazdanpanah, and N.A. Che Sidik, *A review on the application of the lattice Boltzmann method for turbulent flow simulation.* Numerical Heat Transfer, Part A: Applications, 2013. **64**(11): p. 938-953.

107. Kloss, C., et al., *Models, algorithms and validation for opensource DEM and CFD–DEM.* Progress in Computational Fluid Dynamics, an International Journal, 2012. **12**(2-3): p. 140-152.

108. Higuchi, M., et al., *Minimum rotation speed to prevent coning phenomena in compendium paddle dissolution apparatus.* Eur J Pharm Sci, 2014. **65**: p. 74-8.

109. Higuchi, M., et al., *Prediction of coning phenomena for irregular particles in paddle dissolution test.* Eur J Pharm Sci, 2015. **76**: p. 213-6.

110. Higuchi, M., K. Terada, and K. Sugano, *Coning phenomena under laminar flow.* Eur J Pharm Sci, 2015. **80**: p. 53-5.

111. Marabi, A., et al., *Assessing dissolution kinetics of powders by a single particle approach.* Chemical Engineering Journal, 2008. **139**(1): p. 118-127.

112. Svanbäck, S., H. Ehlers, and J. Yliruusi, *Optical microscopy as a comparative analytical technique for single-particle dissolution studies.* International journal of pharmaceutics, 2014. **469**(1): p. 10-16.

113. Kašpar, O., et al., *Combined UV/vis and micro-tomography investigation of acetaminophen dissolution from granules.* International journal of pharmaceutics, 2013. **458**(2): p. 272-281.

114. Smrčka, D., J. Dohnal, and F. Štěpánek, *Dissolution and disintegration kinetics of high-active pharmaceutical granules produced at laboratory and manufacturing scale.* European Journal of Pharmaceutics and Biopharmaceutics, 2016. **106**: p. 107-116.

115. Siepmann, J. and F. Siepmann, *Mathematical modeling of drug dissolution.* International journal of pharmaceutics, 2013. **453**(1): p. 12-24.
116. Brunner, E., *Reaktionsgeschwindigkeit in heterogenen Systemen*. 1903: Georg-Augusts-Universitat, Gottingen.
117. Nernst, W., *Theorie der Reaktionsgeschwindigkeit in heterogenen Systemen.* Zeitschrift für physikalische Chemie, 1904. **47**(1): p. 52-55.
118. Dali, M.V. and J. Carstensen, *Effect of change in shape factor of a single crystal on its dissolution behavior.* Pharmaceutical research, 1996. **13**(1): p. 155-162.
119. Simöes, S., L.P. de Almeida, and M. Figueiredo, *Testing the applicability of classical diffusional models to polydisperse systems.* International journal of pharmaceutics, 1996. **139**(1-2): p. 169-176.
120. Derksen, J.J., et al., *Simulations of dissolution of spherical particles in laminar shear flow.* Chemical Engineering Research and Design, 2015. **93**: p. 66-78.
121. Todaro, V., et al., *Characterization and Simulation of Hydrodynamics in the Paddle, Basket and Flow-Through Dissolution Testing Apparatuses - A Review.* Dissolution Technologies, 2017. **24**(3): p. 24-36.
122. Martinez, A.F., et al., *Characterization of the Hydrodynamics in the USP Basket Apparatus Using Computational Fluid Dynamics.* J Pharm Sci, 2019.
123. D'Arcy, D.M., O.I. Corrigan, and A.M. Healy, *Hydrodynamic simulation (computational fluid dynamics) of asymmetrically positioned tablets in the paddle dissolution apparatus: impact on dissolution rate and variability.* J Pharm Pharmacol, 2005. **57**(10): p. 1243-50.
124. Wang, B., G. Bredael, and P.M. Armenante, *Computational hydrodynamic comparison of a mini vessel and a USP 2 dissolution testing system to predict the dynamic operating conditions for similarity of dissolution performance.* International Journal of Pharmaceutics, 2018. **539**(1-2): p. 112-130.
125. Guo, Z.-L., B.-C. Shi, and N.-C. Wang, *Fully Lagrangian and lattice Boltzmann methods for the advection-diffusion equation.* Journal of scientific computing, 1999. **14**(3): p. 291-300.
126. Van Der Sman, R., *Galilean invariant lattice Boltzmann scheme for natural convection on square and rectangular lattices.* Physical Review E, 2006. **74**(2): p. 026705.

127. Shi, B., et al., *A new scheme for source term in LBGK model for convection–diffusion equation.* Computers & Mathematics with Applications, 2008. **55**(7): p. 1568-1575.
128. Thakur, S.C., et al., *Micromechanical analysis of cohesive granular materials using the discrete element method with an adhesive elasto-plastic contact model.* Granular Matter, 2014. **16**(3): p. 383-400.
129. Haynes, W.M., *CRC handbook of chemistry and physics*. 2014: CRC press.
130. Rost, M. and P.O. Quist, *Dissolution of USP prednisone calibrator tablets - Effects of stirring conditions and particle size distribution.* Journal of Pharmaceutical and Biomedical Analysis, 2003. **31**(6): p. 1129-1143.
131. Kimber, J.A., S.G. Kazarian, and F. Stepanek, *Modelling of pharmaceutical tablet swelling and dissolution using discrete element method.* Chemical Engineering Science, 2012. **69**(1): p. 394-403.
132. Kimber, J.A., S.G. Kazarian, and F. Stepanek, *DEM simulation of drug release from structurally heterogeneous swelling tablets.* Powder Technology, 2013. **248**: p. 68-76.
133. Kimber, J.A., S.G. Kazarian, and F. Stepanek, *Formulation design space analysis for drug release from swelling polymer tablets.* Powder Technology, 2013. **236**: p. 179-187.
134. Bhatnagar, P.L., E.P. Gross, and M. Krook, *A MODEL FOR COLLISION PROCESSES IN GASES .1. SMALL AMPLITUDE PROCESSES IN CHARGED AND NEUTRAL ONE-COMPONENT SYSTEMS.* Physical Review, 1954. **94**(3): p. 511-525.
135. Chen, S. and G.D. Doolen, *Lattice Boltzmann method for fluid flows.* Annual Review of Fluid Mechanics, 1998. **30**: p. 329-364.
136. Noble, D.R. and J.R. Torczynski, *A lattice-Boltzmann method for partially saturated computational cells.* International Journal of Modern Physics C, 1998. **9**(8): p. 1189-1201.
137. Martys, N.S. and H.D. Chen, *Simulation of multicomponent fluids in complex three-dimensional geometries by the lattice Boltzmann method.* Physical Review E, 1996. **53**(1): p. 743-750.
138. Baxter, J.L., J. Kukura, and F.J. Muzzio, *Hydrodynamics-induced variability in the USP apparatus II dissolution test.* International Journal of Pharmaceutics, 2005. **292**(1-2): p. 17-28.

139. Kimber, J.A., S.G. Kazarian, and F. Štěpánek, *A fast algorithm for mass transfer on an unstructured grid formed by DEM particles.* Powder Technology, 2011. **214**(3): p. 415-422.